

Phase transitions of some discrete models in statistical mechanics

A thesis submitted for the degree of

Doctor of Philosophy

by

Zongzheng Zhou

School of Mathematical Sciences

Monash University

Australia

April 2016

Copyright notice

© Zongzheng Zhou (2016). Except as provided in the Copyright Act 1968, this thesis may not be reproduced in any form without the written permission of the author.

I certify that I have made all reasonable efforts to secure copyright permissions for third-party content included in this thesis and have not knowingly added copyright content to my work without the owner's permission.

Contents

Abstract	ix
List of publications	xi
Acknowledgement	xv
1 Introduction	3
1.1 Percolation	3
1.2 Directed percolation	6
1.3 The face-cubic model	9
1.4 Thesis Outline	11
2 Bond and Site Percolation in Three Dimensions	19
2.1 Introduction	19
2.2 Sampled quantities	21
2.3 Estimating p_c	24
2.3.1 Bond percolation	24
2.3.2 Site percolation	27
2.4 Results at p_c	29
2.4.1 Estimating y_t	30
2.4.2 Estimating y_h	31
2.4.3 Estimating d_{\min}	33
2.4.4 Excess number of clusters	34
2.5 Discussion	36

2.6	Acknowledgments	37
3	A high-precision Monte Carlo study of directed percolation in (d+1) dimensions	43
3.1	Introduction	43
3.2	Description of the model and simulations	45
3.2.1	Generating DP configurations	45
3.2.2	Lattices	47
3.2.3	Observables	47
3.2.4	Improved Estimators	49
3.3	Percolation Thresholds	52
3.3.1	Fitting Methodology	52
3.3.2	Results for $d = 2, 3$	54
3.3.3	Results for $d = 4$	56
3.3.4	Result for $d = 5, 6, 7$	57
3.3.5	Summary of thresholds	57
3.4	Critical Exponents	60
3.5	Critical Distributions	63
3.6	Estimates of thresholds and critical exponents in (1+1) dimensions.	64
3.7	Discussion of the improved estimators	65
3.8	Discussion	67
4	Geometric structure of percolation clusters	75
4.1	Introduction	75
4.2	Model, Algorithm and Observables	80
4.2.1	Model	80
4.2.2	Algorithm	81
4.2.3	Measured quantities	82
4.3	Results	83

4.3.1	Fitting ansätze and methodology	83
4.3.2	Bond densities	85
4.3.3	Fractal dimensions of clusters	86
4.3.4	Fractal dimensions of loops	88
4.4	A loop duality lemma	90
4.5	Discussion	92
4.6	Acknowledgments	94
5	Leaf-excluded percolation in two and three dimensions	99
5.1	Introduction	99
5.2	Algorithm and Observables	102
5.2.1	Monte Carlo algorithm	102
5.2.2	Sampled quantities	104
5.3	Results	105
5.3.1	Fitting methodology	105
5.3.2	Square lattice near v_c	106
5.3.3	Square lattice at v_c	109
5.3.4	Simple-cubic lattice	109
5.4	Discussion	113
5.5	Acknowledgments	114
6	An n-component face-cubic model on the complete graph	119
6.1	Introduction	119
6.2	The n -component face-cubic model	123
6.2.1	Model	123
6.2.2	Large deviations theory	124
6.2.3	Rate function for $P^\beta(S_N)$	126
6.3	Limit theorems	127
6.4	Preliminary results needed to prove theorems	137

6.5	The general face-cubic model	144
6.5.1	Model	144
6.5.2	Useful definitions	146
6.5.3	Phase diagram	149
6.5.4	Preliminary knowledge needed to prove the phase diagram	154
6.6	Discussion	165
7	Conclusion	173
7.1	Estimating thresholds and critical exponents for the percolation and directed percolation models	173
7.2	Geometric structure of percolation clusters	174
7.3	Phase transitions of an n -component face-cubic model on the com- plete graph	175
	Bibliography	189

Abstract

We present in this thesis our recent work concerning phase transitions of some discrete models in statistical mechanics. Our work can be separated into three parts. In the first part, by performing extensive Monte Carlo simulations, we carefully estimate percolation thresholds and universal parameters in percolation and directed percolation. Specifically, we estimate percolation thresholds and critical exponents of the bond and site percolation models on a simple-cubic lattice. Various universal amplitudes are also obtained, including wrapping probabilities, ratios associated with the cluster-size distribution, and the excess cluster number. We also study the bond and site directed (oriented) percolation models in $(d + 1)$ dimensions on simple-cubic and body-centered-cubic lattices, with $2 \leq d \leq 7$. Both percolation thresholds and critical exponents are precisely estimated. Typically, the estimates we reported significantly improve the precision of previous results, especially for directed percolation in high dimensions where our estimates are the first reported.

The second part of this thesis is devoted to understanding critical percolation clusters. We first study the geometric structure of percolation clusters by considering a natural partition of occupied bonds. Specifically, we classify all occupied bonds into three types: branches, junctions and nonbridges. Deleting all branches from a percolation configuration results in a leaf-free configuration, while deleting all bridges produces a bridge-free configuration. For critical bond percolation on the

square lattice, we show that the density of bridges and nonbridges both tend to $1/4$ for large system sizes. Although branches account for $\approx 43\%$ of all occupied bonds, we find that the fractal dimensions of the cluster size and hull length of leaf-free configurations are consistent with those for standard percolation configurations. The fractal dimensions of the cluster size and hull length of bridge-free configurations are respectively given by the backbone and external perimeter dimensions. Inspired by the nontrivial properties of leaf-free configurations, we then study a leaf-excluded percolation model in which all configurations are conditioned to have no leaves. We study this model on the square and simple-cubic lattices via Monte Carlo simulation, using a worm-like algorithm. Our results imply that the phase transition of the leaf-excluded percolation model belongs to the standard percolation universality class.

The third part of this thesis seeks to rigorously study an n -component face-cubic model on the complete graph. We first consider the standard face-cubic model, and perform a large deviation analysis of the probability distribution of the magnetization, i.e. the empirical mean of the spin states. We study the limit theorems of the magnetization for all temperatures, which reveals that there exist continuous phase transitions for $n \leq 3$, and discontinuous phase transitions for $n \geq 4$. This result clarifies the longstanding uncertainty about the nature of phase transition at $n = 3$. We then study a general version in which a Potts-like interaction is added. We rigorously study the phase diagram of this general face-cubic model, by a large deviations analysis. We prove the $n = 2$ case on the (J_1, J_2) plane, except the region $-J_1 < J_2 < 0$ when $J_1 > 2$. Our results show that at least four phases exist on the phase diagram: disordered, Ising, Potts, and face-cubic.

List of publications

1. Wang J, Zhou Z, Liu Q, Garoni TM, Deng Y. 2013a. High-precision monte carlo study of directed percolation in $(d + 1)$ dimensions. *Physical Review E* **88**: 042 102
2. Wang J, Zhou Z, Zhang W, Garoni TM, Deng Y. 2013b. Bond and site percolation in three dimensions. *Physical Review E* **87**: 052 107
3. Xu X, Wang J, Zhou Z, Garoni TM, Deng Y. 2014b. Geometric structure of percolation clusters. *Physical Review E* **89**: 012 120
4. Zhou Z, Xu X, Garoni TM, Deng Y. 2015. Leaf-excluded percolation in two and three dimensions. *Physical Review E* **91**: 022 140
5. Zhou Z, Garoni TM. 2015. An n -component face-cubic model on the complete graph. *in preparation*

General Declaration

In accordance with Monash University Doctorate Regulation 17.2 Doctor of Philosophy and Research Master's regulations the following declarations are made:

I hereby declare that this thesis contains no material which has been accepted for the award of any other degree or diploma at any university or equivalent institution and that, to the best of my knowledge and belief, this thesis contains no material previously published or written by another person, except where due reference is made in the text of the thesis.

This thesis includes 4 original papers published in peer reviewed journals and 1 unpublished publications. The core theme of the thesis is phase transitions in statistical mechanics. The ideas, development and writing up of all the papers in the thesis were the principal responsibility of myself, the candidate, working within the School of Mathematical Sciences, Monash University, under the supervision of Dr. Timothy Garoni.

The inclusion of co-authors reflects the fact that the work came from active collaboration between researchers and acknowledges input into team-based research.

In the case of Chapters 2-6 my contribution to the work involved the following:

Thesis chapter	Publication title	Publication status*	Nature and extent of candidate's contribution
2	Bond and site percolation in three dimensions	published	Run simulations, analyse the data, and write the article
3	A high-precision Monte Carlo study of directed percolation in (d+1) dimensions	published	Run simulations, analyse the data, and write the article
4	Geometric structure of percolation clusters	published	Run simulations, analyse the data, and write the article
5	Leaf-excluded percolation in two and three dimensions	published	Run simulations, analyse the data, and write the article
6	An n-component face-cubic on the complete graph	unpublished	Derive theorems and lemmas, and write the article

I have not renumbered sections of submitted or published papers in order to generate a consistent presentation within the thesis.

Signed: 

Date:27/01/2016.....

Acknowledgement

It is a great pleasure to express my deepest thanks and heartfelt gratitude to my supervisor Dr. Timothy Garoni, who has been constantly providing thoughtful supports and guidelines for both my life and study in Monash. Great appreciations are also given to Prof. Youjin Deng in University of Science and Technology of China, for his long-standing collaboration with us and encouragement on my research. Moreover, I would like to extend my gratitude to Dr. Andrea Collevocchio in Monash for his kind push and supervision on me, which is essentially important to accelerate my study.

I would like to sincerely thank my family for their understanding and support to my study. As a child without siblings, studying overseas is indeed hard not only for me but also for my parents. Special thanks are given to my wife, who is willing to give up her career to accompany me to Australia. After our first son was born, she totally takes charge of looking after our baby such that I can focus on my study. Without her support and help, I could easily give up.

It is grateful to express my thanks to my colleagues in Monash, who I am fully indebted from. The discussions with them largely open my mind and the enjoyable chat lets me survive all the stress. All the time we spend together is memorable in my whole life.

List of Figures

1.1	Stochastic formulation of DP on the square lattice. The vertical direction corresponds to time, and the dashed lines identify the sets V_t	8
2.1	Plots of $R^{(x)}(p, L)$ (top) and $R^{(a)}(p, L)$ (bottom) vs L for fixed values of p , for bond percolation. In both cases, the curves correspond to our preferred fit of the MC data for $R(p, L)$ by the ansatz (2.3.1); the dashed curve corresponds to setting $p = 0.248\,811\,82$. The shaded blue strips indicate an interval of 1σ above and below the estimates $R_c^{(x)} = 0.257\,78(6)$ and $R_c^{(a)} = 0.459\,97(8)$	23
2.2	Plots of Q_1 and Q_2 vs $L^{-1.2}$ (top), and $R^{(x)}$ and $R^{(a)}$ vs L^{-2} (bottom), with $p = 0.248\,811\,8$, for bond percolation. The solid lines are simply to guide the eye.	24
2.3	Plots of $R^{(x)}(p, L)$ (top) and $R^{(a)}(p, L)$ (bottom) vs L for fixed values of p , for site percolation. In both cases, the curves correspond to our preferred fit of the MC data for $R(p, L)$ by ansatz (2.3.1); the dashed curve corresponds to setting $p = 0.311\,607\,7$. The shaded blue strips indicate an interval of 1σ above and below the estimates $R_c^{(x)} = 0.257\,82(6)$ and $R_c^{(a)} = 0.459\,99(8)$	29
2.4	Plots of $(\ln g_{bR}^{(x)} - y_t \ln L)$ (top) and $(\ln g_{sR}^{(x)} - y_t \ln L)$ (bottom) vs $\ln L$ illustrating our estimate $y_t = 1.141\,0(15)$. The dashed curves are simply to guide the eye.	31

2.5	Plots of $(\ln C_1^b - y_h \ln L)$ (top) and $(\ln C_1^s - y_h \ln L)$ (bottom) vs $\ln L$ to show our estimate $y_h = 2.52295(15)$. The dashed curves are simply to guide the eye.	32
2.6	Log-log plot of S versus L for bond and site percolation. Two straight lines with slope 1.3756 are included for comparison.	35
3.1	Stochastic formulation of DP on the square lattice. The vertical direction corresponds to time, and the dashed lines identify the sets V_t	45
3.2	(2+1)-dimensional SC (left) and BCC (right) lattices.	47
3.3	(Color online) Plot of $\mathbb{P}(\mathcal{N}_t/ V_t = \cdot)$ at $t = 16384$ for $d = 3$ bond DP on BCC lattice, with $p = 0.13237417$ (square) and $p' = 0.13237453$ (circle).	52
3.4	(Color online) Plot of the Q_t data for bond and site DP on the SC and BCC lattices versus $x = q_1(p_c - p)t^{y_{ }}$ for $d = 2$	52
3.5	(Color online) Plots of $Q_t - c_1 t^{y_u}$ (for $d \neq 4$) and $(Q_t - c_1 t^{-1})/(\log t + h_1)^{1/6}$ (for $d = 4$) versus t for several DP models. The subfigures (a) to (f) respectively correspond to $d = 2$ SC site DP, $d = 3$ BCC bond DP, $d = 4$ SC bond DP, $d = 5$ BCC site DP, $d = 6$ SC site DP and $d = 7$ BCC bond DP. The values of c_1 , y_u and h_1 are our best estimates, taken from Tables 3.1, 3.2 and 3.3. The three curves show the Monte Carlo data corresponding to the central value of our estimated p_c , and the central value of p_c plus or minus three error bars (from Table 3.4). The curve corresponding to p_c is plotted with its statistical error, corresponding to one standard error.	59
3.6	(Color online) Plot of $1/p_c$ versus coordination number λ for bond and site DP on the BCC lattice. The lines are obtained by fitting (3.3.5) to the $d \geq 4$ data. The inset shows the analogous plot for the SC lattice.	60

3.7	(Color online) Log-log plots of $t^{y_{\mathcal{N}}} p_{\mathcal{N}}(t, s)$ versus $s/t^{y_{\mathcal{N}}}$, and $t^{y_{\mathcal{R}}} p_{\mathcal{R}}(t, s)$ versus $s/t^{y_{\mathcal{R}}}$. The subfigures (a) to (f) respectively correspond to $p_{\mathcal{N}}(t, s)$ for $d = 1$, $p_{\mathcal{R}}(t, s)$ for $d = 1$, $p_{\mathcal{N}}(t, s)$ for $d = 4$, $p_{\mathcal{R}}(t, s)$ for $d = 4$, $p_{\mathcal{N}}(t, s)$ for $d = 5$ and $p_{\mathcal{R}}(t, s)$ for $d = 5$. The data correspond to bond DP on the square lattice ($d = 1$) and BCC lattice ($d = 4, 5$). The exponents $y_{\mathcal{N}} = \theta + \delta$ and $y_{\mathcal{R}} = 1/z$ are calculated from Table 3.9 for $d = 1$, and are given by the exact mean-field values for $d = 4$ and 5. The dashed lines have slopes equal to $1/y_{\mathcal{N}} - 1$ and $1/y_{\mathcal{R}} - 1 + d$ for $p_{\mathcal{N}}(t, s)$ and $p_{\mathcal{R}}(t, s)$, respectively.	62
3.8	Plots of triangular, honeycomb, and kagome lattices.	65
4.1	(Color Online). Decomposition of a percolation configuration into leaf-free and bridge-free configurations. Periodic boundary conditions are applied. Nonbridges are denoted by dark blue lines, branches by light blue lines, and junctions by dashed lines. The union of the nonbridges and junctions defines the leaf-free configuration. Also shown is the BKW loop configuration on the medial lattice, corresponding to the entire percolation configuration. . . .	77
4.2	(Color Online). The largest cluster in a random realization of critical square-lattice bond percolation on an $L \times L$ torus with $L = 100$. Nonbridges, junctions and branches are respectively drawn by bold, thin, and gray lines.	79
4.3	Plots of ρ_n (top), ρ_b (middle), and ρ_j (bottom) versus $L^{-5/4}$. From top to bottom, the three dashed lines respectively correspond to values $1/4$, 0.21405018 , and 0.03594979 . The statistical error of each data point is smaller than the symbol size. The straight lines are simply to guide the eye.	87

4.4	Plot of $L^{-91/48}C_{1f}$ versus $L^{-5/4}$. The statistical error of each data point is smaller than the symbol size. The straight lines are simply to guide the eye.	88
4.5	Plot of $L^{-d_B}C_{bf}$ versus $L^{-5/4}$, with $d_B = 1.643\,06, 1.643\,36$ and $1.643\,66$. The statistical error of each data point is smaller than the symbol size. The straight lines are simply to guide the eye.	89
4.6	Log-log plot of H_{1f} and H_{bf} versus L . The two dashed lines have slopes $7/4$ and $4/3$ respectively. The statistical error of each data point is smaller than the symbol size.	90
4.7	Left: Illustration of a configuration $A \subseteq E$ for which the event $\ell_1(e)$ occurs. Right: The corresponding configuration $A^* \cup e^*$ for which the event $\ell_2(e^*)$ occurs.	90
5.1	A typical configuration (denoted by bold edges) of the leaf-excluded model on a 6×6 patch of the square lattice.	101
5.2	Plots of $R^{(x)}$ and Q_1 versus v for the leaf-excluded model on the square lattice.	108
5.3	Plots of $R^{(x)}(v, L)$ versus L for fixed values of v , for the two-dimensional leaf-excluded model. The curves correspond to our preferred fit of the Monte Carlo data. The shaded grey strips indicate an interval of one error bar above and below the estimate $R_c^{(x)} = 0.5212(2)$	108
5.4	Plots of $L^{-3/4}g_{bR}^{(x)}$ and $L^{-91/48}C_1$ versus $L^{-3/2}$. The straight lines are simply to guide the eye.	110
5.5	Plots of $R^{(x)}$ and Q_1 versus v for the leaf-excluded model on the simple-cubic lattice.	111

5.6	Plots of $R^{(x)}(p, L)$ versus L for fixed values of p , for the three-dimensional leaf-excluded model. The curves correspond to our preferred fit of the Monte Carlo data. The shaded grey strips indicate an interval of one error bar above and below the estimate $R_c^{(x)} = 0.260(4)$	111
5.7	Plot of $L^{-1.1415} g_{bR}^{(x)}$ and $L^{-2.52295} C_1$ versus $L^{-1.2}$. The values of the critical exponents used on the vertical axis correspond to the estimates $y_t = 1.1415(15)$ and $y_h = 2.52295(10)$ (Wang <i>et al.</i> , 2014, 2013b). The straight lines are simply to guide the eye.	112
6.1	Plot of $g_\beta(x)$ versus x for $n = 4$. The curves from top to bottom respectively correspond to $\beta = 3.5, 3.625, 3.785, 4, 4.1$. The values of 3.625 and 3.785 are respectively the estimates of β' and β_c . The reason that $\beta_c \approx 3.785$ can be seen in Fig. 6.2	141
6.2	Plot of $A_\beta(x)$ versus x for $n = 4$. From left to right, plots respectively correspond to $\beta = 3, \beta = 3.785$, and $\beta = 4$. A first order phase transition can be seen around $\beta = 3.785$	141
6.3	Illustration of an Ising vector (top left), Potts vector (top right), super-ordered vector (bottom left), and face-cubic vector (bottom right). In each figure, the size of each ellipse represents the fractional occupation of the corresponding color, while the regions above and below the bar respectively represent spin up and down.	149
6.4	Phase diagram for the general n -component face-cubic model on the complete graph with $n = 2$. The phase diagram is rigorous except the region $-J_1 < J_2 < 0$ when $J_1 > 2$	150

6.5	Illustration of five phases by means of the function $g(J_1, x)$ and ellipse diagrams. From top to bottom, they respectively denote the disordered, Potts, face-cubic, super-ordered, and Ising phases. The curves on the left plot the function $g(J_1, x) = \log x - 2J_1 x$. On the right, we use ellipses to represent the fractional occupation of colors and in each ellipse, a bar is used to distinguish spin up and down. One can see both spin and color disorder in the disordered phase, color order but spin disorder in the Potts phase, color disorder but spin order in the Ising phase. In the face-cubic phase, color is ordered and spin is ordered in the dominant color but disordered in the other. In the super-ordered phase, both color and spin are ordered.	151
6.6	Plot of $I'(J_1, x)$ (left) and $I(J_1, x)$ (right) for $J = c/2, c$ and $3c/2$, with $c = 1$	165
6.7	Phase diagram for the general n -component face-cubic model on the complete graph with $n = 2$. A super-ordered phase is observed in the region $-J_1 < J_2 < 0$ ($J_1 > 2$) by numerically calculating the global minimums of the rate function.	166

List of Tables

- 2.1 Fits of the wrapping probabilities $R^{(x)}$, $R^{(a)}$, and $R^{(3)}$, and the ratios Q_1 and Q_2 for bond percolation. We did not obtain stable fits with y_i free for $R^{(3)}$ 25
- 2.2 Fits of the wrapping probabilities $R^{(x)}$, $R^{(a)}$, and $R^{(3)}$, and the ratios Q_1 and Q_2 for site percolation. For $R^{(x)}$ we obtain unstable results when y_i is free. 27
- 2.3 Fits of covariances $g_{bR}^{(x)}$ and $g_{sR}^{(x)}$ 30
- 2.4 Fits of C_1 and χ . The superscripts b and s denote bond and site percolation, respectively. 32
- 2.5 Fits of S . The superscripts b and s denote bond and site percolation, respectively. 33
- 2.6 Fits of ρ . The superscripts b and s denote bond and site percolation, respectively. 33
- 2.7 Summary of estimated thresholds, critical exponents, universal wrapping probabilities, and excess cluster number of bond and site percolation on the simple-cubic lattice. We note that the values of y_t and y_h in (Deng and Blöte, 2005) marked by the superscript * contained typographical errors. The final error bars reported in (Deng and Blöte, 2005) were also underestimated, taking insufficient account of systematic errors. 34

3.1	Fit results for Q_t with $d = 2, 3$ on the SC and BCC lattices. Superscripts b and s represent bond and site DP, respectively. The subscript represents the dimensionality d	51
3.2	Fit results for Q_t with $d = 4$ on the SC and BCC lattices. Superscripts b and s represent bond and site DP, respectively. The subscript represents the dimensionality d	51
3.3	Fit results for Q_t with $d = 5, 6, 7$ on the SC and BCC lattices. Superscripts b and s represent bond and site DP, respectively. The subscript represents the dimensionality d	51
3.4	Final estimates of critical thresholds for bond and site DP on the SC and BCC lattices, with $2 \leq d \leq 7$. A dash “-” implies that we are unaware of any previous estimates in the literature.	56
3.5	Estimates of a_1 and a_2 in (3.3.5), calculated from the $d \geq 4$ data. . .	58
3.6	Fits results of N_t , P_t , and R_t^2 on the BCC lattice for $d = 2$ (top) and 3 (bottom). The leading correction exponent y_u was fixed to -1	58
3.7	Final estimates of the critical exponents for $d = 2$ and 3.	61
3.8	Estimates of thresholds in (1+1) dimensions on the square, triangular, honeycomb and kagome lattices.	65
3.9	Estimates of the critical exponents for $d = 1$	65
4.1	Fit results for ρ_b , ρ_j , and ρ_n	86
4.2	Fit results for C_{lf} and C_{bf}	88
4.3	Fit results for H_{lf} and H_{bf}	90
5.1	Summary of our estimates for the thresholds v_c , critical exponents y_t and y_h , and wrapping probabilities for the leaf-excluded model. A comparison with standard bond percolation is also included. . .	113
6.1	Comparison of phases in the Ashkin-Teller model and the $n = 2$ general face-cubic model on the complete graph.	169

Chapter 1
Introduction

Chapter 1

Introduction

1.1 Percolation

Probably the simplest way to introduce phase transitions is to define the percolation model (Broadbent and Hammersley, 1957; Grimmett, 1999; Stauffer and Aharony, 2003; Bollobás and Riordan, 2006) on the square lattice. Let the graph $G = (V, E)$ denote the $L \times L$ square lattice, where $|V| = L^2$ and $|E| = 2L^2$. The percolation model is then defined as follows. Every edge on the lattice is independently visited and occupied by a bond with a probability p . A bond configuration is obtained once all edges are visited. All edges are occupied by bonds if $p = 1$, whilst none are occupied if $p = 0$. Given a bond configuration, two bonds are called connected if there exists a bond-path between them; otherwise they are not connected. A cluster is a maximal set of bonds in which all bonds are connected with each other.

Despite the simplicity of the definition, percolation has attracted much attention in both mathematics and physics, because it exhibits non-trivial phase transitions. To study the critical properties, one has to take the thermodynamic limit which

corresponds to $L \rightarrow +\infty$. For percolation, a natural question to ask is what is the probability that there exists an infinitely large cluster. For bond percolation on the square lattice, it is well known that the probability is 0 for $p \leq 1/2$ and 1 for $p > 1/2$. This means that, as p crosses $1/2$, an infinitely large cluster emerges suddenly. The threshold $p_c = 1/2$ can be easily predicted from a duality argument, but providing a mathematical proof took decades of research and was finally completed by Kesten in 1980 (Kesten, 1980). In two dimensions, exact values of thresholds are also available on certain lattices with duality properties (Essam, 1972). However, no exact results are reported in three and above dimensions. Numerous numerical results can be found in Refs. (Wang *et al.*, 2013b; Zhou *et al.*, 2012a; Martins and Plascak, 2003; Grassberger, 2003; Ballesteros *et al.*, 1999; Lorenz and Ziff, 1998a,b) and the references therein.

Close to the threshold p_c , the critical properties of percolation are believed to be universal, which means they are independent of the lattice details (like square lattice, triangular lattice, or others), but only depend on the dimensions of lattices and range of interactions. For other statistical-mechanical models with spins interactions, the critical properties also depend on the dimensions of spins. The concept of universality is used to classify the critical behaviors of various models, and each universality class is characterized by its critical exponents. To define the fundamental critical exponents for percolation, we first introduce two important quantities. The first is the probability that the origin of the lattice belongs to an infinite cluster. This quantity defines the order parameter of percolation, and behaves as a power-law in the neighbourhood of p_c ,

$$P_\infty \sim \begin{cases} 0, & p \leq p_c, \\ (p - p_c)^\beta, & p \rightarrow p_c^+. \end{cases} \quad (1.1.1)$$

Here $p \rightarrow p_c^+$ means that p approaches p_c from above. The second quantity is the correlation length ξ , which is defined via the correlation function by $\rho(r) \sim e^{-r/\xi}$ ($p \neq p_c$). The correlation function $\rho(r)$ can be interpreted as the probability that two bonds separated by a distance r are in the same cluster. Around p_c , the correlation length ξ diverges as $\xi \sim (p - p_c)^{-\nu}$. In two dimensions, the exact values of $\beta = 5/36$ and $\nu = 4/3$ are predicted by Coulomb gas arguments (Nienhuis, 1987) and conformal field theory (Cardy, 1987), which have been confirmed rigorously in the specific case of triangular-lattice site percolation (Smirnov and Werner, 2001). For dimension 3 or above, no exact results for critical exponents are available, and numerical results can be found in Refs. (Wang *et al.*, 2013b; Zhou *et al.*, 2012a; Martins and Plascak, 2003; Grassberger, 2003; Ballesteros *et al.*, 1999; Lorenz and Ziff, 1998a,b) and the references therein. At or above the upper critical dimension 6 (Toulouse, 1974), the mean-field results $\beta = 1$ and $\nu = 1/2$ are believed to hold.

Not only critical exponents are believed to be universal, but also certain amplitudes. One of the most important universal amplitudes in percolation is the crossing probability (Langlands *et al.*, 1992; Cardy, 1992). For a lattice drawn on a torus, the analogue is the wrapping probability (Langlands *et al.*, 1994). Wrapping probabilities are defined as the probability that a cluster wraps around the torus in certain specified directions. Wrapping probabilities are believed to be universal and have proved to be an effective practical means of estimating percolation thresholds. In two dimensions, the values of wrapping probabilities can be determined exactly (Pinson, 1994). Numerical results are available for three dimensions (Martins and Plascak, 2003; Wang *et al.*, 2013b), but no results are reported for higher dimensions. In addition to wrapping probabilities, another commonly studied amplitude ratio is the Binder cumulant, which is defined from the moments of cluster sizes. Let S_2 and S_4 be the second and fourth moments of

the cluster size, then the binder cumulant U is defined as

$$U = 1 - \frac{\langle S_4 \rangle}{3\langle S_2^2 \rangle^2}. \quad (1.1.2)$$

Binder cumulants have been widely used in various lattice models to estimate the critical points.

In recent decades, one of the main goals in studying percolation theory has been to understand the geometric structure of the critical percolation clusters. The early studies (Stanley, 1977) decomposed the incipient infinite cluster into backbone and dangling bonds, and further decomposed the backbone into blobs and red bonds. To define the backbone, one typically fixes two distant sites in the incipient infinite cluster. The backbone is defined as those occupied bonds in the cluster which belong to trails between the specified sites. A trail in a graph is a sequence of adjacent edges with no repetitions. The remaining bonds in the cluster are considered dangling. In the backbone, the deletion of red bonds will disconnect the specified sites. At p_c , the number of backbone bonds scales as L^{d_B} , and the number of red bonds scales as L^{d_R} . The exponents d_B and d_R are the corresponding fractal dimensions. In two dimensions, the value of d_R is predicted to be exactly $3/4$ (Nienhuis, 1984) by Coulomb gas arguments, but no exact results are known for d_B . Pursuing the exact value of d_B is one of the unsolved problems in two-dimensional percolation.

1.2 Directed percolation

As a fundamental model in non-equilibrium statistical mechanics, directed percolation (DP) has been extensively studied since it was first introduced in 1957 (Broadbent and Hammersley, 1957). In recent decades, much attention has been given to DP largely because of the conjectured universality first proposed by

Janssen and Grassberger (Janssen, 1981; Grassberger, 1982). Specifically, it is believed that any model possessing the following properties will belong to the DP universality class: short-range interactions; a continuous phase transition into a unique absorbing state; a one-component order parameter and no additional symmetries. DP can be used to model a variety of natural phenomena, including forest fires (Broadbent and Hammersley, 1957; Albano, 1994), epidemic diseases (Mollison, 1977), and transport in porous media (Bouchaud and Georges, 1990; Havlin and ben Avraham, 1987).

Although DP was originally defined by analogy with standard percolation on oriented lattices, it is most common to formulate DP as a stochastic cellular automaton. Taking DP on the square lattice for example, the oriented lattice can be obtained by partitioning the sites on the lattice into a sequence of sets $(V_t)_{t \geq 0}$. The origin “0” is the only element in V_0 which is located at the top of the oriented lattice, see Fig. 1.1. A site is in V_t if and only if the shortest path to the origin has length t . Then the DP model can be defined as a spreading process on the sites set $\{V_0, V_1, \dots\}$. Specifically, every site on the lattice is assumed to be either wet ($s = 1$) or dry ($s = 0$). At $t = 0$, a spread process starts from the wet site “0” and proceeds as follows. The process for bond and site DP are slightly different and thus we discuss them separately. For the site DP process, a site $v \in V_{t+1}$ is wet with probability p if and only if there exists at least one wet neighbor in V_t ; otherwise v is dry. For the bond DP process, the probability that a site $v \in V_{t+1}$ is wet depends on the number of wet neighbors in V_t . Denote this number by n_v , then the site v is wet with probability $1 - (1 - p)^{n_v}$. For both bond and site DP, the process from V_t to V_{t+1} is Markovian. Due to this formulation, it is typical to refer to two-dimensional DP as $(1 + 1)$ dimensional DP (space plus time).

Analogous to standard percolation, one can ask under what circumstances the growth process can last forever. For the spread process, a natural order parameter is the density of active sites at time t , denoted as ρ_t . For $p \leq p_c$, ρ_t decays to zero as

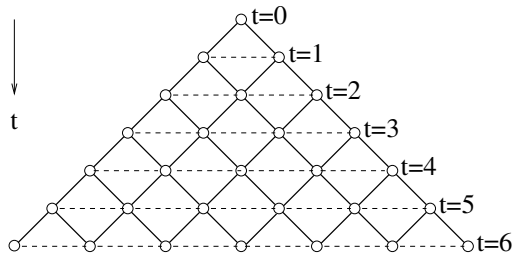


Figure 1.1: Stochastic formulation of DP on the square lattice. The vertical direction corresponds to time, and the dashed lines identify the sets V_t .

$t \rightarrow +\infty$. For $p > p_c$, ρ_t decays to a non-zero constant. Here p_c is the threshold for DP. As p approaches p_c from above, ρ_∞ decays as a power law: $\rho_\infty \sim (p - p_c)^\beta$. Due to the existence of a distinguished direction (temporal direction), the correlation length of DP is not isotropic, and thus two correlation lengths are defined: parallel to the temporal direction ξ_{\parallel} and perpendicular to the temporal direction ξ_{\perp} . Around the threshold p_c , these diverge as $\xi_{\parallel} \sim |p - p_c|^{\nu_{\parallel}}$ and $\xi_{\perp} \sim |p - p_c|^{\nu_{\perp}}$. Here $\beta, \nu_{\parallel}, \nu_{\perp}$ are three independent critical exponents for DP.

Despite of the simplicity of definition, no exact results are available for directed percolation, even in $(1 + 1)$ dimensions. Various numerical methods, including series expansions, transfer matrix, and Monte Carlo simulations, are applied to estimate critical points and exponents. Especially in $(1 + 1)$ dimensions, by series analysis (Jensen, 1996, 1999), the thresholds of several lattices have been determined to the eighth decimal place, with the critical exponents to the sixth decimal place. Estimates of thresholds and critical exponents in higher dimensions can be found in Refs. (Bleuse, 1977; Adler *et al.*, 1988; Grassberger and Zhang, 1996; Perlsman and Havlin, 2002; Lubeck and Willmann, 2004; Grassberger, 2009b,a). At and above the upper critical dimension ($d_c = 4$), mean-field values for the critical exponents $\beta = 1$, $\nu_{\parallel} = 1$, and $\nu_{\perp} = 1/2$ are believed to hold. A more detailed review for DP can be found in Ref (Hinrichsen, 2000).

1.3 The face-cubic model

The n -component general face-cubic (GFC) model was first introduced in 1975 by Kim et al (Kim *et al.*, 1975; Kim and Levy, 1975) to model the non-trivial critical behaviors of the cubic rare-earth compounds. Given a graph $G = (V, E)$, the GFC model can be defined as follows. The state space Σ consists of $2n$ n -dimensional vectors; each vector has only one non-zero entry and the entry is either 1 or -1 . For example, if $n = 1$ then $\Sigma = \{1, -1\}$, and if $n = 2$ then $\{(1, 0), (-1, 0), (0, 1), (0, -1)\}$. If one plots the $2n$ vectors in n -dimensional Cartesian coordinates, they comprise the $2n$ face centers of an n -cube centered at the origin. If $N = |V|$, then a set $\omega = \{\omega_1, \omega_2, \dots, \omega_N\}$ is a configuration, where $\omega_i \in \Sigma$ for $i = 1, \dots, N$. The GFC model is defined by randomly choosing a configuration $\omega \in \Sigma^N$ via the Gibbs measure,

$$\pi(\omega) = \frac{1}{Z(J_1, J_2)} \exp[-H(\omega)].$$

Here the Hamiltonian is defined via

$$H(\omega) = -J_1 \sum_{\alpha\beta \in E} \langle \omega_\alpha, \omega_\beta \rangle - J_2 \sum_{\alpha\beta \in E} \langle \omega_\alpha, \omega_\beta \rangle^2,$$

and $Z(J_1, J_2)$ is the partition sum

$$Z(J_1, J_2) = \sum_{\omega \in \Sigma^N} \exp[-H(\omega)].$$

We note that, without loss of generality, the parameter β (the inverse temperature) commonly appearing in the definition of Gibbs measure, is set to one.

One motivation for studying the GFC model is that many fundamental models in statistical mechanics appear as special cases. This can be partially explained from the state space Σ , which can be considered a combination of colors and spins. The $2n$ states in Σ can be classified into n colors and in each color a *spin* can point

either up or down. Specifically, two states ω_i, ω_j are said to possess the same color if $|\omega_i \cdot \omega_j| = 1$ and different colors otherwise. Analogously, two states are in the same spin states if $\omega_i \cdot \omega_j = 1$ and opposite spin states if $\omega_i \cdot \omega_j = -1$. Now let us describe some special cases of the GFC model in more detail. For $n = 1$, the GFC model reduces to the Ising model. This can be seen from the facts that the state space $\Sigma = \{1, -1\}$ and the J_2 term in the Hamiltonian becomes constant. For $n = 2$, if one redefines new variables $\tau_i, \sigma_i \in \{1, -1\}$ and writes $\omega_i = \frac{1}{2}(\tau_i + \sigma_i, \tau_i - \sigma_i)$, then the Hamiltonian of the GFC model can be rewritten as

$$H(\omega) = -\frac{J_1}{2} \sum_{ij \in E} (\tau_i \tau_j + \sigma_i \sigma_j) - \frac{J_2}{2} \sum_{ij \in E} \tau_i \tau_j \sigma_i \sigma_j - J_2 |E|/2.$$

We observe that, up to an additional constant, this is exactly the Hamiltonian for the Ashkin-Teller model (Ashkin and Teller, 1943). Other special cases can be obtained by taking special values of J_1 and J_2 . When $J_1 = 0$, the n -state Potts model is recovered, since the Hamiltonian fails to distinguish the spin states under the same color. When $J_1 = J_2$, one can verify that the Hamiltonian is non-zero iff $\omega_i = \omega_j$, which therefore corresponds to the $2n$ -state Potts model.

From these special cases of the GFC model, a natural question to ask is what is the explicit phase diagram of the GFC model on the (J_1, J_2) plane. In 1982, Nienhuis et al (Nienhuis *et al.*, 1983) studied the GFC model in two dimensions by means of renormalization group and provided a schematic phase diagram for general n . Two years later, a more detailed phase diagram on the square lattice was provided by Blöte et al (Blöte and Nightingale, 1984), in which the critical couplings and exponents were estimated using transfer matrix and finite-size scaling techniques. They also proposed a graphical representation for the GFC model such that the vector dimension n can vary continuously. In particular, on a special line on the (J_1, J_2) plane ($\cosh J_1 = e^{-J_2}$), the GFC model can be mapped exactly to a loop model. Critical points and exponents along this line were studied by Guo et al (Guo *et al.*,

2006). The mean-field approximation of the standard face-cubic model ($J_2 = 0$) was first studied by Kim et al in 1975 (Kim *et al.*, 1975). They argued that the nature of the phase transitions is continuous for $n < 3$ and of first order for $n > 3$. They also argued that for $n = 3$ the exponents are tricritical. However, the validity of the mean-field approximation was challenged by the Bethe-Peierls-Weiss and high-temperature approximations, both of which demonstrate that the transition for $n = 3$ is of first order (Kim and Levy, 1975). The phase diagram of the Ashkin-Teller model was first considered in 1980 (Ditzian *et al.*, 1980), using mean-field approximation.

Much attention has been given to study models on the complete graph, since it is possible to perform rigorous analysis. For instance, the Ising model on the complete graph has been rigorously analysed in (Ellis and Newman, 1978b,a; Ellis *et al.*, 1980). The Potts model on the complete graph was also rigorously treated by Ellis and Wang (Ellis and Wang, 1990). In recent work, we rigorously studied the standard face-cubic model on the complete graph, using a large deviation analysis. We rigorously deduced that the transition is continuous for $n \leq 3$ and of first order for $n \geq 4$. The phase diagram of the GFC model was also explicitly studied.

1.4 Thesis Outline

We list at the end of this chapter the contents of this thesis.

Chapter 2 is the published paper “Bond and site percolation in two and three dimensions” (Wang *et al.*, 2013b).

Chapter 3 is the published paper “High-precision Monte Carlo study of directed percolation in $(d + 1)$ dimensions” (Wang *et al.*, 2013a).

Chapter 4 is the published paper “Geometric structure of percolation clusters” (Xu *et al.*, 2014b).

Chapter 5 is the published paper “Leaf-excluded percolation in two and three dimensions” (Zhou *et al.*, 2015).

Chapter 6 is an unpublished paper “A n -component face-cubic model on the complete graph”, which will be submitted shortly.

Chapter 7 is Conclusion.

Declaration for Thesis Chapter 2

Declaration by candidate

In the case of Chapter 2, the nature and extent of my contribution to the work was the following:

Nature of contribution	Extent of contribution (%)
Run simulations, analyse the data, and write the article	60%

The following co-authors contributed to the work. If co-authors are students at Monash University, the extent of their contribution in percentage terms must be stated:

Name	Nature of contribution	Extent of contribution (%) for student co-authors only
Junfeng Wang	Run simulations and analyse the data	
Wei Zhang	Provide guidance and proofreading	
Timothy Garoni	Provide guidance and proofreading	
Youjin Deng	Provide guidance and proofreading	

The undersigned hereby certify that the above declaration correctly reflects the nature and extent of the candidate's and co-authors' contributions to this work*.

Candidate's Signature		Date 27/01/2016
-----------------------	---	-----------------

Main Supervisor's Signature		Date 27/01/2016
-----------------------------	---	-----------------

*Note: Where the responsible author is not the candidate's main supervisor, the main supervisor should consult with the responsible author to agree on the respective contributions of the authors.

Chapter 2
Bond and Site Percolation in Three
Dimensions

Chapter 2 is based on the article Wang J, Zhou Z, Zhang W, Garoni TM, Deng Y. 2013b. Bond and site percolation in three dimensions. Physical Review E 87: 052 107.

Abstract. *We simulate the bond and site percolation models on a simple-cubic lattice with linear sizes up to $L = 512$, and estimate the percolation thresholds to be $p_c(\text{bond}) = 0.248\,811\,82(10)$ and $p_c(\text{site}) = 0.311\,607\,7(2)$. By performing extensive simulations at these estimated critical points, we then estimate the critical exponents $1/\nu = 1.141\,0(15)$, $\beta/\nu = 0.477\,05(15)$, the leading correction exponent $\gamma_i = -1.2(2)$, and the shortest-path exponent $= 1.375\,6(3)$. Various universal amplitudes are also obtained, including wrapping probabilities, ratios associated with the cluster-size distribution, and the excess cluster number. We observe that the leading finite-size corrections in certain wrapping probabilities are governed by an exponent ≈ -2 , rather than $\gamma_i \approx -1.2$.*

Keywords. *lattice theory and statistics, critical point phenomena, percolation, equilibrium properties near critical points, critical exponents*

References are considered at the end of the thesis.

Chapter 2

Bond and Site Percolation in Three Dimensions

2.1 Introduction

Percolation (Broadbent and Hammersley, 1957) is a cornerstone of the theory of critical phenomena (Stauffer and Aharony, 1994), and a central topic in probability (Grimmett, 1999; Bollobás and Riordan, 2006). In two dimensions, Coulomb gas arguments (Nienhuis, 1987) and conformal field theory (Cardy, 1987) predict the exact values of the bulk critical exponents $\beta = 5/36$ and $\nu = 4/3$, which have been confirmed rigorously in the specific case of triangular-lattice site percolation (Smirnov and Werner, 2001). Exact values of the percolation thresholds p_c on several two-dimensional lattices are also known (Essam, 1972). In particular, it is known rigorously (Kesten, 1980) that $p_c = 1/2$ for bond percolation on the square lattice. For all d greater than or equal to the upper critical dimension (Toulouse, 1974) of $d_c = 6$, the mean-field values for the exponents $\beta = 1$ and $d\nu = 3$ are believed to hold; this has been proved rigorously (Aizenman and Newman, 1984; Hara and Slade, 1990) for $d \geq 19$.

For dimensions $2 < d < 6$ by contrast, no exact values for either the critical exponents or the percolation thresholds are known. Significant effort has therefore been expended on obtaining ever more accurate estimates, especially in three dimensions.

In addition to percolation thresholds and critical exponents, crossing probabilities (Langlands *et al.*, 1992; Cardy, 1992) also play an important role in studies of percolation. For lattices drawn on a torus, the analogous quantities are wrapping probabilities (Langlands *et al.*, 1994), and in two dimensions their values can be determined exactly (Pinson, 1994). The three-dimensional case (Martins and Plascak, 2003) has been far less studied however. Precise estimation of wrapping probabilities on the simple-cubic lattice represents one of the central undertakings of the current work.

In addition to their intrinsic importance, wrapping probabilities have proved to be an effective practical means of estimating percolation thresholds (Newman and Ziff, 2000; Feng *et al.*, 2008). Using Monte Carlo (MC) simulations and performing a careful finite-size scaling analysis of various wrapping probabilities in the neighborhood of the transition, we obtain very accurate estimates of p_c for both site and bond percolation. We observe numerically that the leading finite-size corrections for certain wrapping probabilities appear to be governed by an exponent ≈ -2 , rather than by the leading irrelevant exponent $\gamma_i \approx -1.2$.

We then estimate the thermal exponent $\gamma_t = 1/\nu$ by fixing p to our best estimate of p_c , and studying the divergence with linear size L of the derivative of the wrapping probability, which is proportional to the covariance of its indicator with the number of bonds. We find this procedure for estimating γ_t preferable to methods in which γ_t is estimated by studying how quantities behave in a neighborhood of p values around p_c . In particular, we believe the current method produces more reliable error estimates.

The remainder of this paper is organized as follows. The simulation method and the sampled quantities are discussed in Sec. 2.2. The results for the wrapping probabilities and thresholds are given in Sec. 2.3. Critical exponents and the excess cluster number are discussed in Sec. 2.4. We then finally conclude with a discussion in Sec. 2.5.

2.2 Sampled quantities

We study bond and site percolation on a periodic $L \times L \times L$ simple-cubic lattice with linear system sizes $L = 8, 12, 16, 24, 32, 48, 64, 128, 256,$ and 512 . For each system size, we produced at least 2.5×10^7 independent samples. Each independent bond (site) configuration is generated by independently occupying each bond (site) with probability p . The clusters in each configuration are identified using breadth-first search. The number of sites in each cluster defines its size.

We sampled the following observables in our simulations:

1. The number of occupied bonds \mathcal{N}_b for bond percolation, and the number of occupied sites \mathcal{N}_s for site percolation.
2. The number of clusters \mathcal{N}_c .
3. The size \mathcal{C}_1 of the largest cluster.
4. The cluster-size moments $\mathcal{S}_m = \sum_C |C|^m$ with $m = 0, 2, 4$. The sum runs over all clusters C , and \mathcal{S}_0 is simply the number of clusters.
5. An observable $\mathcal{S} := \max_C \max_{y \in C} d(x_C, y)$ used to determine the shortest-path exponent. Here $d(x, y)$ denotes the graph distance from site x to site y , and x_C is the vertex in cluster C with the smallest vertex label, according to some fixed (but arbitrary) vertex labeling.

6. The indicators $\mathcal{R}^{(x)}$, $\mathcal{R}^{(y)}$, and $\mathcal{R}^{(z)}$, for the event that a cluster wraps around the lattice in the x , y , or z direction, respectively.

From these observables we calculated the following quantities:

1. The mean size of the largest cluster $C_1 = \langle \mathcal{C}_1 \rangle$, which at p_c scales as $C_1 \sim L^{y_h}$ with $y_h = d_f = d - \beta/\nu$, where d_f is the fractal dimension.
2. The cluster density $\rho = \langle \mathcal{N}_c \rangle / L^d$.
3. The mean size of the cluster at the origin, $\chi = \langle \mathcal{S}_2 \rangle / L^d$, which at p_c scales as $\chi \sim L^{2y_h - d}$.
4. The dimensionless ratios

$$Q_1 = \frac{\langle \mathcal{C}_1 \rangle^2}{\langle \mathcal{C}_1^2 \rangle}, \quad Q_2 = \frac{\langle \mathcal{S}_2^2 \rangle}{\langle 3\mathcal{S}_2^2 - 2\mathcal{S}_4 \rangle}. \quad (2.2.1)$$

5. The shortest-path length $S = \langle \mathcal{S} \rangle$, which at p_c scales as $S \sim L^{d_{\min}}$ with d_{\min} the shortest-path fractal dimension.
6. The wrapping probabilities

$$\begin{aligned} R^{(x)} &= \langle \mathcal{R}^{(x)} \rangle = \langle \mathcal{R}^{(y)} \rangle = \langle \mathcal{R}^{(z)} \rangle, \\ R^{(a)} &= 1 - \langle (1 - \mathcal{R}^{(x)})(1 - \mathcal{R}^{(y)})(1 - \mathcal{R}^{(z)}) \rangle, \\ R^{(3)} &= \langle \mathcal{R}^{(x)} \mathcal{R}^{(y)} \mathcal{R}^{(z)} \rangle. \end{aligned} \quad (2.2.2)$$

Here $R^{(x)}$ gives the probability that a winding exists in the x direction, $R^{(a)}$ gives the probability that a winding exists in at least one of the three possible directions, and $R^{(3)}$ gives the probability that windings simultaneously exist in all three possible directions. Near p_c , we expect each of these wrapping probabilities to behave as $\sim f((p - p_c)L^{y_t})$, where f is a scaling function.

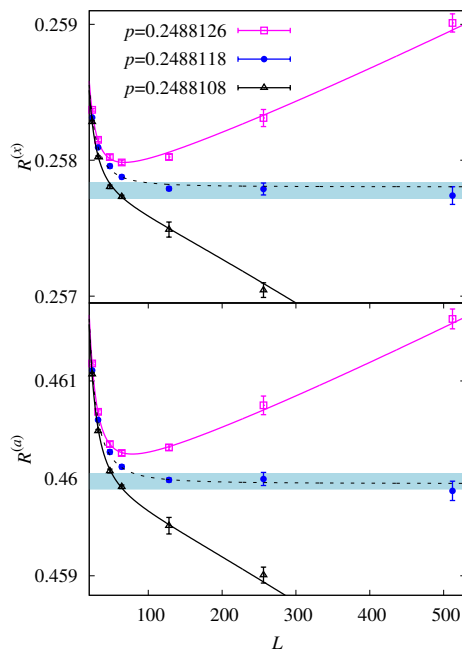


Figure 2.1: Plots of $R^{(x)}(p, L)$ (top) and $R^{(a)}(p, L)$ (bottom) vs L for fixed values of p , for bond percolation. In both cases, the curves correspond to our preferred fit of the MC data for $R(p, L)$ by the ansatz (2.3.1); the dashed curve corresponds to setting $p = 0.248\,811\,82$. The shaded blue strips indicate an interval of 1σ above and below the estimates $R_c^{(x)} = 0.257\,78(6)$ and $R_c^{(a)} = 0.459\,97(8)$.

7. The covariance of $\mathcal{R}^{(x)}$ and \mathcal{N}_b

$$\begin{aligned} g_{bR}^{(x)} &= \langle \mathcal{R}^{(x)} \mathcal{N}_b \rangle - \langle \mathcal{R}^{(x)} \rangle \langle \mathcal{N}_b \rangle \\ &= p(1-p) \frac{\partial R^{(x)}}{\partial p}. \end{aligned} \tag{2.2.3}$$

At p_c , we expect $g_{bR}^{(x)} \sim L^{\nu_t}$. An analogous definition of $g_{sR}^{(x)}$, with \mathcal{N}_b being replaced with \mathcal{N}_s , was used for site percolation.

To derive (2.2.3), one can explicitly differentiate $\langle \mathcal{R}^{(x)} \rangle$ with respect to p , and use the fact that $\langle \mathcal{N}_b \rangle = p|E|$ where $|E|$ is the total number of edges on the lattice.

The complete set of data for all observables, for both bond and site percolation, is available as Supplemental Material.

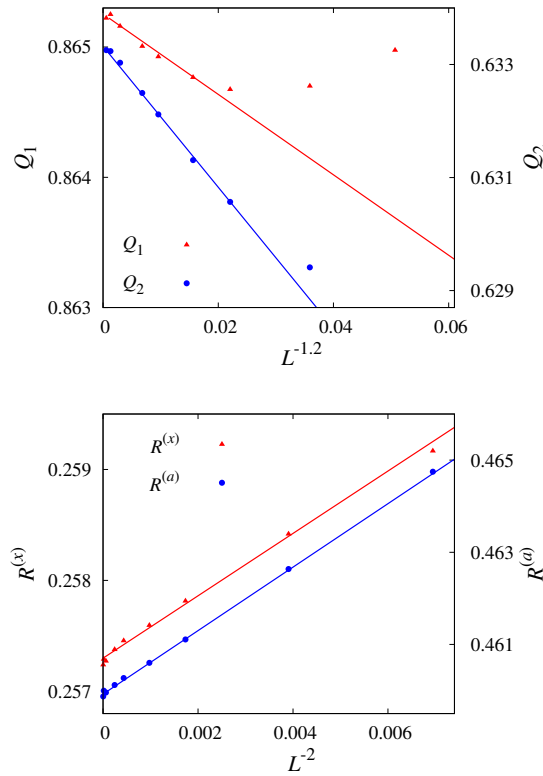


Figure 2.2: Plots of Q_1 and Q_2 vs $L^{-1.2}$ (top), and $R^{(x)}$ and $R^{(a)}$ vs L^{-2} (bottom), with $p = 0.2488118$, for bond percolation. The solid lines are simply to guide the eye.

2.3 Estimating p_c

2.3.1 Bond percolation

We estimate the thresholds of bond and site percolation by studying the finite-size scaling of the wrapping probabilities $R^{(x)}$, $R^{(a)}$, and $R^{(3)}$, and the dimensionless ratios Q_1 and Q_2 . Around p_c , we perform least-squares fits of the MC data for these quantities by the ansatz

$$\mathcal{O}(\epsilon, L) = \mathcal{O}_c + \sum_{k=1}^2 q_k \epsilon^k L^{ky_t} + b_1 L^{y_i} + b_2 L^{-2}, \quad (2.3.1)$$

Table 2.1: Fits of the wrapping probabilities $R^{(x)}$, $R^{(a)}$, and $R^{(3)}$, and the ratios Q_1 and Q_2 for bond percolation. We did not obtain stable fits with y_i free for $R^{(3)}$.

	L_{\min}	χ^2/DF	p_c	y_t	\mathcal{O}_c	q_1	b_1	y_i	b_2
Q_1	16	53/40	0.248 812 03(5)	1.16(1)	0.865 37(1)	-0.36(1)	-0.0423(5)	-1.2	0.341(5)
	24	33/33	0.248 811 98(6)	1.16(2)	0.865 35(2)	-0.31(2)	-0.040(2)	-1.2	0.31(2)
	32	28/26	0.248 811 93(7)	1.19(3)	0.865 33(2)	-0.31(3)	-0.036(3)	-1.2	0.25(5)
	16	44/39	0.248 811 84(8)	1.16(1)	0.865 39(3)	-0.36(1)	-0.10(4)	-1.34(9)	0.50(8)
	24	31/32	0.248 811 88(9)	1.19(2)	0.865 29(4)	-0.32(3)	-0.10(8)	-1.3(2)	0.5(2)
	32	28/25	0.248 811 96(14)	1.19(3)	0.865 4(2)	-0.31(3)	-0.02(4)	-1.0(5)	0.2(3)
Q_2	32	28/25	0.248 811 20(5)	1.17(2)	0.633 58(3)	-0.80(5)	-0.104(4)	-1.2	0.05(7)
	48	16/18	0.248 811 95(6)	1.14(2)	0.633 50(3)	-0.89(8)	-0.088(9)	-1.2	-0.3(2)
	64	10/11	0.248 811 84(11)	1.12(3)	0.633 4(2)	-1.0(2)	-0.05(4)	-1.2	-1(1)
	32	28/26	0.248 812 02(6)	1.17(2)	0.633 58(5)	-0.80(5)	-0.097(8)	-1.08(3)	-
	48	16/19	0.248 811 93(7)	1.14(2)	0.633 46(7)	-0.89(8)	-0.15(4)	-1.22(7)	-
	64	10/12	0.248 811 82(11)	1.12(3)	0.633 3(2)	-1.0(2)	-0.5(6)	-1.5(4)	-
$R^{(x)}$	16	41/37	0.248 811 81(4)	1.143(7)	0.257 77(2)	-1.22(3)	0.005(2)	-1.2	-0.23(1)
	24	30/31	0.248 811 83(4)	1.15(2)	0.257 78(3)	-1.22(6)	0.003(3)	-1.2	-0.26(4)
	32	25/24	0.248 811 82(6)	1.15(2)	0.257 76(5)	-1.20(8)	0.006(7)	-1.2	-0.20(10)
	16	41/37	0.248 811 82(4)	1.144(7)	0.257 79(2)	-1.22(3)	0.18(2)	-1.83(4)	-
	24	31/31	0.248 811 84(4)	1.15(2)	0.257 79(2)	-1.22(6)	0.22(8)	-1.9(2)	-
	32	25/24	0.248 811 82(6)	1.15(2)	0.257 77(4)	-1.20(8)	0.1(1)	-1.7(3)	-
$R^{(a)}$	16	40/39	0.248 811 82(4)	1.149(7)	0.459 99(3)	-1.65(4)	0.004(2)	-1.2	0.73(2)
	24	25/32	0.248 811 82(5)	1.14(2)	0.459 97(5)	-1.74(9)	0.003(4)	-1.2	0.72(6)
	32	22/25	0.248 811 83(6)	1.14(2)	0.459 98(7)	-1.7(2)	0.005(9)	-1.2	0.7(2)
	16	40/39	0.248 811 82(4)	1.149(7)	0.459 97(2)	-1.65(4)	0.81(6)	-2.06(3)	-
	24	25/32	0.248 811 82(4)	1.14(2)	0.459 95(3)	-1.74(9)	0.8(2)	-2.05(8)	-
	32	22/25	0.248 811 82(5)	1.14(2)	0.459 96(5)	-1.74(2)	1.0(9)	-2.1(3)	-
$R^{(3)}$	16	44/38	0.248 811 85(6)	1.14(1)	0.080 41(2)	-0.66(2)	0.010(1)	-1.2	-0.076(8)
	24	35/31	0.248 811 91(6)	1.15(2)	0.080 43(3)	-0.63(5)	0.007(3)	-1.2	-0.04(3)
	32	23/24	0.248 811 85(8)	1.17(3)	0.080 39(4)	-0.59(5)	0.014(6)	-1.2	-0.15(9)

where $\epsilon = p_c - p$, \mathcal{O}_c is a universal constant, and y_i is the leading correction exponent. We perform fits with both b_1 and b_2 free, as well as fits with b_2 being set identically to zero. By performing fits with y_i free we estimate that $y_i = -1.2(2)$. We also perform fits with y_i fixed to $y_i = -1.2$.

As a precaution against correction-to-scaling terms that we have neglected in our chosen ansatz, we impose a lower cutoff $L \geq L_{\min}$ on the data points admitted in the fit, and we systematically study the effect on the χ^2 value of increasing L_{\min} . In general, our preferred fit for any given ansatz corresponds to the smallest L_{\min} for which χ^2 divided by the number of degrees of freedom (DFs) is $O(1)$, and for which subsequent increases in L_{\min} do not cause χ^2 to drop by much more than one unit per degree of freedom.

Table 2.1 summarizes the results of these fits. From the fits, we can see that the finite-size corrections of Q_1 and Q_2 are dominated by the exponent $y_i \approx -1.2$. From Q_1 and Q_2 , we estimate $p_c = 0.2488119(3)$, and their universal critical values $Q_{1,c} = 0.8654(2)$ and $Q_{2,c} = 0.6335(2)$.

For $R^{(x)}$ and $R^{(a)}$, fixing $y_i = -1.2$ and including both the b_1 and b_2 terms we find that b_1 is consistent with zero, while b_2 is clearly nonzero. Furthermore, if we set $b_2 = 0$ and leave y_i free, we find $y_i \approx -2$. This suggests that either the amplitudes of the leading corrections of $R^{(x)}$ and $R^{(a)}$ vanish identically, or at least that they are sufficiently small that they cannot be detected from our data. Due to these weak finite-size corrections, the values of p_c fitted from $R^{(x)}$ and $R^{(a)}$ are much more stable than those obtained from Q_1 and Q_2 . From $R^{(x)}$ and $R^{(a)}$, we estimate $p_c = 0.24881182(10)$. For $R^{(3)}$, we report only the fits with corrections $b_1 L^{-1.2} + b_2 L^{-2}$. If y_i is left free the fits become unstable, regardless of whether the $b_2 L^{-2}$ term is included. From $R^{(3)}$, we estimate $p_c = 0.24881185(15)$ which is consistent with the value obtained from $R^{(x)}$ and $R^{(a)}$. From these fits, we estimate the universal wrapping probabilities to be $R_c^{(x)} = 0.25778(6)$, $R_c^{(a)} = 0.45997(8)$ and $R_c^{(3)} = 0.08041(8)$.

In Fig. 2.1, we illustrate our estimate of p_c by plotting $R^{(x)}$ and $R^{(a)}$ vs L . Precisely at $p = p_c$, as $L \rightarrow \infty$ the data should tend to a horizontal line, whereas the data with $p \neq p_c$ will bend upward or downward. Figure 2.1 shows that our estimate of p_c lies slightly below the central value 0.2488126 reported in Lorenz and Ziff (1998a).

In Fig. 2.2, we plot the data at $p = 0.2488118$ for $R^{(x)}$ and $R^{(a)}$ vs L^{-2} , and for Q_1 and Q_2 vs $L^{-1.2}$. The figure strongly suggests that the correction $L^{-1.2}$ dominates in Q_1 and Q_2 , but vanishes (or is very weak) in $R^{(x)}$ and $R^{(a)}$.

Table 2.2: Fits of the wrapping probabilities $R^{(x)}$, $R^{(a)}$, and $R^{(3)}$, and the ratios Q_1 and Q_2 for site percolation. For $R^{(x)}$ we obtain unstable results when y_i is free.

	L_{\min}	χ^2/DF	p_c	y_t	\mathcal{O}_c	q_1	b_1	y_i	b_2
Q_1	32	19/16	0.311 606 9(2)	1.14(2)	0.865 05(2)	-0.22(2)	0.062(2)	-1.2	0(3)
	48	11/11	0.311 607 0(2)	1.11(3)	0.865 09(3)	-0.25(3)	0.054(6)	-1.2	0.2(2)
	64	3/6	0.311 607 7(3)	1.12(6)	0.865 26(7)	-0.24(6)	0.01(2)	-1.2	1.4(5)
	32	19/16	0.311 606 9(2)	1.15(2)	0.865 06(3)	-0.22(2)	0.063(4)	-1.11(2)	-
	48	10/11	0.311 607 1(2)	1.11(3)	0.865 12(4)	-0.25(3)	0.09(2)	-1.22(7)	-
	64	3/6	0.311 607 7(3)	1.12(6)	0.865 27(5)	-0.24(6)	0.9(10)	-1.8(3)	-
Q_2	64	3/6	0.311 607 6(2)	1.12(4)	0.633 3(1)	-0.56(9)	0.02(3)	-1.2	5.1(7)
	48	13/11	0.311 607 2(1)	1.14(2)	0.633 06(4)	-0.52(4)	0.9(1)	-1.52(3)	-
	64	2/6	0.311 607 6(2)	1.12(4)	0.633 29(8)	-0.56(9)	4(2)	-1.9(2)	-
$R^{(x)}$	16	42/39	0.311 607 85(5)	1.13(1)	0.257 89(2)	-0.76(4)	0.004(1)	-1.2	-0.22(1)
	24	30/31	0.311 607 74(6)	1.14(2)	0.257 84(3)	-0.75(5)	0.009(2)	-1.2	-0.29(3)
	32	24/24	0.311 607 66(7)	1.14(2)	0.257 80(3)	-0.73(5)	0.015(4)	-1.2	-0.39(6)
$R^{(a)}$	16	39/40	0.311 607 70(5)	1.12(2)	0.460 02(2)	-1.09(6)	0.023(2)	-1.2	0.08(2)
	24	25/32	0.311 607 67(7)	1.13(2)	0.459 99(4)	-1.05(6)	0.025(3)	-1.2	0.05(4)
	32	19/24	0.311 607 65(8)	1.13(2)	0.459 98(5)	-1.06(7)	0.027(6)	-1.2	0.02(9)
	16	36/40	0.311 607 75(6)	1.12(2)	0.460 06(3)	-1.09(6)	0.055(5)	-1.33(4)	-
	24	25/32	0.311 607 68(8)	1.13(2)	0.460 01(5)	-1.05(7)	0.039(9)	-1.21(9)	-
	32	19/24	0.311 607 65(9)	1.13(2)	0.459 99(7)	-1.06(7)	0.03(2)	-1.1(2)	-
$R^{(3)}$	16	50/38	0.311 608 01(8)	1.14(2)	0.080 55(1)	-0.38(3)	-0.010(8)	-1.2	-0.30(1)
	24	27/30	0.311 607 79(9)	1.14(2)	0.080 49(2)	-0.39(4)	-0.004(2)	-1.2	-0.38(3)
	32	18/23	0.311 607 65(11)	1.15(3)	0.080 45(3)	-0.38(4)	-0.002(3)	-1.2	-0.47(5)
	16	40/38	0.311 607 89(7)	1.15(2)	0.080 510(9)	-0.38(3)	-0.21(1)	-1.77(2)	-
	24	26/30	0.311 607 77(8)	1.14(2)	0.080 48(2)	-0.39(4)	-0.30(5)	-1.88(5)	-
	32	18/23	0.311 607 66(10)	1.15(3)	0.080 46(2)	-0.38(4)	-0.6(2)	-2.1(2)	-

2.3.2 Site percolation

For site percolation, we again estimate p_c by fitting Q_1 and Q_2 , $R^{(x)}$, $R^{(a)}$, and $R^{(3)}$ with Eq. (2.3.1). The fitting procedure is similar to that of bond percolation, and the results are summarized in Table 2.2. From the table, we can see that the fits of Q_1 and Q_2 are less stable for site percolation than for bond percolation. The ratio of χ^2 per DF remains large until $L_{\min} \geq 32$ for Q_1 and $L_{\min} \geq 48$ for Q_2 , and the resulting estimates of p_c range from 0.311 606 9(2) to 0.311 607 7(3).

The fits of the wrapping probabilities are better behaved, as was the case for bond percolation. For $R^{(3)}$, fixing $y_i = -1.2$ and including both the b_1 and b_2 terms, we find that b_1 is consistent with zero, while b_2 is clearly nonzero. Furthermore, if we set $b_2 = 0$ and leave y_i free, we find $y_i \approx -2$. This suggests that the amplitude of the leading correction of $R^{(3)}$ is smaller than the resolution of our fits, and might possibly be zero. The fits of the $R^{(a)}$ data, however, quite clearly indicate

the presence of the $b_1 L^{-1.2}$ term. For $R^{(x)}$, we report only the fits with corrections $b_1 L^{-1.2} + b_2 L^{-2}$; if y_i is left free the fits become unstable, regardless of whether the $b_2 L^{-2}$ term is included. As for $R^{(a)}$, the amplitude b_1 appears to take a nonzero value. These observations suggest that the leading correction $L^{-1.2}$ does not generically vanish for all wrapping probabilities, but rather that the amplitudes in some cases are smaller than the resolution of our simulations.

Comparing the various fits, we estimate $p_c = 0.311\,6077(2)$ for site percolation, which is consistent with the previous result $0.311\,6077(4)$ (Deng and Blöte, 2005). In addition, we estimate the universal wrapping probabilities to be $R_c^{(x)} = 0.257\,82(6)$, $R_c^{(a)} = 0.459\,99(8)$, and $R_c^{(3)} = 0.080\,46(6)$, which are consistent with those estimated from bond percolation. In Fig. 2.3, we show plots of $R^{(x)}$ and $R^{(a)}$ which illustrate our estimate of p_c .

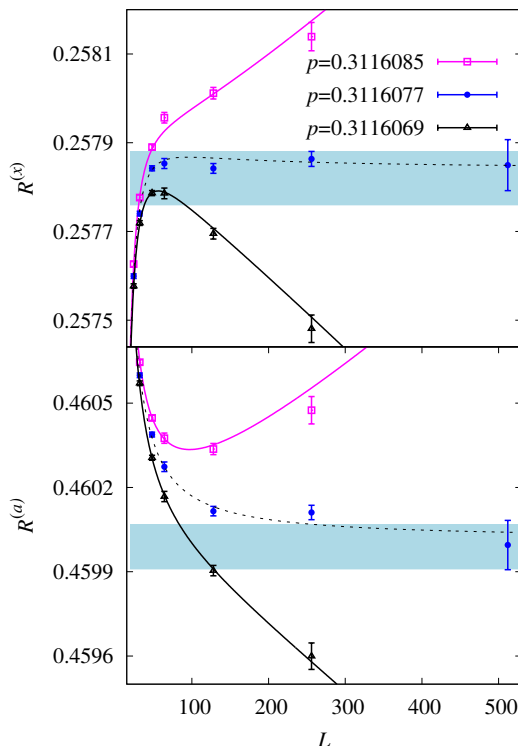


Figure 2.3: Plots of $R^{(x)}(p, L)$ (top) and $R^{(a)}(p, L)$ (bottom) vs L for fixed values of p , for site percolation. In both cases, the curves correspond to our preferred fit of the MC data for $R(p, L)$ by ansatz (2.3.1); the dashed curve corresponds to setting $p = 0.3116077$. The shaded blue strips indicate an interval of 1σ above and below the estimates $R_c^{(x)} = 0.25782(6)$ and $R_c^{(a)} = 0.45999(8)$.

2.4 Results at p_c

In this section, we estimate the critical exponents γ_t , γ_h , and d_{\min} , as well as the excess cluster number. Fixing p at our estimated thresholds for bond and site percolation, we study the covariances $g_{bR}^{(x)}$ and $g_{sR}^{(x)}$, the mean size of the largest cluster C_1 , the mean size of the cluster at the origin, χ , the shortest-path length S , and the cluster density ρ . The MC data for $g_{bR}^{(x)}$, $g_{sR}^{(x)}$, C_1 , χ and S are fitted by the ansatz

$$\mathcal{A} = L^{\gamma_A}(a_0 + b_1 L^{-1.2} + b_2 L^{-2}). \quad (2.4.1)$$

We perform fits using different combinations of the two corrections $b_1 L^{-1.2}$ and $b_2 L^{-2}$ and compare the results.

Table 2.3: Fits of covariances $g_{bR}^{(x)}$ and $g_{sR}^{(x)}$.

	L_{\min}	χ^2/DF	y_t	a_0	b_1	b_2
$g_{bR}^{(x)}$	16	4/4	1.140 4(9)	0.231(1)	-0.03(2)	0.1(2)
	24	4/3	1.140 6(13)	0.231(2)	-0.02(5)	0.0(4)
	16	4/5	1.140 9(4)	0.230 7(3)	-0.012(3)	-
	24	4/4	1.140 6(6)	0.231 1(6)	-0.017(7)	-
$g_{sR}^{(x)}$	16	5/4	1.141 6(4)	0.155 1(3)	-0.004(7)	-0.06(5)
	24	4/3	1.141 1(6)	0.155 4(6)	-0.02(2)	-0.1(2)
	16	7/5	1.141 1(2)	0.155 5(1)	-0.013(1)	-
	24	4/4	1.141 4(3)	0.155 3(2)	-0.010(2)	-

2.4.1 Estimating y_t

We estimate y_t by studying the covariances $g_{bR}^{(x)}$ and $g_{sR}^{(x)}$, both of which scale as $\sim L^{y_t}$ at the critical point. We find this procedure for estimating y_t preferable to methods, such as that employed in (Deng and Blöte, 2005), in which y_t is estimated by studying how quantities behave in the neighborhood of p_c as the system deviates from criticality. In particular, we believe the current method produces more reliable error estimates.

We fit the data for $g_{bR}^{(x)}$ at $p = 0.248\,811\,8$ and $g_{sR}^{(x)}$ at $p = 0.311\,6077$ to Eq. (2.4.1), and the results are shown in Table 2.3. The estimate of y_t from $g_{sR}^{(x)}$ produces a smaller error bar than that from $g_{bR}^{(x)}$. From these fits we take our final, somewhat conservative, estimate to be $y_t = 1.141\,0(15)$.

In Fig. 2.4, we plot $(\ln g_{bR}^{(x)} - y_t \ln L)$ and $(\ln g_{sR}^{(x)} - y_t \ln L)$ vs $\ln L$ using three different values of y_t : our estimate, as well as our estimate plus or minus three standard deviations. Using the true value of y_t should produce a horizontal line for large L . In the figure, the data using $y_t = 1.1365$ and $y_t = 1.1455$ respectively bend upward and downward, suggesting that the true value of y_t does indeed lie within 3σ of our estimate. The data with $y_t = 1.141$ appear to be consistent with an asymptotically horizontal line. We note that while the curve appears to be increasing around the point at $L = 512$ for bond percolation, it instead slightly decreases for site

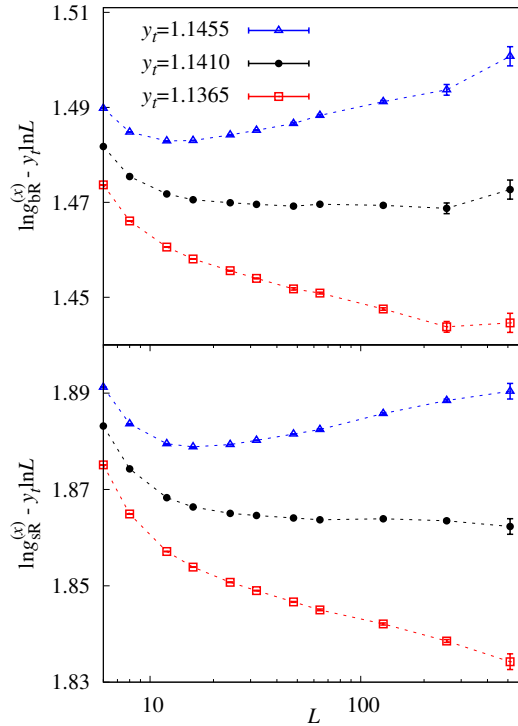


Figure 2.4: Plots of $(\ln g_{bR}^{(x)} - y_t \ln L)$ (top) and $(\ln g_{sR}^{(x)} - y_t \ln L)$ (bottom) vs $\ln L$ illustrating our estimate $y_t = 1.1410(15)$. The dashed curves are simply to guide the eye.

percolation, suggesting that in fact this movement is dominated (or even entirely caused) by noise.

2.4.2 Estimating γ_h

We estimate γ_h by studying the divergence of C_1 and χ as L increases with p fixed to our best estimates of p_c . We fit the MC data for C_1 and χ with Eq. (2.4.1), with the exponent γ_A then corresponding to γ_h and $2\gamma_h - d$, respectively. The results are reported in Table 2.4. We use superscripts b and s to distinguish bond and site percolation. For C_1^b and χ^s , the amplitude b_1 is quite small, while b_1 in χ^b and C_1^s is clearly present. In the fits of χ^s with one correction term $b_1 L^{-1.2}$, the ratio of χ^2 per DF remains large until $L_{\min} \geq 64$. We therefore show the fits with the correction $b_2 L^{-2}$ instead. Comparing these fits, we estimate $\gamma_h = 2.52295(15)$.

Table 2.4: Fits of C_1 and χ . The superscripts b and s denote bond and site percolation, respectively.

	L_{\min}	χ^2/DF	y_h	a_0	b_1	b_2
C_1^b	16	3/4	2.522 86(5)	0.939 4(3)	-0.014(6)	0.22(4)
	24	3/3	2.522 89(7)	0.939 3(4)	-0.009(11)	0.2(1)
	24	5/4	2.522 98(3)	0.938 8(2)	0.009(2)	-
	32	3/3	2.522 94(4)	0.939 0(2)	0.005(3)	-
χ^b	16	4/4	2.523 03(4)	1.125 7(5)	0.14(1)	0.18(7)
	24	3/3	2.523 00(5)	1.126 2(7)	0.12(2)	0.3(2)
	24	6/4	2.523 08(3)	1.125 1(3)	0.157(4)	-
	32	4/3	2.523 05(3)	1.125 5(4)	0.151(6)	-
C_1^s	16	5/4	2.522 99(3)	0.471 16(7)	0.024(2)	-0.44(2)
	24	5/3	2.523 00(5)	0.471 1(2)	0.024(4)	-0.45(4)
χ^s	32	0.9/2	2.522 91(5)	0.284 1(2)	-0.001(7)	-1.15(9)
	48	0.7/1	2.522 94(9)	0.284 0(4)	-0.007(18)	-1.3(3)
	32	0.9/3	2.522 92(1)	0.284 06(3)	-	-1.16(1)
	48	0.9/2	2.522 91(2)	0.284 08(7)	-	-1.17(5)

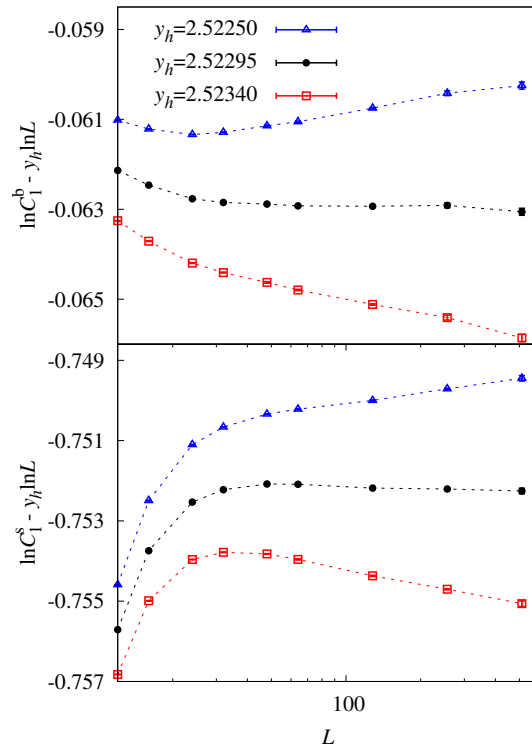

Figure 2.5: Plots of $(\ln C_1^b - y_h \ln L)$ (top) and $(\ln C_1^s - y_h \ln L)$ (bottom) vs $\ln L$ to show our estimate $y_h = 2.522 95(15)$. The dashed curves are simply to guide the eye.

Table 2.5: Fits of S . The superscripts b and s denote bond and site percolation, respectively.

	L_{\min}	χ^2/DF	d_{\min}	a_0	b_1	b_2
S^b	24	2/3	1.375 26(5)	1.814 9(5)	-0.65(2)	-3.8(2)
	32	1/2	1.375 33(7)	1.814 2(7)	-0.59(5)	-4.4(4)
	48	0/2	1.375 30(9)	1.815(1)	-0.63(9)	-4(1)
S^s	16	5/4	1.375 80(2)	1.383 4(2)	-3.432(5)	2.72(3)
	24	4/4	1.375 77(3)	1.383 6(3)	-3.45(2)	2.82(3)
	32	4/2	1.375 76(5)	1.383 7(4)	-3.45(3)	2.9(3)

Table 2.6: Fits of ρ . The superscripts b and s denote bond and site percolation, respectively.

	L_{\min}	χ^2/DF	ρ_c	b	b_1
ρ^b	16	3/5	0.272 932 83(1)	0.679(3)	0.1(6)
	24	1/4	0.272 932 83(1)	0.674(6)	3(4)
	16	2/7	0.272 932 83(1)	0.678 9(6)	-
	24	2/6	0.272 932 83(1)	0.679(2)	-
ρ^s	12	4/6	0.052 438 218(3)	0.674 5(5)	0.02(8)
	16	4/5	0.052 438 218(3)	0.674 7(8)	-0.02(21)
	24	4/4	0.052 438 218(3)	0.674(2)	0.2(10)
	12	4/7	0.052 438 218(3)	0.674 6(2)	-
	16	4/6	0.052 438 218(3)	0.674 6(3)	-
	24	4/5	0.052 438 218(3)	0.674 6(5)	-

In Fig. 2.5, we plot $(\ln C_1^b - y_h \ln L)$ and $(\ln C_1^s - y_h \ln L)$ vs $\ln L$ using three different values of y_h : our estimate, as well as our estimate plus or minus three standard deviations. As L increases, the data with $y_h = 2.52250$ and 2.52340 respectively slope upward and downward, while the data with $y_h = 2.52295$ are consistent with an asymptotically horizontal line.

2.4.3 Estimating d_{\min}

We estimate the shortest-path fractal dimension d_{\min} by studying the quantity S at our estimated thresholds. The MC data for S are fitted to Eq. (2.4.1) with the exponent y_A replaced by d_{\min} , and the results are reported in Table 2.5. We again use the superscripts b and s to distinguish bond and site percolation. In the fits, both b_1 and b_2 are clearly observable for S^b and S^s . And when we set

Table 2.7: Summary of estimated thresholds, critical exponents, universal wrapping probabilities, and excess cluster number of bond and site percolation on the simple-cubic lattice. We note that the values of γ_i and γ_h in (Deng and Blöte, 2005) marked by the superscript * contained typographical errors. The final error bars reported in (Deng and Blöte, 2005) were also underestimated, taking insufficient account of systematic errors.

Ref.	$p_c(\text{bond})$	$p_c(\text{site})$	$\gamma_i = 1/\nu$	$\gamma_h = d_f$	d_{\min}
Lorenz and Ziff (1998a)	0.248 812 6(5)		1.12(2)	2.523(4)	
Lorenz and Ziff (1998b)		0.311 608 0(4)			
Ballesteros <i>et al.</i> (1999)		0.311 608 1(13)	1.141(2)	2.523 0(3)	
Martins and Plascak (2003)	0.249 0(2)	0.311 5(3)	1.15(2)		
Deng and Blöte (2005)*		0.311 607 7(4)	1.145 0(7)	2.522 6(1)	
Zhou <i>et al.</i> (2012a)	0.248 812 0(5)		1.142(3)	2.523 5(8)	
Zhou <i>et al.</i> (2012b)					1.375 6(6)
Kozlov and Laguës (2010)			1.142(8)		
This work	0.248 811 82(10)	0.311 607 7(2)	1.141 0(15)	2.522 95(15)	1.375 6(3)
Ref.	γ_i	$R^{(x)}$	$R^{(a)}$	$R^{(3)}$	b
Lorenz and Ziff (1998a)					
Lorenz and Ziff (1998b)					
Ballesteros <i>et al.</i> (1999)	-1.61(13)				
Martins and Plascak (2003)		0.265(6)	0.471(8)	0.084(4)	
Deng and Blöte (2005)*					
Zhou <i>et al.</i> (2012a)					
Zhou <i>et al.</i> (2012b)					
Kozlov and Laguës (2010)	-1.0(2)				
This work	-1.2(2)	0.257 80(6)	0.459 98(8)	0.080 44(8)	0.675(2)

$b_2 = 0$, the ratio of χ^2 per DF remains relatively large. We also did the fits by replacing the correction with b_2 by a constant term c_0 in Eq. (2.4.1), and obtained $d_{\min}(\text{bond}) = 1.375 55(6)$ and $d_{\min}(\text{site}) = 1.375 59(6)$. Comparing these fits, we estimate $d_{\min} = 1.375 6(3)$.

To illustrate this estimate, Fig. 2.6 shows a log-log plot of S versus L .

2.4.4 Excess number of clusters

The cluster density tends to a finite limit $\rho_c = \lim_{L \rightarrow \infty} \lim_{p \rightarrow p_c} \rho$ at criticality. While the value of ρ_c is non-universal, the *excess cluster number* $b := \lim_{L \rightarrow \infty} \lim_{p \rightarrow p_c} L^d (\rho - \rho_c)$ is universal Ziff *et al.* (1997). To estimate b , we study ρ with p fixed to our estimated thresholds for bond and site percolation and fit the

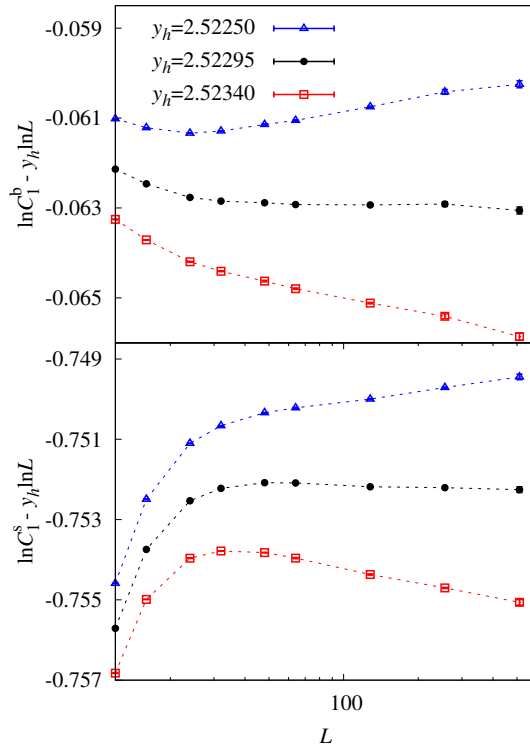


Figure 2.6: Log-log plot of S versus L for bond and site percolation. Two straight lines with slope 1.375 6 are included for comparison.

data to the ansatz

$$\rho = \rho_c + L^{-3}(b + b_1 L^{-2}). \quad (2.4.2)$$

The resulting fits are summarized in Table 2.6, where we again use superscripts b and s to differentiate the bond and site cases. We report fits both with b_1 free and with $b_1 = 0$. We find that ρ can be well fitted to (2.4.2) with $b_1 = 0$ fixed. Leaving b_1 free, we find that b_1 is consistent with zero, suggesting that the leading correction exponent might be even smaller than -2 . We also performed fits in which the leading correction exponent was fixed to -1.2 and -3 , and in both cases the resulting estimates of ρ_c and b were consistent with those reported in Table 2.6. Leaving the leading correction exponent free produces unstable fits however. Comparing these fits, we estimate $b = 0.675(2)$.

Our estimate of b is determined on the periodic $L \times L \times L$ simple cubic lattice; on the $L \times L$ square lattice $b = 0.8835(8)$ Ziff *et al.* (1997). The excess cluster number was studied in Lorenz and Ziff (1998a) on an $L \times L \times L'$ lattice with $L' \gg L$. Naively, extrapolating their results to $L' = L$ gives an estimate of $b \approx 0.412$ which is significantly below our estimate. We also note that our estimate of the number of clusters $\rho_c = 0.27293283(1)$ differs slightly from the estimate $\rho_c = 0.2729310(5)$ reported in Lorenz and Ziff (1998a).

2.5 Discussion

We study in this paper standard bond and site percolation on the three-dimensional simple-cubic lattice with periodic boundary conditions. Using extensive Monte Carlo simulations and finite-size scaling analysis, we report the estimates: $p_c = 0.24881182(10)$ (bond) and $p_c = 0.3116077(2)$ (site). The bulk thermal and magnetic exponents are estimated to be $y_t = 1.1410(15)$ and $y_h = 2.52295(15)$, the shortest-path fractal dimension to be $d_{\min} = 1.3756(3)$, and the leading irrelevant exponent to be $y_i = -1.2(2)$. The universal value of the excess cluster number is estimated to be $b = 0.675(2)$.

We emphasize that the reported estimates of p_c are obtained by studying wrapping probabilities, which are found to have weaker corrections to scaling than dimensionless ratios constructed from moments of magnetic quantities such as \mathcal{C}_1 and \mathcal{S}_m . In particular, we find evidence suggesting that the leading correction exponent in certain wrapping probabilities ($R^{(x)}$ and $R^{(a)}$ for bond percolation, $R^{(3)}$ for site percolation) may be ≈ -2 rather than -1.2 , although the reasons are not clear. The universal values of the wrapping probabilities we studied are estimated to be: $R_c^{(x)} = 0.25780(6)$, $R_c^{(a)} = 0.45998(8)$, and $R_c^{(3)} = 0.08044(8)$, by comparing the results for bond and site percolation.

From these values we can estimate other wrapping probabilities discussed in the literature, such as

$$\begin{aligned}
R^{(1)} &:= \langle \mathcal{R}^{(x)}(1 - \mathcal{R}^{(y)})(1 - \mathcal{R}^{(z)}) \rangle \\
&= \frac{1}{3}(2R^{(a)} + R^{(3)} - 3R^{(x)}), \\
R^{(2)} &:= \langle \mathcal{R}^{(x)}\mathcal{R}^{(y)}(1 - \mathcal{R}^{(z)}) \rangle \\
&= \frac{1}{3}(3R^{(x)} - 2R^{(3)} - R^{(a)}), \\
R^{(x,y)} &:= \langle \mathcal{R}^{(x)}\mathcal{R}^{(y)} \rangle = \frac{1}{3}(3R^{(x)} + R^{(3)} - R^{(a)}).
\end{aligned}$$

In words, $R^{(1)}$ is the probability that a winding exists in one given direction but not in the other two directions; $R^{(2)}$ is the probability that a winding exists in two given directions but not in the third; and $R^{(x,y)}$ is the probability that a winding exists in two given directions, regardless of whether a winding exists in the third direction. We obtain $R_c^{(1)} = 0.075\,67(14)$, $R_c^{(2)} = 0.050\,85(14)$, and $R_c^{(x,y)} = 0.131\,29(12)$.

Table 2.7 summarizes the estimates presented in this work. For comparison, we also provide an (incomplete) summary of previous estimates.

2.6 Acknowledgments

This research was supported in part by NSFC under Grants No. 91024026 and No. 11275185, and the Chinese Academy of Science. It was also supported under the Australian Research Council’s (ARC) Discovery Projects funding scheme (Project No. DP110101141), and T.G. acknowledges support from the Australian Research Council through a Future Fellowship (Project No. FT100100494). Y.D. is grateful for the hospitality of Monash University at which this work was partly completed. The simulations were carried out on the NYU-ITS cluster, which is partly supported by NSF Grant No. PHY-0424082.

Declaration for Thesis Chapter 3

Declaration by candidate

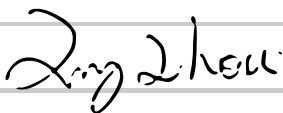
In the case of Chapter 3, the nature and extent of my contribution to the work was the following:

Nature of contribution	Extent of contribution (%)
Run simulations, analyse the data, write the article	60%

The following co-authors contributed to the work. If co-authors are students at Monash University, the extent of their contribution in percentage terms must be stated:

Name	Nature of contribution	Extent of contribution (%) for student co-authors only
Junfeng Wang	Run simulations and analyse the data	
Qingquan Liu	Proofreading and useful discussions	
Timothy Garoni	Provide guidance and proofreading	
Youjin Deng	Provide guidance and proofreading	

The undersigned hereby certify that the above declaration correctly reflects the nature and extent of the candidate's and co-authors' contributions to this work*.

Candidate's Signature		Date 27/01/2016
-----------------------	---	-----------------

Main Supervisor's Signature		Date 27/01/2016
-----------------------------	---	-----------------

*Note: Where the responsible author is not the candidate's main supervisor, the main supervisor should consult with the responsible author to agree on the respective contributions of the authors.

Chapter 3

*A high-precision Monte Carlo study
of directed percolation in $(d + 1)$
dimensions*

Chapter 3 is based on the article Wang J, Zhou Z, Liu Q, Garoni TM, Deng Y. 2013a. High-precision monte carlo study of directed percolation in $(d + 1)$ dimensions. Physical Review E 88: 042 102. Abstract.

Background: *We present a Monte Carlo study of the bond and site directed (oriented) percolation models in $(d + 1)$ dimensions on simple-cubic and body-centered-cubic lattices, with $2 \leq d \leq 7$. A dimensionless ratio is defined, and an analysis of its finite-size scaling produces improved estimates of percolation thresholds. We also report improved estimates for the standard critical exponents. In addition, we study the probability distributions of the number of wet sites and radius of gyration, for $1 \leq d \leq 7$.*

References are considered at the end of the thesis.

Chapter 3

A high-precision Monte Carlo study of directed percolation in $(d+1)$ dimensions

3.1 Introduction

Directed (or oriented) percolation (DP) is a fundamental model in non-equilibrium statistical mechanics. A variety of natural phenomena can be modeled by DP, including forest fires (Broadbent and Hammersley, 1957; Albano, 1994), epidemic diseases (Mollison, 1977), and transport in porous media (Bouchaud and Georges, 1990; Havlin and ben Avraham, 1987).

A major reason for the longstanding interest in DP is its conjectured universality, first described by Janssen (Janssen, 1981) and Grassberger (Grassberger, 1982). Specifically, it is believed that any model possessing the following properties will belong to the DP universality class: short-range interactions; a continuous phase

transition into a unique absorbing state; a one-component order parameter and no additional symmetries.

At and above the upper critical dimension ($d_c = 4$), mean-field values for the critical exponents $\beta = 1$, $\nu_{\parallel} = 1$, $\nu_{\perp} = 1/2$ are believed to hold. For $d < d_c$ however, no exact results for either critical exponents or thresholds are known, and instead one relies on numerical estimates obtained by series analysis, transfer matrix methods, and Monte Carlo simulations. In (1 + 1) dimensions, series analysis (Jensen, 1996, 1999) has enabled the threshold estimates on several lattices to be determined to the eighth decimal place, with the critical exponents being estimated to the sixth decimal place.

Estimates of thresholds and critical exponents for $d \geq 2$ can be found in (Grassberger and Zhang, 1996; Grassberger, 2009b; Perlsman and Havlin, 2002; Lubeck and Willmann, 2004; Adler *et al.*, 1988; Blease, 1977; Grassberger, 2009a). Compared with results for $d = 1$ however, the precision of these estimates in higher dimensions is less satisfactory. The central undertaking of the present work is to use high-precision Monte Carlo simulations to systematically study the thresholds of bond and site DP on simple-cubic (SC) and body-centered-cubic (BCC) lattices for $2 \leq d \leq 7$.

In order to obtain precise estimates of the critical thresholds, we study the finite-size scaling of the dimensionless ratio $Q_t = N_{2t}/N_t$, where N_t is the mean number of sites becoming wet at time t .

Having obtained these estimates for p_c , we then fix p to our best estimate of p_c and use finite-size scaling to obtain improved estimates of the critical exponents for $d = 2, 3$. In addition, we also study the finite-size scaling at p_c of the distribution

$$p_{\mathcal{N}}(t, s) := \mathbb{P}(\mathcal{N}_t = s | \mathcal{N}_t > 0), \quad (3.1.1)$$

where \mathcal{N}_t is the number of sites becoming wet at time t . We conjecture, and numerically confirm, that

$$p_{\mathcal{N}}(t, s) \sim t^{-y_{\mathcal{N}}} F_{\mathcal{N}}(s/t^{y_{\mathcal{N}}}), \quad t \rightarrow \infty, \quad (3.1.2)$$

with exponent $y_{\mathcal{N}} = \theta + \delta$, where $\theta = (d\nu_{\perp} - \beta)/\nu_{\parallel}$ and $\delta = \beta/\nu_{\parallel}$ for $d < d_c$ and $y_{\mathcal{N}} = 1$ for $d \geq d_c$. We also study an analogous distribution of the random radius of gyration, as in Eq. (3.1.2) with $y_{\mathcal{N}}$ being replaced by $y_{\mathcal{R}} = \nu_{\perp}/\nu_{\parallel}$.

The remainder of this paper is organized as follows. Section 3.2 introduces the DP models we study and describes how the simulations were performed. Results are presented in Secs. 3.3, 3.4 and 3.5. In Sec. 3.6 we present estimated thresholds of bond and site DP on the square, triangular, honeycomb and kagome lattices, while Sec. 3.7 contains some technical results justifying the definitions of the improved estimators defined in Sec. 3.2.4. We conclude with a discussion in Sec. 3.8.

3.2 Description of the model and simulations

3.2.1 Generating DP configurations

Although DP was originally introduced from a stochastic-geometric perspective (Broadbent and Hammersley, 1957), as the natural analog of isotropic percolation to oriented lattices, the most common formulation of DP is as a stochastic

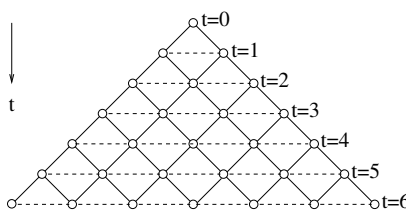


Figure 3.1: Stochastic formulation of DP on the square lattice. The vertical direction corresponds to time, and the dashed lines identify the sets V_t .

cellular automaton. To obtain a stochastic formulation of DP on a given oriented lattice, one defines a sequence $(V_t)_{t \geq 0}$ which partitions the set of lattice sites, such that each adjacent site directed to $v \in V_t$ belongs to some $V_{t'}$ with $t' < t$. See Fig. 3.1 for the example of the square lattice. By setting $V_0 = \{\mathbf{0}\}$, the trajectory of the stochastic process then generates the cluster connected to the origin. Typically $t' = t - 1$, and the resulting process is then Markovian.

For both site and bond DP, at time t the stochastic process visits each site $v \in V_t$ and sets either $s_v = 1$ (wet) or $s_v = 0$ (dry). In more detail, the process proceeds as follows. At $t = 0$, we wet the origin with probability 1. At time $t > 0$, we construct for each $v \in V_t$ the (random) set E_v of edges directed from wet sites to v . In the case of site DP, if E_v is non-empty we set $s_v = 1$ with probability p , otherwise we set $s_v = 0$. For bond DP, we select an edge $e \in E_v$ and occupy it with probability p . If e is occupied, we set $s_v = 1$, and then proceed to update the next site in V_t . If e is unoccupied, we repeat the procedure for the next edge in E_v , and continue until either an edge is occupied or the set E_v is exhausted ¹.

We note that in this description, the sets V_t have been given a pre-specified order, as have the sets of edges incident to each $v \in V_t$. The precise form of these orderings is obviously unimportant, and in practice they were induced in the natural way from the coordinates of the vertices. We used a hash table (Sedgewick, 1998) to store the wet sites in our simulations, as described in (Grassberger, 2003).

For $p > p_c$, there is a non-zero probability that the number of wet sites will diverge as $t \rightarrow \infty$. In our simulations, the cluster growth stops either at the first time that no new sites become wet, or when $t = t_{\max}$, where t_{\max} is predetermined. The values of t_{\max} used for each simulation were chosen as follows. For site and bond

¹We note that the version of bond DP that we are simulating generates a different ensemble of bond configurations compared to the standard geometric version of bond DP, in which each edge is occupied independently. However, the resulting site configurations generated by these two bond DP models are identical. Since we only consider properties of the site configurations in this article, the distinction is unimportant for our purposes. For the sake of computational efficiency, we find the version described in the text more convenient.

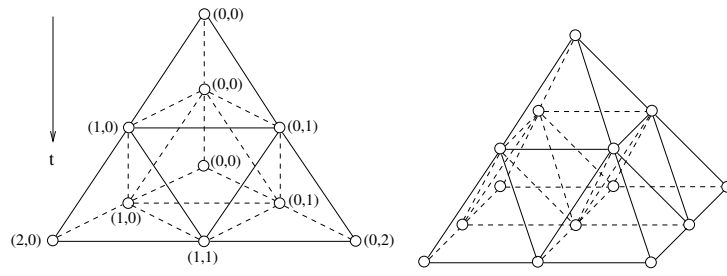


Figure 3.2: $(2+1)$ -dimensional SC (left) and BCC (right) lattices.

DP with $2 \leq d \leq 5$, we set $t_{\max} = 2^{14}$. On SC lattice with $d = 6, 7$, we set $t_{\max} = 2^{13}$ and $t_{\max} = 2^{11}$ respectively. On BCC lattice with $d = 6, 7$, we set $t_{\max} = 2^{12}$ and $t_{\max} = 2^{10}$ respectively. In all cases, the number of independent samples generated was 10^9 .

3.2.2 Lattices

We simulated $(d + 1)$ -dimensional simple-cubic (SC) and body-centered cubic (BCC) lattices with $2 \leq d \leq 7$. The stochastic processes formulation of DP on these lattices that we used in our simulations is Markovian, and is described most easily by explicitly describing the sets V_t together with the edges between V_t and V_{t+1} . In $(d + 1)$ dimensions, each $V_t \subset \mathbb{Z}^d$. Let $\mathbf{x} \in V_t$, and let $\{\mathbf{e}_1, \dots, \mathbf{e}_d\}$ denote the standard basis of \mathbb{Z}^d . On the BCC lattice, the coordinates of the $\lambda = 2^d$ neighbors of \mathbf{x} in V_{t+1} are $\mathbf{x} + \sum_{i=1}^d \alpha_i \mathbf{e}_i$ for $\alpha \in \{0, 1\}^d$. On the SC lattice, the coordinates of the $\lambda = d + 1$ neighbors of \mathbf{x} in V_{t+1} are $\mathbf{x} + \sum_{i=1}^d \alpha_i \mathbf{e}_i$ for all $\alpha \in \{0, 1\}^d$ with $\|\alpha\|_1 \leq 1$. The $(2+1)$ -dimensional cases are illustrated in Fig. 3.2.

3.2.3 Observables

For each simulation we sampled the following random variables:

1. \mathcal{N}_t , the number of sites becoming wet at time t ;

2. $\mathcal{S}_t = \sqrt{\sum_v r_v^2}$, where r_v denotes the Euclidean distance of the site v to the time axis, and the sum is over all wet sites in V_t ;
3. $\mathfrak{N}_t = \sum_{v \in V_t} b_v$, where b_v is the number of Bernoulli trials needed to determine the state of $v \in V_t$, given the configuration of sites in V_{t-1} ;
4. $\mathfrak{S}_t = \sqrt{\sum_{v \in V_t} b_v r_v^2}$.

We note that, as shown in Sec. 3.7, we have

$$\langle \mathcal{N}_t \rangle = p \langle \mathfrak{N}_t \rangle, \quad (3.2.1)$$

$$\langle \mathcal{S}_t^2 \rangle = p \langle \mathfrak{S}_t^2 \rangle, \quad (3.2.2)$$

where $\langle \cdot \rangle$ denotes the ensemble average. As explained in Section 3.2.4, \mathfrak{N}_t and \mathfrak{S}_t can be used to construct reduced-variance estimators.

Using the above random variables, we then estimated the following quantities:

1. The percolation probability $P_t = \mathbb{P}(\mathcal{N}_t > 0)$;
2. The mean number of sites becoming wet at time t , $N_t = \langle \mathcal{N}_t \rangle$;
3. The dimensionless ratio $Q_t = N_{2t}/N_t$;
4. The radius of gyration $R_t^2 = \langle \mathcal{S}_t^2 \rangle / N_t$;
5. The distribution $p_{\mathcal{N}}(t, s)$ defined by (3.1.1);
6. The distribution

$$p_{\mathcal{R}}(t, s) := \mathbb{P}(\mathcal{R}_t = s | \mathcal{N}_t > 0) \quad (3.2.3)$$

where

$$\mathcal{R}_t := \begin{cases} \frac{\mathcal{S}_t}{\sqrt{\mathcal{N}_t}}, & \mathcal{N}_t > 0, \\ 0, & \mathcal{N}_t = 0. \end{cases} \quad (3.2.4)$$

We expect the second moment of $p_{\mathcal{R}}(t, \cdot)$ to display the same critical scaling as the radius of gyration. We discuss this point further in Sec. 3.5.

3.2.4 Improved Estimators

To estimate N_t , R_t^2 and Q_t , we adopted the variance reduction technique introduced in (Grassberger, 2003, 2009a; Foster *et al.*, 2009), the details of which we now describe. To clearly distinguish sample means generated by our simulated data from the ensemble averages to which they converge, we will use $\bar{X} = \sum_{i=1}^n X^{(i)}/n$ to denote the sample mean of n independent realizations $X^{(1)}, \dots, X^{(n)}$ of the random variable X . While $\lim_{n \rightarrow \infty} \bar{X} = \langle X \rangle$, we emphasize that \bar{X} is a random variable for any finite n .

In addition to the naive estimator $\bar{\mathcal{N}}_t$, we can also estimate N_t via

$$\widehat{N}_t := p^t \prod_{t'=1}^t \frac{\bar{\mathfrak{N}}_{t'}}{\bar{\mathcal{N}}_{t'-1}}. \quad (3.2.5)$$

Indeed, taking the number of samples to infinity and using (3.2.1) we find

$$\widehat{N}_t = p^t \prod_{t'=1}^t \frac{\bar{\mathfrak{N}}_{t'}}{\bar{\mathcal{N}}_{t'-1}} \longrightarrow \prod_{t'=1}^t \frac{N_{t'}}{N_{t'-1}} = N_t. \quad (3.2.6)$$

Any convex combination of $\bar{\mathcal{N}}_t$ and the estimator (3.2.5) will therefore also be an estimator for N_t . As our final estimator for N_t we therefore used

$$\alpha \bar{\mathcal{N}}_t + (1 - \alpha) \widehat{N}_t, \quad (3.2.7)$$

with $\alpha = \alpha_{\min}$ chosen so as to minimize the variance of (3.2.7). Explicitly,

$$\alpha_{\min} = \frac{(\widehat{N}_t) - \text{cov}(\bar{\mathcal{N}}_t, \widehat{N}_t)}{(\bar{\mathcal{N}}_t) + (\widehat{N}_t) - 2\text{cov}(\bar{\mathcal{N}}_t, \widehat{N}_t)}. \quad (3.2.8)$$

Note that α_{\min} can be readily estimated from the simulation data. Similarly, to estimate Q_t we use the minimum-variance convex combination of $\overline{N}_{2t}/\overline{N}_t$ and $\widehat{N}_{2t}/\widehat{N}_t$.

An analogous estimator for R_t^2 can also be constructed:

$$\widehat{R}_t^2 = \sum_{t'=1}^t \left(\frac{\overline{\mathfrak{S}}_{t'}^2}{\overline{\mathfrak{N}}_{t'}} - \frac{\overline{\mathfrak{S}}_{t'-1}^2}{\overline{\mathfrak{N}}_{t'-1}} \right). \quad (3.2.9)$$

Taking the number of samples to infinity and using (3.2.2) shows that indeed $\widehat{R}_t^2 \rightarrow R_t^2$. Analogously to the argument above, we then take the convex combination of \widehat{R}_t^2 and $\overline{\mathfrak{S}}_t^2/\overline{N}_t$ with minimum variance to be our final estimator for R_t^2 .

We now comment on the motivation behind these definitions. For DP on a λ -ary tree we have the simple identity $\mathfrak{N}_t = \lambda \mathcal{N}_{t-1}$, which implies that \widehat{N}_t is deterministic in this case, and therefore has precisely zero variance. For DP on a $(d+1)$ -dimensional lattice, as d increases the updates become more and more like the updates for DP on the λ -ary tree, and so intuitively one expects that the variance of \widehat{N}_t should decrease as d increases. This is indeed what we observe numerically. For the simulations of bond DP on the BCC lattice for example, we find that for $d=4$ the variance of \widehat{N}_t is ≈ 0.1 of the variance of \overline{N}_t . This factor reduces to 10^{-4} for $d=7$. For low dimensions, however, the above variance reduction technique is less effective. Similar arguments and observations apply to the reduced-variance estimator for the radius of gyration. Interestingly, our data suggest that the above technique is more effective for bond DP than site DP.

	p_c	Q_c	$y_{ }$	q_1	q_2	c_1	y_u	$t_{\min}/DF/\chi^2$
SC_2^b	0.382 224 62(2)	1.173 42(4)	0.776 7(4)	-3.127(7)	2.25(3)	-0.011(1)	-0.5	64/224/175
SC_2^s	0.435 314 10(5)	1.173 42(2)	0.777 4(3)	-2.403(5)	1.37(2)	-0.025(6)	-0.48(7)	64/223/168
BCC_2^b	0.287 338 37(2)	1.173 36(2)	0.776 2(4)	-4.177(9)	4.26(4)	-6(3)	-2.1(2)	64/224/235
BCC_2^s	0.344 574 01(4)	1.173 41(2)	0.777 2(3)	-2.879(6)	1.95(2)	-0.31(2)	-0.54(7)	64/223/82
SC_3^b	0.268 356 28(1)	1.076 52(8)	0.905(4)	-3.8(2)	5.6(3)	0.005(1)	-0.3	64/223/166
SC_3^s	0.303 395 39(2)	1.075 2(4)	0.906(4)	-2.7(1)	2.9(2)	0.024(1)	-0.26(2)	64/223/367
BCC_3^b	0.132 374 169(3)	1.076 29(6)	0.904(2)	-8.5(2)	28.6(9)	-0.032(3)	-0.62(3)	64/359/341
BCC_3^s	0.160 961 28(1)	1.076 7(3)	0.904(4)	-5.0(2)	10.0(6)	0.026(1)	-0.34(2)	64/223/163

Table 3.1: Fit results for Q_t with $d = 2, 3$ on the SC and BCC lattices. Superscripts b and s represent bond and site DP, respectively. The subscript represents the dimensionality d .

	p_c	q_1	c_1	h_1	t_{\min}
SC_4^b	0.207 918 153(3)	-5.2(9)	-0.22(2)	0.50(2)	64
SC_4^s	0.231 046 861(3)	-3.83(1)	-0.53(2)	-1.2(1)	64
BCC_4^b	0.063 763 395(1)	-18.6(1)	-0.08(1)	3.34(3)	64
BCC_4^s	0.075 585 154(2)	-11.4(4)	-0.55(2)	-1.12(2)	64

Table 3.2: Fit results for Q_t with $d = 4$ on the SC and BCC lattices. Superscripts b and s represent bond and site DP, respectively. The subscript represents the dimensionality d .

	p_c	q_1	q_2	c	c_1	y_u	$t_{\min}/DF/\chi^2$
SC_5^b	0.170 615 153(1)	-5.253(5)	13.5(2)	-0.72(7)	0.026(1)	-0.49(1)	48/258/208
SC_5^s	0.186 513 581(2)	-4.115(6)	8.6(1)	-1.17(9)	0.054(1)	-0.49(1)	48/258/172
BCC_5^b	0.031 456 631 6(1)	-30.78(4)	450(6)	-1.6(7)	0.009(1)	-0.48(1)	48/248/176
BCC_5^s	0.035 972 542 1(5)	-21.17(5)	164(7)	-5.3(7)	0.049(1)	-0.48(1)	48/242/119
SC_6^b	0.145 089 946 5(4)	-6.538(2)	21.4(2)	-	0.028(1)	-0.99(1)	48/235/147
SC_6^s	0.156 547 177(3)	-5.428(4)	13.1(4)	-	0.051(3)	-0.87(2)	64/193/55
BCC_6^b	0.015 659 382 96(3)	-63.394(8)	1945(30)	-	0.003(1)	-0.99(3)	48/193/110
BCC_6^s	0.017 333 051 7(4)	-49.33(4)	1343(27)	-	0.043(1)	-0.88(2)	48/198/79
SC_7^b	0.126 387 509 0(6)	-7.663(2)	28.9(4)	-	0.015(2)	-1.32(3)	32/225/196
SC_7^s	0.135 004 173(2)	-6.566(4)	20.8(5)	-	0.092(6)	-1.45(2)	32/225/212
BCC_7^b	0.007 818 371 82(1)	-127.63(1)	7557(157)	-	0.0007(2)	-1.31(8)	32/176/171
BCC_7^s	0.008 432 989 5(3)	-107.0(2)	3882(1000)	-	0.036(5)	-1.29(4)	32/181/84

Table 3.3: Fit results for Q_t with $d = 5, 6, 7$ on the SC and BCC lattices. Superscripts b and s represent bond and site DP, respectively. The subscript represents the dimensionality d .

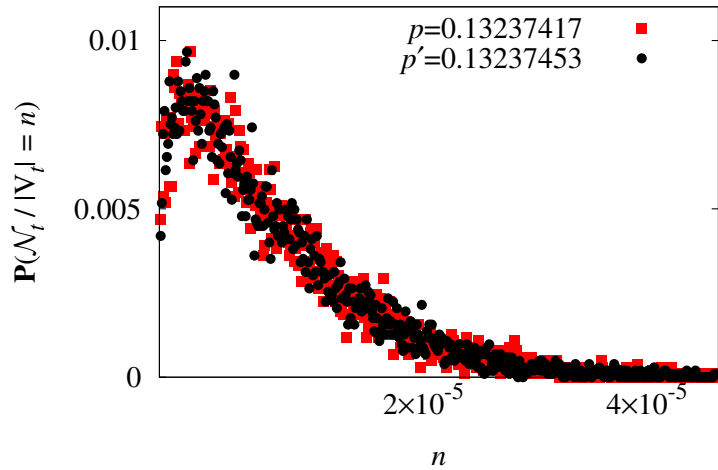


Figure 3.3: (Color online) Plot of $\mathbb{P}(\mathcal{N}_t/|V_t| = \cdot)$ at $t = 16384$ for $d = 3$ bond DP on BCC lattice, with $p = 0.13237417$ (square) and $p' = 0.13237453$ (circle).

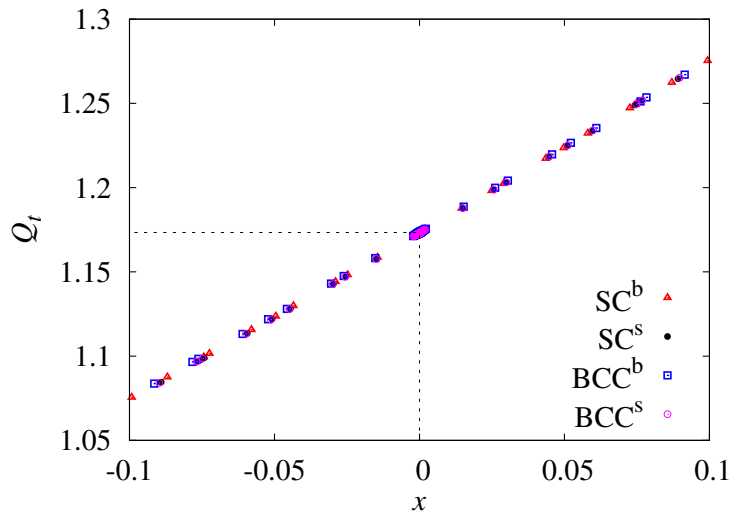


Figure 3.4: (Color online) Plot of the Q_t data for bond and site DP on the SC and BCC lattices versus $x = q_1(p_c - p)t^{2/3}$ for $d = 2$.

3.3 Percolation Thresholds

3.3.1 Fitting Methodology

To estimate the critical threshold p_c we applied an iterative approach. We ran preliminary simulations at several values of p and relatively small values of t_{\max} , and used these data to estimate p_c by studying the finite-size scaling of Q_t . Further

simulations were then performed at and near the value of p_c estimated in the initial runs, using somewhat larger values of t_{\max} . For both site and bond DP, and for each choice of lattice and dimension, this procedure was iterated a number of times before we performed our final high-precision runs at the single value of p which corresponded to the best estimate of p_c obtained in the preliminary simulations. For these final simulations we used the values of t_{\max} reported in Section 3.2.1.

For computational efficiency, we then used re-weighting to obtain expectations corresponding to multiple values of p , from each of our final high-precision runs. Our approach to re-weighting is similar to that described for the contact process in (Dickman, 1999), and relies on the simple observation that for any observable \mathcal{A}_t we have the identity $\langle \mathcal{A}_t \rangle_{p'} = \langle \mathcal{W}_{p,p'} \mathcal{A}_t \rangle_p$, where the random variable $\mathcal{W}_{p,p'}$ is defined on the space of site configurations C by

$$\mathcal{W}_{p,p'}(C) = \frac{\mathbb{P}_{p'}(C)}{\mathbb{P}_p(C)} = \prod_{t=1}^{t_{\max}} \left(\frac{p'}{p} \right)^{\mathcal{N}_t(C)} \left(\frac{1-p'}{1-p} \right)^{\mathfrak{N}_t(C) - \mathcal{N}_t(C)}.$$

As with any application of re-weighting, in practice one must of course be careful that the distributions $\mathbb{P}_p(\cdot)$ and $\mathbb{P}_{p'}(\cdot)$ have sufficient overlap, so that a finite simulation with parameter p will generate sufficiently many samples in the neighbourhood of the peak of $\mathbb{P}_{p'}(\cdot)$. As t increases, the range of acceptable p' values is expected to decrease. To verify that we had sufficient overlap, for both bond and site DP and for each choice of lattice and dimension, we performed additional low-statistics simulations (10^7 independent samples, rather than 10^9) for the p' values furthest from p , and compared the histograms generated at $t = t_{\max}$ for simulations at p' with those generated at p . In all cases the overlap was excellent. Figure 3.3 gives a typical example, showing the estimated distribution $\mathbb{P}(\mathcal{N}_t/|V_t| = \cdot)$ at $t = 16384$ for $d = 3$ bond DP on the BCC lattice, with $p = 0.13237417$ and $p' = 0.13237453$.

These final high-precision data sets were then used to perform our final fits for p_c , which we report in Tables 3.1, 3.2 and 3.3. Specifically, we performed least-squares fits of the Q_t data to an appropriate finite-size scaling ansatz. As a precaution against correction-to-scaling terms that we failed to include in the chosen ansatz, we imposed a lower cutoff $t > t_{\min}$ on the data points admitted in the fit, and we systematically studied the effect on the χ^2 value of increasing t_{\min} . In general, our preferred fit for any given ansatz corresponds to the smallest t_{\min} for which the goodness of fit is reasonable and for which subsequent increases in t_{\min} do not cause the χ^2 value to drop by vastly more than one unit per degree of freedom. In practice, by “reasonable” we mean that $\chi^2/\text{DF} \lesssim 1$, where DF is the number of degrees of freedom.

In Table 3.1, 3.2 and 3.3, we list the results for our preferred fits for Q_t , with d from 2 to 7. The superscripts “b” and “s” are used in these tables to distinguish the bond and site DP, and the subscript denotes the dimensionality d . The error bars reported in Tables 3.1, 3.2 and 3.3 correspond to statistical error only. To estimate the systematic error in our estimates of p_c we studied the robustness of the fits to variations in the terms retained in the fitting ansatz and in t_{\min} . This produced the final estimates of the critical thresholds shown in Table 3.4.

3.3.2 Results for $d = 2, 3$

Near the critical point p_c , we expect that

$$Q_t(p) = \tilde{Q}(vt^{y_{\parallel}}, ut^{y_u}), \quad (3.3.1)$$

where v and u represent the amplitudes of the relevant and the leading irrelevant scaling fields, respectively, and $y_{\parallel} = 1/\nu_{\parallel}$ and $y_u < 0$ are the associated renormalization exponents. Linearizing $v \approx a_1(p_c - p)$ around $p = p_c$ we can expand Q_t

as

$$Q_t = Q_c + \sum_{k \geq 1} q_k (p_c - p)^k t^{k y_{\parallel}} + c (p_c - p) t^{y_{\parallel} + y_u} + c_1 t^{y_u} + \dots \quad (3.3.2)$$

where $Q_c = 2^\theta$ and $q_k = a_1^k \frac{\partial^k \tilde{Q}}{\partial v^k} |_{v=0}$. It follows that $q_k / (q_1)^k$ is a universal quantity. In practice, we neglected terms higher than cubic in the finite-size scaling variable $(p_c - p) t^{y_{\parallel}}$.

We fitted our data for Q_t to the ansatz (3.3.2) as described above, and the results are reported in Table 3.1. From the fits for site DP, we observe that on both the SC and BCC lattices, the leading correction exponent $y_u \approx -0.5$ for $d = 2$, and $y_u \approx -0.3$ for $d = 3$. However, for bond DP on the BCC lattice, the fits yield $y_u \approx -2$ for $d = 2$, and $y_u \approx -0.6$ for $d = 3$. This suggests that, within the resolution of our simulations, the amplitude c_1 is consistent with zero in this case. For the fits for bond DP on the SC lattice, we could not obtain numerically stable fits with y_u left free, and so we instead report the results using correction terms $c_1 t^{-0.5} + c_2 t^{-2}$ for $d = 2$ and $c_1 t^{-0.3} + c_2 t^{-2}$ for $d = 3$.

For $d = 2$, we estimate $Q_c = 1.17340(6)$, $\nu_{\parallel} = 1/y_{\parallel} = 1.287(2)$, and $q_2/q_1^2 = 0.24(1)$. For $d = 3$, we estimate $Q_c = 1.076(1)$, $\nu_{\parallel} = 1/y_{\parallel} = 1.104(6)$, and $q_2/q_1^2 = 0.40(1)$.

In Fig. 3.4 we plot the Q_t data versus $q_1 (p_c - p) t^{y_{\parallel}}$, for bond and site DP on the two-dimensional SC and BCC lattices. We use the estimated value $y_{\parallel} \approx 0.777$, and q_1 and p_c are taken respectively from Table 3.1 and Table 3.4. An excellent collapse is observed in Fig. 3.4. The data for $t < 1024$ have been excluded to suppress the effects of finite-size corrections. The data collapse to a line with slope 1 clearly demonstrates universality.

Lattice	Site		Bond	
	$p_c(\text{Present})$	$p_c(\text{Previous})$	$p_c(\text{Present})$	$p_c(\text{Previous})$
$d = 2, \text{SC}$	0.435 314 11(10)	0.435 31(7) (Grassberger and Zhang, 1996)	0.382 224 62(6)	0.382 223(7) (Grassberger and Zhang, 1996)
$d = 2, \text{BCC}$	0.344 574 0(2)	0.344 573 6(3) (Grassberger, 2009b) 0.344 575(15) (Lubeck and Willmann, 2004)	0.287 338 38(4)	0.287 338 3(1) (Perlsman and Havlin, 2002) 0.287 338(3) (Grassberger and Zhang, 1996)
$d = 3, \text{SC}$	0.303 395 38(5)	0.302 5(10) (Adler et al., 1988)	0.268 356 28(5)	0.268 2(2) (Bleuse, 1977)
$d = 3, \text{BCC}$	0.160 961 28(3)	0.160 950(30) (Lubeck and Willmann, 2004)	0.132 374 17(2)	-
$d = 4, \text{SC}$	0.231 046 86(3)	-	0.207 918 16(2)	0.208 5(2) (Bleuse, 1977)
$d = 4, \text{BCC}$	0.075 585 15(1)	0.075 585 0(3) (Grassberger, 2009a) 0.075 582(17) (Lubeck and Willmann, 2004)	0.063 763 395(5)	-
$d = 5, \text{SC}$	0.186 513 58(2)	-	0.170 615 155(5)	0.171 4(1) (Bleuse, 1977)
$d = 5, \text{BCC}$	0.035 972 540(3)	0.035 967(23) (Lubeck and Willmann, 2004)	0.031 456 631 8(5)	-
$d = 6, \text{SC}$	0.156 547 18(1)	-	0.145 089 946(3)	0.145 8 (Bleuse, 1977)
$d = 6, \text{BCC}$	0.017 333 051(2)	-	0.015 659 382 96(10)	-
$d = 7, \text{SC}$	0.135 004 176(10)	-	0.126 387 509(3)	0.127 0(1) (Bleuse, 1977)
$d = 7, \text{BCC}$	0.008 432 989(2)	-	0.007 818 371 82(6)	-

Table 3.4: Final estimates of critical thresholds for bond and site DP on the SC and BCC lattices, with $2 \leq d \leq 7$. A dash “-” implies that we are unaware of any previous estimates in the literature.

3.3.3 Results for $d = 4$

At the upper critical dimension, the existence of dangerous irrelevant scaling fields typically leads to both multiplicative and additive logarithmic corrections to the mean-field behavior. Field-theoretic arguments (Janssen and Täuber, 2005; Janssen and Stenull, 2004) predict that in the neighborhood of criticality

$$N_t \sim \left(\ln \frac{t}{t_0} \right)^\alpha \Phi \left((p_c - p) t^{y_{\parallel}} \left(\ln \frac{t}{t_2} \right)^{-\alpha}, u t^{y_u} \right), \quad (3.3.3)$$

with $\alpha = 1/6$, $y_{\parallel} = 1$ and Φ a universal scaling function. From (3.3.3) we then obtain

$$Q_t = \left(1 + \frac{\ln 2}{\ln t + h_1} \right)^{1/6} + c(p_c - p) \frac{t^{1+y_u}}{(\ln t + h_2)^{1/6}} + \sum_{k \geq 1} q_k (p_c - p)^k \frac{t^k}{(\ln t + h_2)^{k/6}} + c_1 t^{y_u} + \dots \quad (3.3.4)$$

We fitted the $d = 4$ data for Q_t to the ansatz (3.3.4), and the results of our preferred fits are reported in Table 3.2. In the reported fits, we fixed $c = 0$ and $h_2 = 0$ since performing fits with them left free produced estimates for both which were consistent with zero. We could not obtain stable fits with y_u left free, and so the reported fits use $y_u = -1$; the resulting estimate of p_c was robust against variations

in the fixed value of y_u . All q_i with $i \geq 3$ were set identically to zero. In addition, to suppress the effects of various higher-order corrections associated with the deviation $|p_c - p|$, we only fitted the Q_t data corresponding to p values which were sufficiently close to p_c that q_2 was consistent with zero. Thus, in Table 3.2, we do not report estimates for q_2 .

3.3.4 Result for $d = 5, 6, 7$

For $d > d_c$, we fitted the data for Q_t to the ansatz (3.3.2) with Q_c and $y_{||}$ fixed at their mean-field values (Hinrichsen, 2000), $Q_c = 1 = y_{||}$. The results are reported in Table 3.3. Repeating the fits with Q_c and $y_{||}$ left free produced estimates in perfect agreement with the predicted values. For $d = 6$ and 7 , leaving the amplitude c free produced estimates consistent with zero, and we therefore omitted this term in the reported fits.

From Table 3.3, we observe that the universal amplitude $q_2/q_1^2 \approx 0.5$ holds for all models in $d = 5, 6$ and 7 dimensions. We also observe that the leading correction exponents y_u are $\approx -1/2, -1, -3/2$ for $d = 5, 6$, and 7 , respectively, in agreement with the field-theoretic prediction (Janssen and Täuber, 2005) of $y_u = 2 - d/2$.

3.3.5 Summary of thresholds

We summarize our final estimates of the critical thresholds for $2 \leq d \leq 7$ in Table 3.4. The error bars in these final estimates of p_c are obtained by estimating the systematic error from a comparison of the results from a number of different fits, varying both the terms retained in the fitting ansatz and the value of t_{\min} used. For comparison, we also present several previous estimates from the literature.

To illustrate the accuracy of our threshold estimates, we plot in Fig. 3.5 the data for Q_t versus t for a number of DP models. At the critical point, the data for Q_t

should tend to a horizontal line as t increases, while the data with $p \neq p_c$ will bend upwards or downwards. In each case in Fig. 3.5, the central curve corresponds to our estimated p_c , and the other two curves correspond to the p values which are the estimated p_c plus or minus three error bars.

We conclude this section with some observations regarding the p_c values reported in Table 3.4. Based on empirical observations, (Kurrer and Schulten, 1993) conjectured the ansatz

$$1/p_c \approx a_1 + a_2 \lambda, \text{ for } \lambda \gg 1, \quad (3.3.5)$$

relating p_c to the coordination number λ , when λ is large. In Fig. 3.6, we plot $1/p_c$ versus λ . We observe that on the SC lattice, the slopes for bond and site DP are approximately equal, while on the BCC lattice the bond and site cases clearly differ. In Table 3.5 we report the values of a_1 and a_2 obtained by fitting (3.3.5) to the $d \geq 4$ data for p_c from Table 3.4. From Table 3.5 we conjecture that a_2 is identical for bond and site DP on the SC lattice.

	SC ^b	SC ^s	BCC ^b	BCC ^s
a_1	-0.35(4)	-0.71(2)	-0.23(4)	-2.6(4)
a_2	1.034(5)	1.026(2)	1.0011(4)	0.946(5)

Table 3.5: Estimates of a_1 and a_2 in (3.3.5), calculated from the $d \geq 4$ data.

$\mathcal{O}(t)$	$y_{\mathcal{O}}$	c_0	c_1	c_2	t_{\min}
N_t	0.230 70(7)	0.976 0(5)	0.004(4)	4(2)	64
P_t	-0.451 1(2)	0.830 6(8)	0.83(9)	-30(5)	96
R_t^2	1.132 19(4)	1.633 7(5)	1.09(4)	-4(2)	64
N_t	0.105 58(10)	0.958 2(7)	0.33(5)	-4(2)	64
P_t	-0.740 3(3)	1.069(3)	0.6(3)	-60(12)	64
R_t^2	1.053 01(7)	2.715(2)	2.2(2)	-60(15)	128

Table 3.6: Fits results of N_t , P_t , and R_t^2 on the BCC lattice for $d = 2$ (top) and 3 (bottom). The leading correction exponent y_u was fixed to -1 .

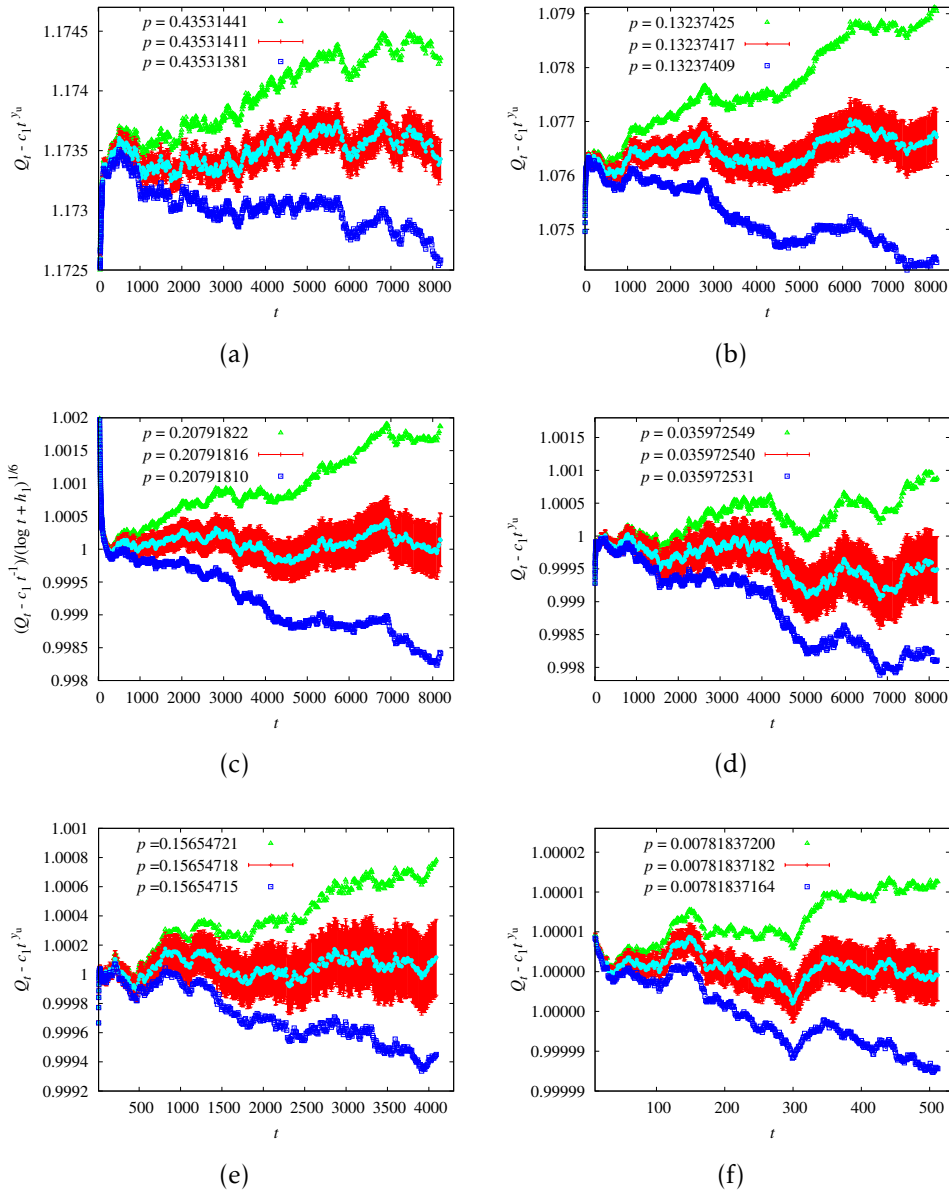


Figure 3.5: (Color online) Plots of $Q_t - c_1 t^{y_u}$ (for $d \neq 4$) and $(Q_t - c_1 t^{-1}) / (\log t + h_1)^{1/6}$ (for $d = 4$) versus t for several DP models. The subfigures (a) to (f) respectively correspond to $d = 2$ SC site DP, $d = 3$ BCC bond DP, $d = 4$ SC bond DP, $d = 5$ BCC site DP, $d = 6$ SC site DP and $d = 7$ BCC bond DP. The values of c_1 , y_u and h_1 are our best estimates, taken from Tables 3.1, 3.2 and 3.3. The three curves show the Monte Carlo data corresponding to the central value of our estimated p_c , and the central value of p_c plus or minus three error bars (from Table 3.4). The curve corresponding to p_c is plotted with its statistical error, corresponding to one standard error.

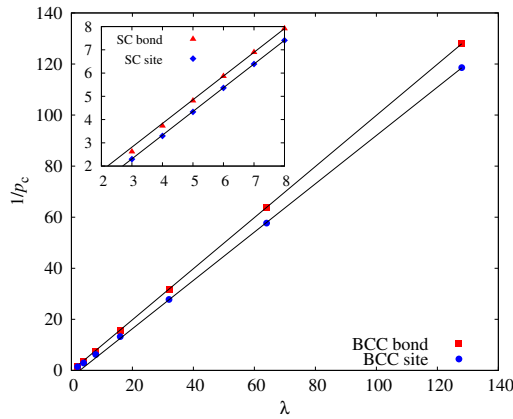


Figure 3.6: (Color online) Plot of $1/p_c$ versus coordination number λ for bond and site DP on the BCC lattice. The lines are obtained by fitting (3.3.5) to the $d \geq 4$ data. The inset shows the analogous plot for the SC lattice.

3.4 Critical Exponents

At $p = p_c$, one expects

$$P_t \sim t^{-\delta}, \quad N_t \sim t^\theta, \quad R_t^2 \sim t^{2/z}. \quad (3.4.1)$$

The critical exponents δ , θ , z are related to the standard exponents β , ν_{\parallel} , ν_{\perp} by (Hinrichsen, 2000)

$$\delta = \beta/\nu_{\parallel}, \quad \theta = (d\nu_{\perp} - 2\beta)/\nu_{\parallel}, \quad \text{and} \quad z = \nu_{\parallel}/\nu_{\perp}. \quad (3.4.2)$$

Fixing p to our best estimate of p_c from Table 3.4, we estimated the critical exponents θ , δ , and z for $d = 2$ and 3, by studying the critical scaling of N_t , P_t and R_t^2 . Specifically, we fitted the data for N_t , P_t , and R_t^2 to the ansatz

$$\mathcal{O}(t) = t^{y_{\mathcal{O}}}(c_0 + c_1 t^{y_u} + c_2 t^{-2}), \quad (3.4.3)$$

where $y_{\mathcal{O}}$ corresponds to θ , $-\delta$ and $2/z$, respectively. We focused on the case of bond DP on the BCC lattice, since we find empirically that it suffers from the

weakest corrections to scaling. In Table 3.6, we report the results of the fits with y_u fixed at -1 . To estimate the systematic error in our exponent estimates we studied the robustness of the fits to variations in the fixed value of y_u , and in t_{\min} . This produced the final exponent estimates reported in Table 3.7.

For comparison, we also report in Table 3.7 several previous exponent estimates from the literature. We note that our estimates of z and θ in (3+1) dimensions are inconsistent with the field-theoretic predictions reported in (Janssen, 1981; Bronzan and Dash, 1974).

d	Ref.	β	ν_{\parallel}	ν_{\perp}	z	θ	δ
2	Present	0.580(4)	1.287(2)	0.729(1)	1.7665(2)	0.2307(2)	0.4510(4)
	(Grassberger and Zhang, 1996)		1.295(6)		1.765(3)	0.229(3)	0.451(3)
	(Voigt and Ziff, 1997)				1.766(2)	0.229 5(10)	0.450 5(10)
	(Perlsman and Havlin, 2002)				1.766 6(10)	0.230 3(4)	0.450 9(5)
3	Present	0.818(4)	1.106(3)	0.582(2)	1.8990(4)	0.105 7(3)	0.739 8(10)
	(Jensen, 1992)	0.813(11)	1.11(1)		1.901(5)	0.114(4)	0.732(4)
	(Janssen, 1981)	0.822 05	1.105 71	0.583 60	1.887 46	0.120 84	0.737 17

Table 3.7: Final estimates of the critical exponents for $d = 2$ and 3 .

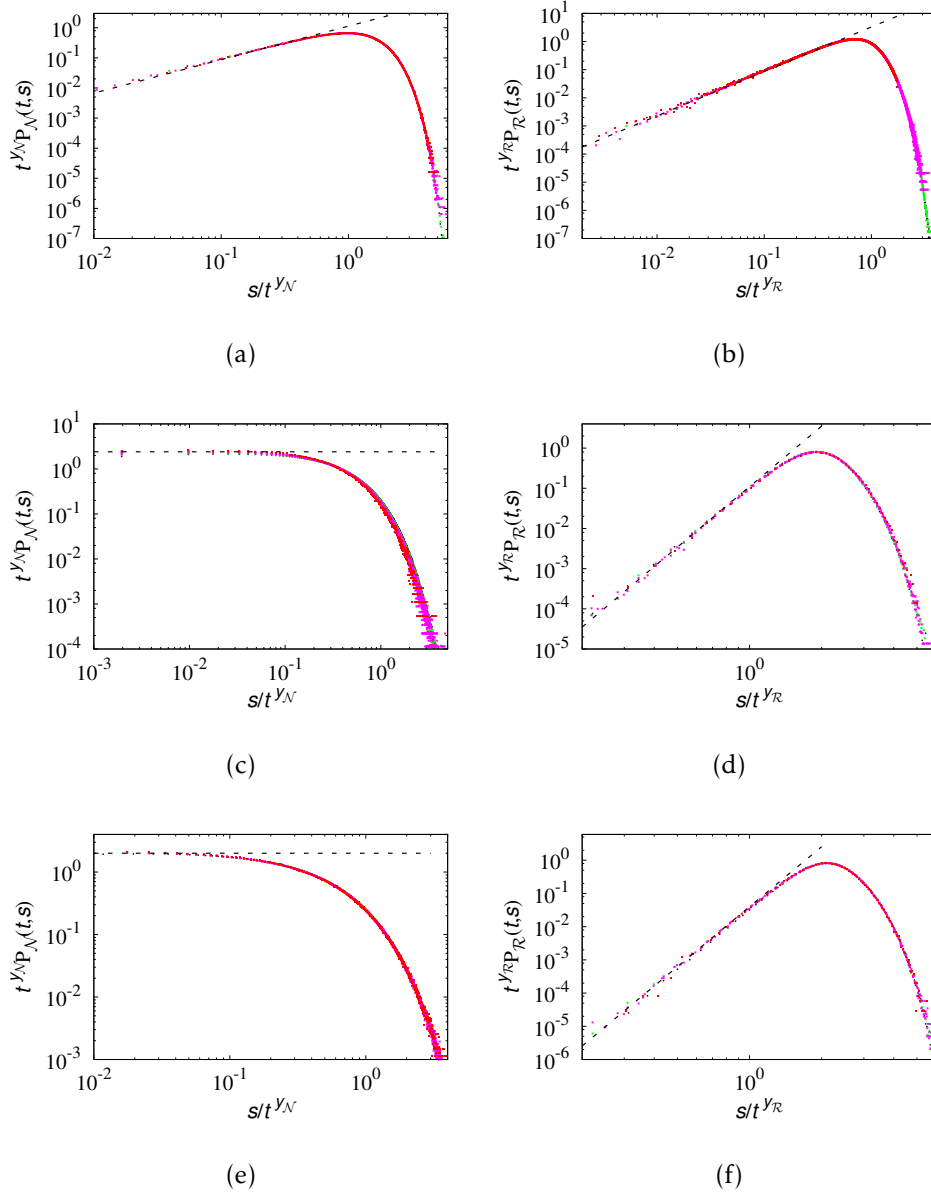


Figure 3.7: (Color online) Log-log plots of $t^{y_N} p_N(t, s)$ versus s/t^{y_N} , and $t^{y_R} p_R(t, s)$ versus s/t^{y_R} . The subfigures (a) to (f) respectively correspond to $p_N(t, s)$ for $d = 1$, $p_R(t, s)$ for $d = 1$, $p_N(t, s)$ for $d = 4$, $p_R(t, s)$ for $d = 4$, $p_N(t, s)$ for $d = 5$ and $p_R(t, s)$ for $d = 5$. The data correspond to bond DP on the square lattice ($d = 1$) and BCC lattice ($d = 4, 5$). The exponents $y_N = \theta + \delta$ and $y_R = 1/z$ are calculated from Table 3.9 for $d = 1$, and are given by the exact mean-field values for $d = 4$ and 5. The dashed lines have slopes equal to $1/y_N - 1$ and $1/y_R - 1 + d$ for $p_N(t, s)$ and $p_R(t, s)$, respectively.

3.5 Critical Distributions

In this section we consider the critical scaling of $p_{\mathcal{N}}(t, s)$ and $p_{\mathcal{R}}(t, s)$. From finite-size scaling theory, we expect that $p_{\mathcal{N}}(t, s)$ and $p_{\mathcal{R}}(t, s)$ should scale at criticality as

$$\begin{aligned} p_{\mathcal{N}}(t, s) &\sim t^{-y_{\mathcal{N}}} F_{\mathcal{N}}(s/t^{y_{\mathcal{N}}}), \\ p_{\mathcal{R}}(t, s) &\sim t^{-y_{\mathcal{R}}} F_{\mathcal{R}}(s/t^{y_{\mathcal{R}}}). \end{aligned} \quad (3.5.1)$$

The scaling functions $F_{\mathcal{N}}$ and $F_{\mathcal{R}}$ are expected to be universal. It follows immediately from (3.5.1) that for all $k \in \mathbb{N}$ we have

$$\begin{aligned} \langle \mathcal{N}_t^k \rangle &\sim t^{k y_{\mathcal{N}} - \delta}, \\ \langle \mathcal{R}_t^k \rangle &\sim t^{k y_{\mathcal{R}} - \delta}. \end{aligned} \quad (3.5.2)$$

Since $\langle \mathcal{N}_t \rangle \sim t^\theta$, we can then identify

$$y_{\mathcal{N}} = \theta + \delta. \quad (3.5.3)$$

Similarly, making the assumption that

$$\langle \mathcal{R}_t^2 \rangle \sim R_t^2 P_t \sim t^{2/z - \delta}$$

at criticality implies

$$y_{\mathcal{R}} = 1/z. \quad (3.5.4)$$

To test these predictions, Fig. 3.7 shows log-log plots of $t^{y_{\mathcal{N}}} p_{\mathcal{N}}(t, s)$ versus $s/t^{y_{\mathcal{N}}}$ and $t^{y_{\mathcal{R}}} p_{\mathcal{R}}(t, s)$ versus $s/t^{y_{\mathcal{R}}}$. The figures show bond DP data for the square lattice for $d = 1$ and the BCC lattice for $d = 4, 5$. For $d = 1$, we set the exponents $y_{\mathcal{N}}$ and $y_{\mathcal{R}}$ to $y_{\mathcal{N}} = 0.47314$ and $y_{\mathcal{R}} = 0.63263$, using the results from Table 3.9 in

Sec. 3.6. For $d = 4$ and 5 , the mean-field predictions $y_N = 1$ and $y_R = 1/2$ were used. In principle, logarithmic corrections should be taken into account for $d = 4$, however we did not pursue this here. The conjectures (3.5.1), (3.5.3) and (3.5.4) are strongly supported by the excellent data collapse observed in Fig. 3.7.

From Fig. 3.7, we observe that for $s/t^{y_N}, s/t^{y_R} \ll 1$, the curves appear to asymptote to a straight line. We find empirically that these slopes are well described by the expressions $1/y_N - 1$ and $1/y_R - 1 + d$, for $p_N(t, s)$ and $p_R(t, s)$ respectively. We therefore conjecture that these expressions hold exactly, and we illustrate them with the dashed lines in Fig. 3.7. As a result, the scaling forms (3.5.1) can be recast as

$$\begin{aligned} p_N(t, s) &\sim t^{-1} s^{1/y_N - 1} f_N(s/t^{y_N}), \\ p_R(t, s) &\sim t^{-1 - d y_R} s^{1/y_R - 1 + d} f_R(s/t^{y_R}), \end{aligned} \tag{3.5.5}$$

with f_N and f_R universal.

3.6 Estimates of thresholds and critical exponents in (1+1) dimensions.

In this section we report estimates of the critical thresholds and critical exponents for a number of (1 + 1)-dimensional lattices. Specifically, we simulated bond and site DP on square (Fig. 3.1), triangular, honeycomb, and kagome lattices (Fig. 3.8). On the triangular lattice, a site at time t has three neighboring sites at times $t' < t$: two at $t - 1$ and one at $t - 2$. On the honeycomb lattice, a site at an odd time t has two neighboring sites at time $t - 1$, while sites at even times have only one neighbor at time $t - 1$. On the kagome lattice, a site at an odd time t has one neighbour at time $t - 1$ and one at time $t - 2$, while sites at even times have two neighbours at time $t - 1$.

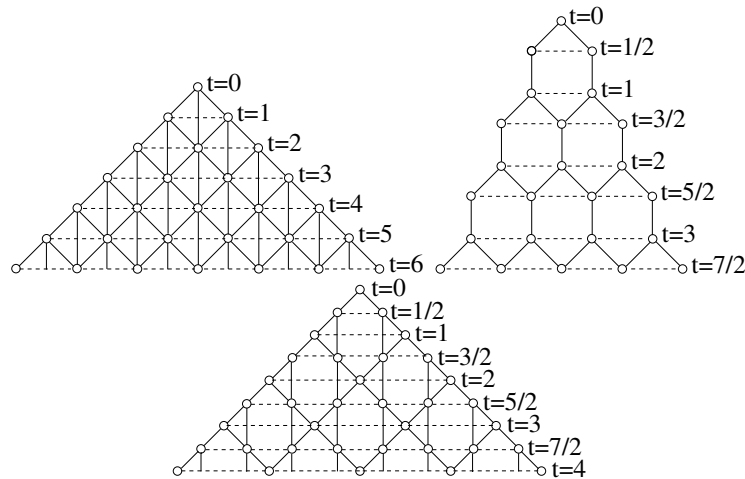


Figure 3.8: Plots of triangular, honeycomb, and kagome lattices.

The general methodology applied for these simulations is as described in Section 3.2. However we did not apply the reduced-variance estimators in this case, since their variance only becomes suppressed in high dimensions. The thresholds estimated from Q_t for $d = 1$ are shown in Table 3.8. The estimates of the critical exponents are shown in Table 3.9. These estimate are consistent with, but less precise than, results obtained previously using series analysis.

Lattice	Site		Bond	
	$p_c(\text{Present})$	$p_c(\text{Previous})$	$p_c(\text{Present})$	$p_c(\text{Previous})$
square	0.705 485 2(3)	0.705 485 22(4) (Jensen, 1999) 0.705 489(4) (Lubeck and Willmann, 2002)	0.644 700 1(2)	0.644 700 185(5) (Jensen, 1999) 0.644 700 15(5) (Jensen, 1996)
triangular	0.595 647 0(3)	0.595 646 75(10) (Jensen, 2004) 0.595 646 8(5) (Jensen, 1996)	0.478 025 0(4)	0.478 025 25(5) (Jensen, 2004) 0.478 025(1) (Jensen, 1996)
honeycomb	0.839 931 6(2)	0.839 933(5) (Jensen and Guttman, 1995)	0.822 856 9(2)	0.822 856 80(6) (Jensen, 2004)
kagome	0.736 931 7(2)	0.736 931 82(4) (Jensen, 2004)	0.658 968 9(2)	0.658 969 10(8) (Jensen, 2004)

Table 3.8: Estimates of thresholds in (1+1) dimensions on the square, triangular, honeycomb and kagome lattices.

	β	ν_{\parallel}	ν_{\perp}	z	θ	δ
Present	0.276 7(3)	1.735 5(15)	1.097 9(10)	1.580 7(2)	0.313 70(5)	0.159 44(2)
(Jensen, 1999)	0.276 486(8)	1.733 847(6)	1.096 854(4)	1.580 745(10)	0.313 686(8)	0.159 464(6)

Table 3.9: Estimates of the critical exponents for $d = 1$.

3.7 Discussion of the improved estimators

In this section we prove the identities (3.2.1) and (3.2.2). Both are direct consequences of the following lemma.

Lemma 3.7.1. *For both bond and site DP we have the following. If b_v is the number of Bernoulli trials required to determine the state of $v \in V_t$ given the site configuration at time $t - 1$, then*

$$\mathbb{P}(s_v = 1) = p \langle b_v \rangle.$$

It follows immediately from Lemma 3.7.1 that for any set of constants a_v with $v \in V_t$ we have

$$\left\langle \sum_{v \in V_t} a_v \delta_{s_v, 1} \right\rangle = p \left\langle \sum_{v \in V_t} a_v b_v \right\rangle, \quad (3.7.1)$$

where $\delta_{\cdot, \cdot}$ denotes the Kronecker delta. Choosing $a_v = 1$ in (3.7.1) gives (3.2.1), while choosing $a_v = r_v^2$ gives (3.2.2).

It now remains only to prove Lemma 3.7.1.

Proof of Lemma 3.7.1. For $v \in V_t$, let n_v denote the number of wet neighbours of v in V_{t-1} .

For site DP,

$$b_v = \begin{cases} 1, & \text{if } n_v > 0, \\ 0, & \text{if } n_v = 0, \end{cases}$$

and so $\langle b_v \rangle = \mathbb{P}(n_v > 0)$. Since $\mathbb{P}(s_v = 1) = p \mathbb{P}(n_v > 0)$, the stated result then follows.

For bond DP, the situation is more involved. Since $\mathbb{P}(s_v = 1) = \langle 1 - (1 - p)^{n_v} \rangle$, our task is to establish

$$p \langle b_v \rangle = \langle 1 - (1 - p)^{n_v} \rangle. \quad (3.7.2)$$

If we consider a fixed value of n_v , then consideration of the stochastic process defined in Section 3.2.1 shows that

$$\begin{aligned}\mathbb{E}(b_v|n_v) &= \sum_{k=1}^{n_v-1} k(1-p)^{k-1}p + n_v(1-p)^{n_v-1} \\ &= \frac{1}{p}(1 - (1-p)^{n_v}).\end{aligned}\tag{3.7.3}$$

From (3.7.3) Taking the expectation of (3.7.3) yields (3.7.2), which concludes the proof. \square

3.8 Discussion

We present a high-precision Monte Carlo study of bond and site DP on $(d + 1)$ -dimensional simple-cubic and body-centered-cubic lattices, with $2 \leq d \leq 7$. A dimensionless ratio $Q_t = N_{2t}/N_t$ constructed from the number of wet sites N_t is defined and used to estimate the critical thresholds. We report improved estimates of thresholds for $2 \leq d \leq 7$, and in high dimensions ($d > 4$) we provide estimates of p_c in several cases for which no previous estimates appear to be known. In addition, we report improved estimates of the critical exponents for $d = 2$ and 3. The accuracy of these estimates was due in part to the use of reduced-variance estimators introduced in (Grassberger, 2003, 2009a; Foster *et al.*, 2009). At the estimated thresholds, we also conjecture, and numerically confirm, the finite-size scaling of the critical probability distributions $p_{\mathcal{N}}(t, s)$ and $p_{\mathcal{R}}(t, s)$.

The high-precision Monte Carlo data reported in this work also suggests that further investigation of a number of questions is desirable. Firstly, is there an underlying physical reason (e.g. hidden symmetry) that in two and three dimensions bond DP on the BCC lattice suffers less finite-size corrections than site DP on the

BCC lattice and both site and bond DP on the SC lattice? Second, can we obtain deeper understanding of origin of the scaling behavior described by (3.5.5)?

Declaration for Thesis Chapter 4

Declaration by candidate

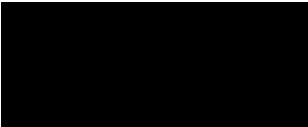
In the case of Chapter 4, the nature and extent of my contribution to the work was the following:

Nature of contribution	Extent of contribution (%)
Run simulations, analyse the data, and write the article	60%

The following co-authors contributed to the work. If co-authors are students at Monash University, the extent of their contribution in percentage terms must be stated:

Name	Nature of contribution	Extent of contribution (%) for student co-authors only
Junfeng Wang	Run simulations	
Xiao Xu	Programming and data analysis	
Timothy Garoni	Provide guidance and proofreading	
Youjin Deng	Provide guidance and proofreading	

The undersigned hereby certify that the above declaration correctly reflects the nature and extent of the candidate's and co-authors' contributions to this work*.

Candidate's Signature		Date 27/01/2016
-----------------------	---	-----------------

Main Supervisor's Signature		Date 27/01/2016
-----------------------------	---	-----------------

*Note: Where the responsible author is not the candidate's main supervisor, the main supervisor should consult with the responsible author to agree on the respective contributions of the authors.

Chapter 4
*Geometric structure of percolation
clusters*

Chapter 4 is based on the article Xu X, Wang J, Zhou Z, Garoni TM, Deng Y. 2014b. Geometric structure of percolation clusters. Physical Review E 89: 012 120.

Abstract. *We investigate the geometric properties of percolation clusters, by studying square-lattice bond percolation on the torus. We show that the density of bridges and nonbridges both tend to 1/4 for large system sizes. Using Monte Carlo simulations, we study the probability that a given edge is not a bridge but has both its loop arcs in the same loop, and find that it is governed by the two-arm exponent. We then classify bridges into two types: branches and junctions. A bridge is a branch iff at least one of the two clusters produced by its deletion is a tree. Starting from a percolation configuration and deleting the branches results in a leaf-free configuration, while deleting all bridges produces a bridge-free configuration. Although branches account for $\approx 43\%$ of all occupied bonds, we find that the fractal dimensions of the cluster size and hull length of leaf-free configurations are consistent with those for standard percolation configurations. By contrast, we find that the fractal dimensions of the cluster size and hull length of bridge-free configurations are respectively given by the backbone and external perimeter dimensions. We estimate the backbone fractal dimension to be 1.643 36(10).*

Keywords. *Percolation; Critical Phenomena.*

References are considered at the end of the thesis.

Chapter 4

Geometric structure of percolation clusters

4.1 Introduction

One of the main goals of percolation theory (Stauffer and Aharony, 2003; Grimmett, 1999; Bollobás and Riordan, 2006) in recent decades has been to understand the geometric structure of percolation clusters. Considerable insight has been gained by decomposing the incipient infinite cluster into a *backbone* plus *dangling bonds*, and then further decomposing the backbone into *blobs* and *red bonds* (Stanley, 1977).

To define the backbone, one typically fixes two distant sites in the incipient infinite cluster, and defines the backbone to be all those occupied bonds in the cluster which belong to trails¹ between the specified sites (Herrmann and Stanley, 1984). The remaining bonds in the cluster are considered dangling.

¹A *trail* in a graph is sequence of adjacent edges, with no repetitions.

Similar definitions apply when considering spanning clusters between two opposing sides of a finite box (Grassberger, 1992); this is the so-called *busbar* geometry. The bridges² in the backbone constitute the red bonds, while the remaining bonds define the blobs. At criticality, the average size of the spanning cluster scales as L^{d_F} , with L the linear system size and d_F the fractal dimension. Similarly, the size of the backbone scales as L^{d_B} , and the number of red bonds as L^{d_R} .

While exact values for d_F and d_R are known (Nienhuis, 1984; Coniglio, 1989) (see (4.1.1)), this is not the case for d_B . In (Aizenman *et al.*, 1999) however, it was shown that $2 - d_B$ coincides with the so-called monochromatic path-crossing exponent $\hat{\chi}_l^P$ with $l = 2$. An exact characterization of $\hat{\chi}_2^P$ in terms of a second-order partial differential equation with specific boundary conditions was given in (Lawler *et al.*, 2002), for which, unfortunately, no explicit solution is currently known. The exponent $\hat{\chi}_2^P$ was estimated in (Jacobsen and Zinn-Justin, 2002) using transfer matrices, and in (Deng *et al.*, 2004) by studying a suitable correlation function via Monte Carlo simulations on the torus.

In this paper, we consider a natural partition of the edges of a percolation configuration, and study the fractal dimensions of the resulting clusters. Specifically, we classify all occupied bonds in a given configuration into three types: branches, junctions and nonbridges. A bridge is a *branch* if and only if at least one of the two clusters produced by its deletion is a tree. Junctions are those bridges which are not branches. Deleting branches from percolation configurations produces *leaf-free* configurations, and further deleting junctions from leaf-free configurations generates bridge-free configurations. These definitions are illustrated in Fig. 4.1.

It is often useful to map a bond configuration to its corresponding Baxter-Kelland-Wu (BKW) (Baxter *et al.*, 1976) loop configuration, as illustrated in Fig. 4.1. The loop configurations are drawn on the medial graph (Ellis-Monaghan and Moffatt,

²An edge in a graph is a *bridge* if its deletion increases the number of connected components.

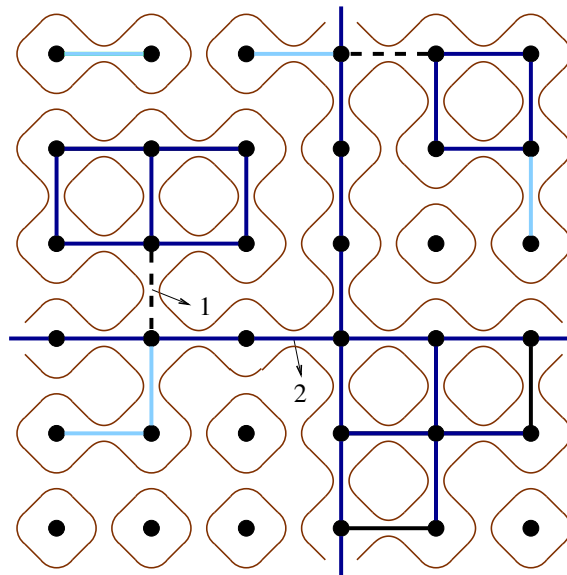


Figure 4.1: (Color Online). Decomposition of a percolation configuration into leaf-free and bridge-free configurations. Periodic boundary conditions are applied. Nonbridges are denoted by dark blue lines, branches by light blue lines, and junctions by dashed lines. The union of the nonbridges and junctions defines the leaf-free configuration. Also shown is the BKW loop configuration on the medial lattice, corresponding to the entire percolation configuration.

2013), the vertices of which correspond to the edges of the original graph. The medial graph of the square lattice is again a square lattice, rotated 45° . Each unoccupied edge of the original lattice is crossed by precisely two loop arcs, while occupied edges are crossed by none. The continuum limits of such loops are of central interest in studies of SLE (Kager and Nienhuis, 2004; Cardy, 2005). At the critical point, the mean length of the largest loop scales as L^{d_H} , with d_H the hull fractal dimension. A related concept is the accessible external perimeter (Grossman and Aharony, 1987). This can be defined as the set of sites that have non-zero probability of being visited by a random walker which is initially far from a percolating cluster. The size of the accessible external perimeter scales as L^{d_E} with $d_E \leq d_H$.

In two dimensions, Coulomb-gas arguments (Nienhuis, 1984; Saleur and Duplantier, 1987; Coniglio, 1989; Duplantier, 1999) predict the following exact

expressions for d_F , d_R , d_H and d_E

$$\begin{aligned}
 d_F &= 2 - (6 - g)(g - 2)/8g = 91/48 , \\
 d_R &= (4 - g)(4 + 3g)/8g = 3/4 , \\
 d_H &= 1 + 2/g = 7/4 , \\
 d_E &= 1 + g/8 = 4/3 ,
 \end{aligned} \tag{4.1.1}$$

where for percolation the Coulomb-gas coupling $g = 8/3$ ³. We note that the magnetic exponent $\gamma_h = d_F$, the two-arm exponent (Saleur and Duplantier, 1987) satisfies $x_2 = 2 - d_R$, and that for percolation the thermal exponent $\gamma_t = d_R$ (Coniglio, 1982; Vasseur *et al.*, 2012). The two-arm exponent gives the asymptotic decay L^{-x_2} of the probability that at least two spanning clusters join inner and outer annuli (of radii $O(1)$ and L respectively) in the plane. We also note that d_E and d_H are related by the duality transformation $g \mapsto 16/g$ (Duplantier, 2000). The most precise numerical estimate for d_B currently known is $d_B = 1.6434(2)$ (Deng *et al.*, 2004).

We study critical bond percolation on the torus \mathbb{Z}_L^2 , and show that as a consequence of self-duality the density of bridges and nonbridges both tend to $1/4$ as $L \rightarrow \infty$. Using Monte Carlo simulations, we observe that despite the fact that around 43% of all occupied edges are branches, the fractal dimension of the leaf-free clusters is simply d_F , while their hulls are governed by d_H . By contrast, the fractal dimension of the bridge-free configurations is d_B , and that of their hulls is d_E . Fig. 4.2 shows a typical realization of the largest cluster in critical square-lattice bond percolation, showing the three different types of bond present.

In more detail, our main findings are summarized as follows.

³In terms of the SLE parameter we have $\kappa = 16/g = 6$.

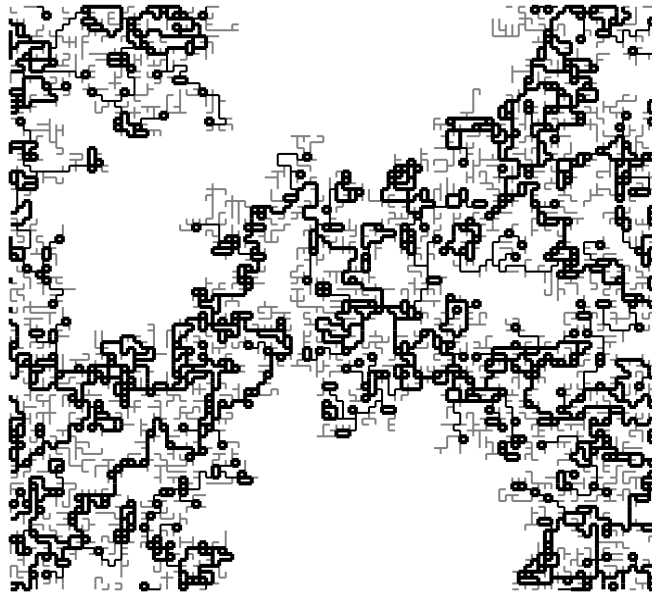


Figure 4.2: (Color Online). The largest cluster in a random realization of critical square-lattice bond percolation on an $L \times L$ torus with $L = 100$. Nonbridges, junctions and branches are respectively drawn by bold, thin, and gray lines.

1. The leading finite-size correction to the density of nonbridges scales with exponent $-5/4$, consistent with $-x_2$. It follows that the probability that a given edge is not a bridge but has both its loop arcs in the same loop decays like L^{-x_2} as $L \rightarrow \infty$. The leading finite-size correction to the density of junctions also scales with exponent $-5/4$, while the density of branches is almost independent of system size.
2. The fractal dimension of leaf-free clusters is $1.89584(4)$, consistent with $d_F = 91/48$ for percolation clusters.
3. The hull fractal dimension for leaf-free configurations is $1.74996(8)$, consistent with $d_H = 7/4$.
4. The fractal dimension for bridge-free clusters is consistent with d_B , and we provide the improved estimate $d_B = 1.64336(10)$.
5. The hull fractal dimension for bridge-free configurations is $1.3333(3)$, consistent with $d_E = 4/3$.

The remainder of this paper is organized as follows. Section 4.2 introduces the model, algorithm and sampled quantities. Numerical results are summarized and analyzed in Section 5.3. A brief discussion is given in Section 5.4.

4.2 Model, Algorithm and Observables

4.2.1 Model

We study critical bond percolation on the $L \times L$ square lattice with periodic boundary conditions, with linear system sizes $L = 8, 16, 24, 32, 48, 64, 96, 128, 256, 512, 1024, 2048,$ and 4096 . To generate a bond configuration, we independently visit each edge on the lattice and randomly place a bond with probability $p = 1/2$. For each system size, we produced at least 7×10^6 independent samples; for each $L \leq 512$ we produced more than 10^8 independent samples.

A *leaf* in a percolation configuration is a site which is adjacent to precisely one occupied bond. Given a percolation configuration we generate the corresponding *leaf-free* configuration via the following iterative procedure, often referred to as *burning*. For each leaf, we delete its adjacent bond. If this procedure generates new leaves, we repeat it until no leaves remain. The bonds which are deleted during this iterative process are precisely the branches defined in Section 6.1.

The bridges in the leaf-free configurations are the junctions. Deleting the junctions from the leaf-free configurations then produces bridge-free configurations. The algorithm we used to efficiently identify junctions in leaf-free configurations is described in Sec. 4.2.2.

4.2.2 Algorithm

Given an arbitrary graph $G = (V, E)$, the bridges can be identified in $O(|E|)$ time (Tarjan, 1974; Schmidt, 2013). Rather than applying such graph algorithms to identify the junctions in our leaf-free configurations however, we took advantage of the associated loop configurations. These loop configurations were also used to measure the observable H_{lf} , defined in Section 5.2.2.

Consider an edge e which is occupied in the leaf-free configuration, and denote the leaf-free cluster to which it belongs by \mathcal{C}_e . In the planar case, it is clear that e will be a bridge iff the two loop segments associated with it belong to the same loop. More generally, the same observation holds on the torus provided \mathcal{C}_e does not simultaneously wind in both the x and y directions.

If \mathcal{C}_e does simultaneously wind in both the x and y directions, loop arguments may still be used, however the situation is more involved. It clearly remains true that if the two loop segments associated with e belong to different loops, then e is a nonbridge.

Suppose instead that the two loop segments associated with e belong to the same loop, which we denote by \mathcal{L} . Deleting e breaks \mathcal{L} into two smaller loops, \mathcal{L}_1 and \mathcal{L}_2 . For each such loop, we let w_x and w_y denote the winding numbers in the x and y directions, respectively, and we define $w = |w_x| + |w_y|$. As we explain below, the following two statements hold:

- (i) If $w(\mathcal{L}_1) = 0$ or $w(\mathcal{L}_2) = 0$, then e is a bridge.
- (ii) If $w(\mathcal{L}) = 0$ and $w(\mathcal{L}_1) = 1$, then e is a nonbridge.

As an illustration, in Fig. 4.1 Edge 1 is a junction while Edge 2 is a nonbridge, despite both of them being bounded by the same loop. Edge 1 can be correctly

classified using statement (i), while Edge 2 can be correctly classified using statement (ii).

By making use of these observations, all but very few edges in the leaf-free clusters can be classified as bridges/nonbridges. We note that in our implementation of the above algorithm, the required w values can be immediately determined from the stored loop configuration without further computational effort. For the small number of edges to which neither of the above two statements apply, we simply delete the edge and perform a connectivity check using simultaneous breadth-first search. This takes $O(L^{d_F-x_2})$ time per edge tested (Deng *et al.*, 2010).

We now justify statement (i). In this case, the loop \mathfrak{L}_1 is contained in a simply-connected region on the surface of the torus. The cluster contained within the loop \mathfrak{L}_1 is therefore disconnected from the remainder of the lattice, implying that e is a bridge. Edge 1 in Fig. 4.1 provides an illustration.

Finally, we justify statement (ii). In this case, \mathfrak{L}_1 and \mathfrak{L}_2 either both wind in the x direction, or both in the y direction (one winds in the positive sense, the other in the negative sense). Suppose they wind in the y direction. It then follows from the definition of the BKW loops that there can be no x -windings in the cluster $\mathcal{C}_e \setminus e$. By assumption however, \mathcal{C}_e does contain an x -winding, so it must be the case that e belongs to a winding cycle in \mathcal{C}_e that winds in the x direction. The edge e is therefore not a bridge. Edge 2 in Fig. 4.1 provides an illustration.

4.2.3 Measured quantities

From our simulations, we estimated the following quantities.

1. The mean density of branches ρ_b , junctions ρ_j , and nonbridges ρ_n .
2. The mean size of the largest cluster C_1

3. The mean size of the largest leaf-free cluster C_{lf}
4. The mean size of the largest bridge-free cluster C_{bf}
5. The mean length of the largest loop, H_{lf} , for the loop configuration associated with leaf-free configurations
6. The mean length of the largest loop, H_{bf} , for the loop configuration associated with bridge-free configurations

We note that fewer samples were generated for C_1 and H_{bf} than for other the quantities.

4.3 Results

In Sections 4.3.2, 4.3.3, 4.3.4, we discuss least-squares fits for ρ_b , ρ_j , ρ_n and C_{lf} , C_{bf} , H_{lf} , H_{bf} . The results are presented in Tables 4.1, 4.2 and 4.3. In Section 4.3.1, we first make some comments on the ansätze and methodology used.

4.3.1 Fitting ansätze and methodology

Let ρ_1 (ρ_2) denote the mean density of occupied edges whose two associated loop segments belong to the same (distinct) loop(s). From Lemma 4.4.1 in Sec. 4.4, we know that for $p = 1/2$ bond percolation on \mathbb{Z}_L^2 we have $\rho_1 = \rho_2 = 1/4$ for all L . In the plane however, an edge is a bridge iff the two associated loop segments belong to the same loop. We therefore expect that both ρ_n and $\rho_j + \rho_b$ should converge to $1/4$ as $L \rightarrow \infty$.

Furthermore, there is a natural interpretation of the quantity $\rho_n - \rho_2$. As noted in Section 4.2.2, if the two loop segments associated with an edge belong to different loops, then that edge cannot be a bridge. This implies that $\rho_n - \rho_2$ is equal to the

probability of the event that “a given edge is not a bridge but has both its loop arcs in the same loop”. Let us denote this event by \mathcal{B} . Studying the finite-size behaviour of ρ_n will therefore allow us to study the scaling of $\mathbb{P}(\mathcal{B})$. Since $\rho_j + \rho_b + \rho_n = \rho_1 + \rho_2$, it follows that $\rho_1 - \rho_j - \rho_b$ is also equal to $\mathbb{P}(\mathcal{B})$.

Armed with the above observations, we fit our Monte Carlo data for the densities ρ_j , ρ_b and ρ_n to the finite-size scaling ansatz

$$\rho = \rho_0 + a_1 L^{-\nu_1} + a_2 L^{-\nu_2}. \quad (4.3.1)$$

We note that since $\rho_j + \rho_b + \rho_n = 1/2$ for all L , the finite-size corrections of $\rho_j + \rho_b$ should be equal in magnitude and opposite in sign to the finite-size corrections of ρ_n . Since $\rho_n = 1/4 + \mathbb{P}(\mathcal{B})$, the latter should be positive and the former negative.

Finally, we note that the event \mathcal{B} essentially characterizes edges which *would* be bridges in the plane, but which are prevented from being bridges on the torus by windings. By construction, branches always have at least one end attached to a tree, suggesting that they cannot be *trapped* in winding cycles in this way. This would suggest that it should be ρ_j that contributes the leading correction of $\rho_j + \rho_b$ away from its limiting value of $1/4$.

The observables C_{lf} , C_{bf} , H_{lf} , H_{bf} are expected to display non-trivial critical scaling, and we fit them to the finite-size scaling ansatz

$$\mathcal{O} = c_0 + L^{d_{\mathcal{O}}}(a_0 + a_1 L^{-\nu_1} + a_2 L^{-\nu_2}) \quad (4.3.2)$$

where $d_{\mathcal{O}}$ denotes the appropriate fractal dimension.

As a precaution against correction-to-scaling terms that we failed to include in the fit ansatz, we imposed a lower cutoff $L > L_{\min}$ on the data points admitted in the fit, and we systematically studied the effect on the χ^2 value of increasing L_{\min} .

Generally, the preferred fit for any given ansatz corresponds to the smallest L_{\min} for which the goodness of fit is reasonable and for which subsequent increases in L_{\min} do not cause the χ^2 value to drop by vastly more than one unit per degree of freedom. In practice, by “reasonable” we mean that $\chi^2/\text{DF} \lesssim 1$, where DF is the number of degrees of freedom.

In all the fits reported below we fixed $y_2 = 2$, which corresponds to the exact value of the sub-leading thermal exponent (Nienhuis, 1984).

4.3.2 Bond densities

Leaving y_1 free in the fits of ρ_j and ρ_n we estimate $y_1 = 1.2505(10)$. We therefore conjecture that $y_1 = 5/4$, which we note is precisely equal to the two-arm exponent $x_2 = 5/4$. We comment on this observation further in Section 4.5.

For ρ_b by contrast, we were unable to obtain stable fits with y_1 free. Fixing $y_1 = 5/4$, the resulting fits produce estimates of a_1 that are consistent with zero. In fact, we find ρ_b is consistent with 0.214 050 18 for all $L \geq 24$. This weak finite-size dependence of ρ_b is in good agreement with the arguments presented in Section 4.3.1.

All the fits for ρ_b , ρ_j and ρ_n gave estimates of a_2 consistent with zero. We therefore set $a_2 = 0$ identically in the fits reported in Table 4.1.

From the fits, we estimate $\rho_{b,0} = 0.214\,050\,18(5)$, $\rho_{j,0} = 0.035\,949\,79(8)$ and $\rho_{n,0} = 0.250\,000\,1(2)$. We note that $\rho_{b,0} + \rho_{j,0} = \rho_{n,0} = 1/4$ within error bars, as expected. The fit details are summarized in Table 4.1. We also note that the estimates of a_1 for ρ_j and ρ_n are equal in magnitude and opposite in sign, which is as expected given that a_1 is consistent with zero for ρ_b .

ρ	ρ_0	y_1	a_1	$L_{\min}/DF/\chi^2$
ρ_b	0.214 050 19(3)	5/4	0.000 04(4)	24/9/6
	0.214 050 19(3)	5/4	0.000 05(5)	32/8/6
	0.214 050 18(3)	5/4	0.000 09(6)	48/7/4
ρ_j	0.035 949 78(5)	1.250 2(2)	-0.277 7(2)	24/8/4
	0.035 949 78(5)	1.250 2(3)	-0.277 7(3)	32/7/4
	0.035 949 79(6)	1.250 0(4)	-0.277 5(4)	48/6/4
ρ_n	0.250 000 1(1)	1.250 7(5)	0.278 3(5)	24/8/2
	0.250 000 1(1)	1.250 8(6)	0.278 4(6)	32/7/2
	0.250 000 1(1)	1.250 6(7)	0.278 1(9)	48/6/2

Table 4.1: Fit results for ρ_b , ρ_j , and ρ_n .

In Fig. 4.3, we plot ρ_b , ρ_j and ρ_n versus $L^{-5/4}$. The plot clearly demonstrates that the leading finite-size corrections for ρ_j and ρ_n are governed by exponent $x_2 = 5/4$, while essentially no finite-size dependence can be observed for ρ_b .

4.3.3 Fractal dimensions of clusters

The first question to be addressed in this section is to determine if the fractal dimension of leaf-free clusters differs from d_F . We therefore fit the data for C_{lf} to the ansatz (4.3.2). The fit results are reported in Table 4.2. In the reported fits we set $c_0 = 0$ identically, since leaving it free produced estimates for it consistent with zero. Leaving y_1 free, we estimate $y_1 = 1.3(3)$, which is consistent with the value $y_1 = 5/4$ observed for ρ_j and ρ_n .

From the fits, we estimate $d_{C_{lf}} = 1.895 84(6)$, which is consistent with the fractal dimension of percolation clusters, $d_F = 91/48$. This indicates that although around 43% of all occupied bonds are branches (see Table 4.1), their deletion from percolation configurations does not alter the fractal dimension of the resulting clusters. In Fig. 4.4, we plot $L^{-91/48}C_{lf}$ versus $L^{-5/4}$.

For comparison, we also performed fits of C_1 to the ansatz (4.3.2), obtaining the estimate $a_0 = 0.983 8(5)$, which is strictly larger than the value estimated for C_{lf} .

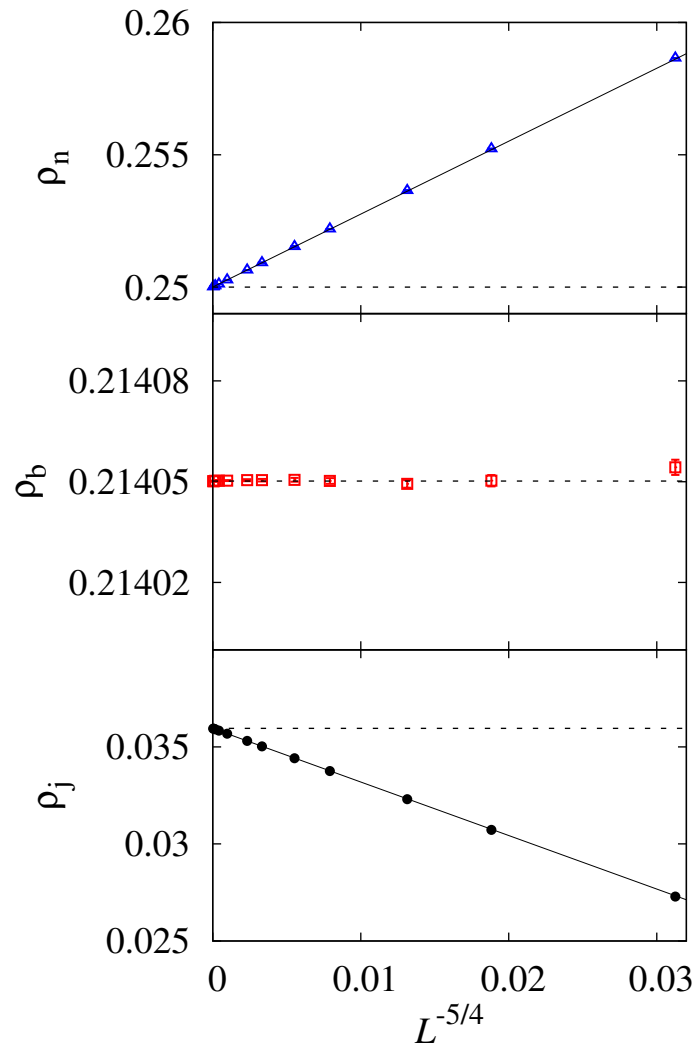


Figure 4.3: Plots of ρ_n (top), ρ_b (middle), and ρ_j (bottom) versus $L^{-5/4}$. From top to bottom, the three dashed lines respectively correspond to values $1/4$, 0.21405018 , and 0.03594979 . The statistical error of each data point is smaller than the symbol size. The straight lines are simply to guide the eye.

As $L \rightarrow \infty$ therefore, a non-trivial fraction $1 - a_0(C_{lf})/a_0(C_1) \approx 40\%$ of sites in the largest percolation cluster are deleted by burning the branches. This is close to, but slightly smaller than, the proportion of occupied bonds which are branches $2\rho_b \approx 43\%$.

We next study the fractal dimension of bridge-free clusters. We fit the Monte Carlo data for C_{bf} to the ansatz (4.3.2), and the results are reported in Table 4.2. In the fits, we fixed $\gamma_1 = 5/4$, and again observed that c_0 is consistent with zero. We also performed fits (not shown) with γ_1 free, or fixed to $\gamma_1 = 1$, in order to estimate

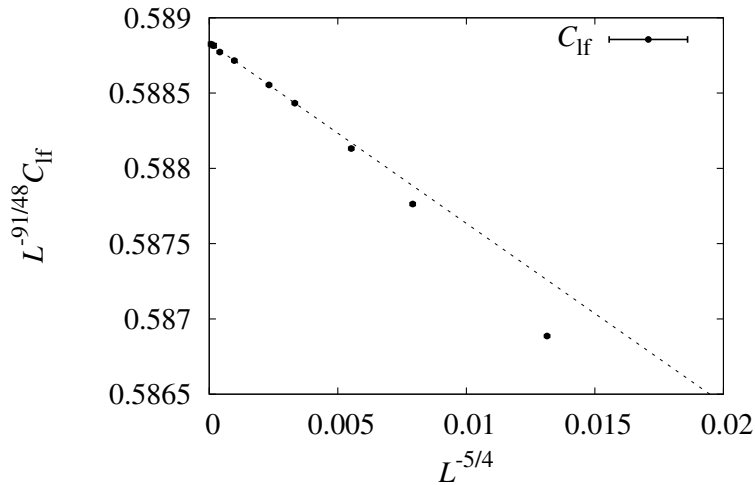


Figure 4.4: Plot of $L^{-91/48} C_{lf}$ versus $L^{-5/4}$. The statistical error of each data point is smaller than the symbol size. The straight lines are simply to guide the eye.

the systematic error in our estimates of d_B . This produced our final estimate $d_B = 1.64336(10)$. This value is consistent with the estimate $d_B = 1.6434(2)$ (Deng et al., 2004), but with an improved error bar.

Fig. 4.5 plots $L^{-d_B} C_{bf}$ versus $L^{-5/4}$, with d_B chosen to be the central value of our estimate, as well as the central value plus or minus three error bars. The obvious upward (downward) bending as L increases when using a d_B value above (below) our central estimate illustrates the reliability of our final estimate of d_B .

\mathcal{O}	$d_{\mathcal{O}}$	a_0	a_1	a_2	$L_{\min}/DF/\chi^2$
C_{lf}	1.89582(2)	0.58888(2)	-0.103(6)	-0.61(5)	24/7/8
	1.89584(2)	0.58881(6)	-0.091(9)	-0.75(9)	32/6/4
	1.89584(2)	0.58878(8)	-0.08(2)	-0.8(3)	48/5/4
C_{bf}	1.64332(3)	0.8092(2)	0.07(2)	-0.2(2)	24/7/4
	1.64332(3)	0.8091(2)	0.08(3)	-0.3(3)	32/6/4
	1.64336(4)	0.8089(3)	0.14(5)	-1.2(7)	48/5/1

Table 4.2: Fit results for C_{lf} and C_{bf} .

4.3.4 Fractal dimensions of loops

Finally, we studied the fractal dimensions of the loop configurations associated with both leaf-free and bridge-free configurations.

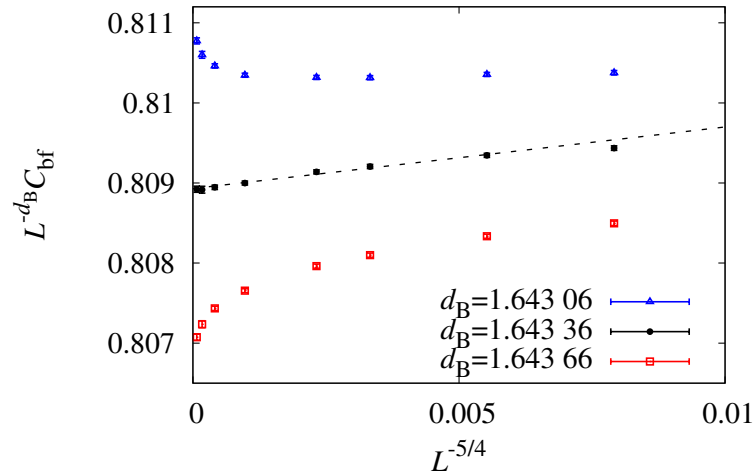


Figure 4.5: Plot of $L^{-d_B} C_{bf}$ versus $L^{-5/4}$, with $d_B = 1.643\ 06$, $1.643\ 36$ and $1.643\ 66$. The statistical error of each data point is smaller than the symbol size. The straight lines are simply to guide the eye.

We fit the data for H_{lf} and H_{bf} to the ansatz (4.3.2), with $\gamma_1 = 5/4$ fixed. For both H_{lf} and H_{bf} , the fits gave estimates of c_0 consistent with zero. We therefore fixed $c_0 = 0$ identically in the fits reported in Table 4.3. To estimate the systematic error, we compared these results with fits in which γ_1 was free, and also fits with $\gamma_1 = 1$ fixed. Our resulting final estimates are $d_{H_{lf}} = 1.749\ 96(8)$ and $d_{H_{bf}} = 1.333\ 3(3)$.

For leaf-free configurations, therefore, our fits strongly suggest $d_{H_{lf}} = 7/4 = d_H$. Thus, deleting branches from percolation configurations affects neither the fractal dimension for cluster size, nor the fractal dimension for lengths of the associated loops. For bridge-free configurations by contrast, the fits suggest that $d_{H_{bf}} = 4/3 = d_E$.

In Fig. 4.6, we plot H_{lf} and H_{bf} versus L to illustrate our estimates for $d_{H_{lf}}$ and $d_{H_{bf}}$.

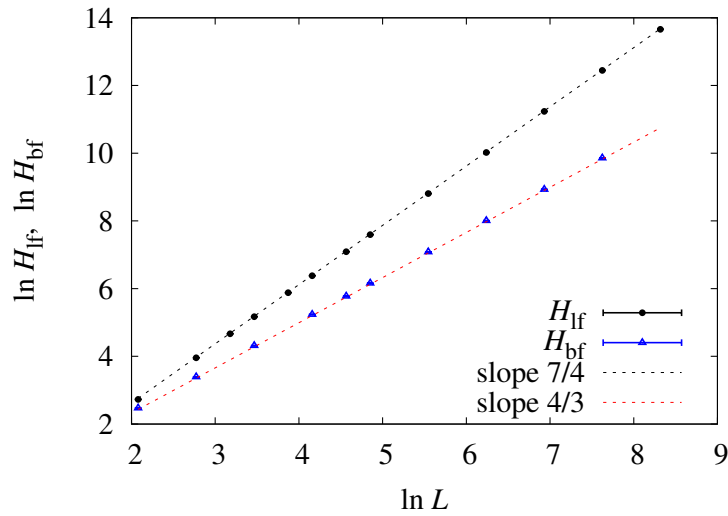


Figure 4.6: Log-log plot of H_{lf} and H_{bf} versus L . The two dashed lines have slopes $7/4$ and $4/3$ respectively. The statistical error of each data point is smaller than the symbol size.

\mathcal{O}	$d_{\mathcal{O}}$	a_0	a_1	a_2	$L_{\min}/DF/\chi^2$
H_{lf}	1.75005(2)	0.40811(6)	0.039(6)	-0.25(5)	24/7/12
	1.75002(3)	0.40817(7)	0.029(9)	-0.15(9)	32/6/10
	1.74999(4)	0.40830(9)	0.00(2)	0.3(3)	48/5/5
H_{bf}	1.33333(8)	0.7340(4)	0.28(3)	-1.1(2)	16/5/4
	1.3332(2)	0.7345(6)	0.20(8)	-0.3(8)	32/4/3
	1.3333(2)	0.7342(9)	0.3(2)	-2(3)	64/3/2

Table 4.3: Fit results for H_{lf} and H_{bf} .

4.4 A loop duality lemma

Let \mathcal{L}_1 (\mathcal{L}_2) denote the fraction of occupied edges whose two associated loop segments belong to the same (distinct) loop(s).

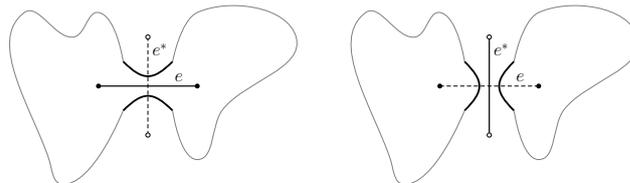


Figure 4.7: Left: Illustration of a configuration $A \subseteq E$ for which the event $\ell_1(e)$ occurs. Right: The corresponding configuration $A^* \cup e^*$ for which the event $\ell_2(e^*)$ occurs.

Lemma 4.4.1. *Consider $p = 1/2$ bond percolation on \mathbb{Z}_L^2 . For any L we have $\mathbb{E} \mathcal{L}_1 = \mathbb{E} \mathcal{L}_2 = 1/4$.*

Proof. Let $m = 2L^2$ denote the number of edges in $G = \mathbb{Z}_L^2$. Since G is a cellularly-embedded graph (Ellis-Monaghan and Moffatt, 2013), it has a well-defined geometric dual G^* and medial graph $\mathcal{M}(G) = \mathcal{M}(G^*)$. For any $e \in E$ we denote its dual by $e^* \in E^*$.

For $e \in E$, let $\ell_1(e)$ be the event that the two loop segments associated with e both belong to the same loop, and let $\ell_2(e)$ be the event that they belong to distinct loops. The key observation is that for any $0 \leq a \leq m$ we have

$$\sum_{\substack{A \subseteq E \\ |A|=a}} \sum_{e \in A} \mathbf{1}_{\ell_1(e)}(A) = \sum_{\substack{B^* \subseteq E^* \\ |B^*|=m+1-a}} \sum_{e^* \in B^*} \mathbf{1}_{\ell_2(e^*)}(B^*) \quad (4.4.1)$$

To see this, first note that the number of terms on either side of (4.4.1) is $\binom{m}{a} a = \binom{m}{m+1-a} (m+1-a)$, and that each term is either 0 or 1. Then note that there is a bijection between the terms on the left- and right-hand sides such that the term on the LHS is 1 iff the term on the RHS is 1, as we now describe. Let $A \subseteq E$ with $|A| = a$, and let A^* denote the *dual* configuration: include e^* in A^* iff $e \notin A$. With the term on the LHS corresponding to (A, e) , associate the term $(B^*, e^*) = (A^* \cup e^*, e^*)$ appearing on the RHS. This is clearly a 1-1 correspondence.

Let $\mathfrak{L}(A)$ denote the loop configuration corresponding to A . By construction, $\mathfrak{L}(A) = \mathfrak{L}(A^*)$. The loop configuration $\mathfrak{L}(A^* \cup e^*)$ differs from $\mathfrak{L}(A)$ only in that the loop arcs cross e^* in $\mathfrak{L}(A)$ but cross e in $\mathfrak{L}(A^* \cup e^*)$. If $\mathbf{1}_{\ell_1(e)}(A) = 1$, then it follows that $\mathbf{1}_{\ell_2(e^*)}(B^*) = 1$. The converse holds by duality, and so (4.4.1) is established. See Fig. 4.7 for an illustration.

Summing both sides of (4.4.1) over a and dividing by $m 2^m$ then shows that $\mathbb{E} \mathcal{L}_1 = \mathbb{E} \mathcal{L}_2$. Since on average precisely $1/2$ of all edges are occupied when $p = 1/2$, the stated result follows. \square

4.5 Discussion

We have studied the geometric structure of percolation on the torus, by considering a partition of the edges into three natural classes. On the square lattice, we have found that leaf-free configurations have the same fractal dimension and hull dimension as standard percolation configurations, while bridge-free configurations have cluster and hull fractal dimensions consistent with the backbone and external perimeter dimensions, respectively.

In addition to the results discussed above, we have extended our study of leaf-free configurations to site percolation on the triangular lattice and bond percolation on the simple-cubic lattice, the critical points of which are respectively $1/2$ and $0.248\,811\,82(10)$ (Wang *et al.*, 2013b). We find numerically that the fractal dimensions of leaf-free clusters for these two models are respectively $1.895\,7(2)$ and $2.522\,7(6)$, both of which are again consistent with the known results $91/48$ and $2.522\,95(15)$ (Wang *et al.*, 2013b) for d_F . In both cases, our data show that the density of branches is again only very weakly dependent on the system size.

It would also be of interest to study the bridge-free configurations on these lattices. In addition to investigating the fractal dimensions for cluster size, and in the triangular case also the hull length, it would be of interest to determine whether the leading finite-size correction to ρ_n is again governed by the two-arm exponent.

The two-arm exponent is usually defined by considering the probability of having multiple spanning clusters joining inner and outer annuli in the plane. As noted in

Section 4.3.1 however, our results show that for percolation, the two-arm exponent also governs the probability of a rather natural geometric event on the torus: the event that a given edge is not a bridge but has both its loop arcs in the same loop. This provides an interesting alternative interpretation of the two-arm exponent in terms of toroidal geometry.

Let us refer to an edge that is not a bridge but has both its loop arcs in the same loop as a *pseudobridge*. We note that an alternative interpretation of the observation that $(\rho_n - \rho_2) \sim L^{-x_2}$ is that the number of pseudobridges $L^2(\rho_n - \rho_2)$ scales as L^{d_R} .

A natural question to ask is to what extent the above results carry over to the general setting of the Fortuin-Kasteleyn random-cluster model. Consider the case of two dimensions once more. In that case, we know that if we fix the edge weight to its critical value and take $q \rightarrow 0$ we obtain the uniform spanning trees (UST) model. For this model all edges are branches, and so the leaf-free configurations, which are therefore empty, certainly do not scale in the same way as UST configurations. Despite this observation, preliminary simulations⁴ performed on the toroidal square lattice at $q = 0.09, 0.16, 1.5, 2.0, 2.5, 3.0$ and 3.5 suggest that, for all $q \in (0, 4]$, the leaf-free configurations have the same fractal dimension and hull dimension as the corresponding standard random cluster configurations. In the context of the random cluster model, the behaviour of the leaf-free configurations for the UST model therefore presumably arises via amplitudes which vanish at $q = 0$.

In addition, these preliminary simulations suggest that the number of pseudobridges in fact scales as L^{d_R} for the critical random cluster model at any $q \in (0, 4]$. It would also be of interest to determine whether the fractal dimensions of cluster size and hull length for bridge-free random cluster configurations again coincide with d_B and d_E when $q \neq 1$.

⁴These simulations were performed using the Sweeny algorithm (Sweeny, 1983) for $q < 1$ and the Chayes-Machta algorithm (Chayes and Machta, 1998) for $q > 1$.

4.6 Acknowledgments

The authors wish to thank Bob Ziff for several useful comments/suggestions, and T.G. wishes to thank Nick Wormald for fruitful discussions relating to the density of bridges. This work is supported by the National Nature Science Foundation of China under Grant No. 91024026 and 11275185, and the Chinese Academy of Sciences. It was also supported under the Australian Research Council's Discovery Projects funding scheme (project number DP110101141), and T.G. is the recipient of an Australian Research Council Future Fellowship (project number FT100100494). The simulations were carried out in part on NYU's ITS cluster, which is partly supported by NSF Grant No. PHY-0424082. In addition, this research was undertaken with the assistance of resources provided at the NCI National Facility through the National Computational Merit Allocation Scheme supported by the Australian Government. J.F.W and Y.J.D acknowledge the Specialized Research Fund for the Doctoral Program of Higher Education under Grant No. 20103402110053. Y.J.D also acknowledge the Fundamental Research Funds for the Central Universities under Grant No. 2340000034.

Declaration for Thesis Chapter 5

Declaration by candidate

In the case of Chapter 5, the nature and extent of my contribution to the work was the following:

Nature of contribution	Extent of contribution (%)
Run simulations, analyse the data, and write the article	70%

The following co-authors contributed to the work. If co-authors are students at Monash University, the extent of their contribution in percentage terms must be stated:

Name	Nature of contribution	Extent of contribution (%) for student co-authors only
Xiao Xu	Programming and data analysis	
Timothy Garoni	Provide guidance and proofreading	
Youjin Deng	Provide guidance and proofreading	

The undersigned hereby certify that the above declaration correctly reflects the nature and extent of the candidate's and co-authors' contributions to this work*.

Candidate's Signature		Date 27/01/2016
-----------------------	---	-----------------

Main Supervisor's Signature		Date 27/01/2016
-----------------------------	---	-----------------

*Note: Where the responsible author is not the candidate's main supervisor, the main supervisor should consult with the responsible author to agree on the respective contributions of the authors.

Chapter 5

Leaf-excluded percolation in two and three dimensions

Chapter 5 is based on the article Zhou Z, Xu X, Garoni TM, Deng Y. 2015. Leaf-excluded percolation in two and three dimensions. Physical Review E 91: 022 140.

Abstract. *We introduce the leaf-excluded percolation model, which corresponds to independent bond percolation conditioned on the absence of leaves (vertices of degree one). We study the leaf-excluded model on the square and simple-cubic lattices via Monte Carlo simulation, using a worm-like algorithm. By studying wrapping probabilities, we precisely estimate the critical thresholds to be 0.355 247 5(8) (square) and 0.185 022(3) (simple-cubic). Our estimates for the thermal and magnetic exponents are consistent with those for percolation, implying that the phase transition of the leaf-excluded model belongs to the standard percolation universality class.*

References are considered at the end of the thesis.

Chapter 5

Leaf-excluded percolation in two and three dimensions

5.1 Introduction

Graphical models, i.e. statistical-mechanical models in which the configuration space consists of certain bond configurations drawn on a lattice, play a fundamental role in the theory of critical phenomena. Examples include percolation, and more generally the Fortuin-Kasteleyn random-cluster model, as well as dimers and various loop models. In the latter two cases, the models are in fact examples of “forbidden-degree” models, in which only bond configurations which preclude specified vertex degrees are allowed; for dimers, all degrees higher than 1 are forbidden, while loop models forbid all odd degrees.

In this article, we introduce and study another example of a forbidden-degree model, the *leaf-excluded* model, which forbids bond configurations containing vertices of degree 1 (i.e. *leaves*). Consider a finite connected graph $G = (V, E)$, and

let

$$\Omega = \{A \subseteq E : d_A(i) \neq 1\}, \quad (5.1.1)$$

where $d_A(i)$ denotes the degree of vertex i in the spanning subgraph (V, A) . As an example, Fig. 5.1 illustrates a typical element of Ω in the case where G is a 6×6 patch of the square lattice. In this case, Ω is the set of all ways of drawing bond configurations such that each site has degree 0, 2, 3 or 4.

The leaf-excluded model on G chooses random configurations $A \in \Omega$ according to the distribution

$$\mathbb{P}(A) \propto v^{|A|}, \quad (5.1.2)$$

where $v > 0$ is a (temperature-like) bond fugacity, and $|A|$ denotes the number of bonds in the configuration A .

The model defined by (5.1.1) and (5.1.2) is equivalent to considering standard independent bond percolation and conditioning on the absence of leaves. This conditioning then introduces non-trivial correlations between the edges. Note that, on the square lattice, if we additionally forbid degree 3 vertices, the resulting model coincides with the high temperature (and low temperature) expansion of the Ising model. On the square lattice therefore, the definition of the leaf-excluded model lies precisely half way between the definitions of standard percolation (no vertex degrees forbidden) and the Ising loop representation (both leaves and degree 3 vertices forbidden). It is therefore natural to ask to which universality class does the leaf-excluded model belong?

One of the main goals of percolation theory in recent decades has been to understand the geometric structure of percolation clusters, following the pioneering work of Stanley (Stanley, 1977). Recently, the present authors (Xu *et al.*, 2014b) studied the geometric structure of percolation clusters by classifying the bridges present in clusters into two types: branches and junctions. A bridge was defined to

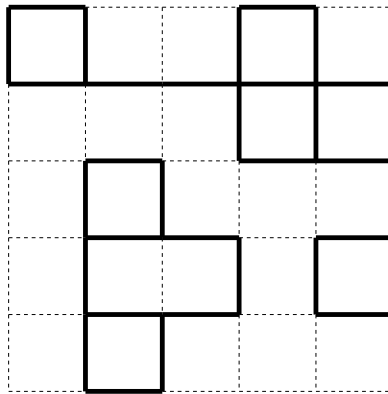


Figure 5.1: A typical configuration (denoted by bold edges) of the leaf-excluded model on a 6×6 patch of the square lattice.

be a branch if and only if at least one of the two clusters produced by its deletion is a tree. It was found that the leaf-free clusters, obtained by deleting the branches from percolation clusters, have the same fractal dimension and hull dimension as the original percolation clusters.

The set of all such leaf-free configurations coincides with Ω as defined in (5.1.1). We emphasize, however, that in (Xu *et al.*, 2014b) these configurations were generated by applying a *burning algorithm* (Herrmann *et al.*, 1984) to standard bond percolation configurations, whereas in the current work they are sampled directly from the distribution (5.1.2). The probability distribution on these configurations studied in (Xu *et al.*, 2014b) is therefore very different to the distribution that we consider here. Nevertheless, based on the observations from (Xu *et al.*, 2014b), one might expect that the leaf-excluded model should belong to the percolation universality class. In this article, we present a careful numerical study which confirms this picture.

Due to the non-trivial combinatorial constraint inherent in the definition of Ω , to efficiently generate random samples from the leaf-excluded model requires a suitable Markov-chain Monte Carlo algorithm. We introduce a worm-like algorithm for this purpose. Using this algorithm, we simulate the leaf-excluded model on the square and simple-cubic lattices with periodic boundary conditions. We

estimate the critical threshold v_c by studying the finite-size scaling of wrapping probabilities. Wrapping probabilities are believed to be universal, and have been successfully applied to the estimation of critical thresholds of several models (Wang *et al.*, 2013b; Newman and Ziff, 2000; Xu *et al.*, 2014a). By simulating precisely at our estimated v_c , we then estimate the thermal exponent $y_t = 1/\nu$ and magnetic exponent $y_h = d - \beta/\nu$. Here the exponent β describes the critical scaling of the percolation probability $P_\infty \sim (v - v_c)^\beta$, while ν describes that of the correlation length $\xi \sim |v - v_c|^{-\nu}$. Our results for critical exponents and universal amplitudes strongly suggest that the phase transition of the leaf-excluded model belongs to the standard percolation universality class.

The remainder of this paper is organized as follows. Sec. 5.2 introduces the worm-like algorithm and the observables measured in our simulations. Numerical results are summarized and analyzed in Section 5.3. A brief discussion is then given in Section 5.4.

5.2 Algorithm and Observables

5.2.1 Monte Carlo algorithm

In this section we describe a Markov-chain Monte Carlo algorithm for simulating the leaf-excluded model, which is similar in spirit to a worm algorithm (Prokof'ev and Svistunov, 2001). Worm algorithms provide very effective tools for simulating models on configuration spaces which are subject to non-trivial combinatorial constraints. The key idea underlying worm algorithms is to first enlarge the configuration space by including “defects”, and to then move these defects via a random walk. Numerical studies have shown that worm algorithms typically

provide highly efficient Monte Carlo methods (Deng *et al.*, 2007; Wolff, 2009b,a, 2010a,b).

To simulate the leaf-excluded model, we therefore consider an enlarged configuration space in which up to two leaves are permitted. For clarity, it is convenient to define the algorithm on an arbitrary (finite and connected) graph $G = (V, E)$. The space of worm configurations is then

$$\mathcal{S} = \{(A, u, v) \in E \times V^2 : d_A(i) \neq 1 \text{ for } i \neq u, v\}.$$

The algorithm proceeds as follows. Let Δ denote symmetric difference of sets. At each time step, we perform precisely one of the following three possible updates, chosen at random with respective probabilities p_1, p_2, p_3 :

1. Set $(A, u, v) \mapsto (A, v, u)$
2. Choose uniformly random $w \in V$ and set $(A, u, v) \mapsto (A, w, v)$ if $d_A(u) \neq 1$ and $d_A(w) \neq 1$.
3. Do the following:
 - (a) Choose uniformly random $w \sim u$
 - (b) Propose $(A, u, v) \mapsto (A \Delta uw, w, v)$, and accept with probability $\min[1, v^{|A \Delta uw| - |A|}]$, provided $(A \Delta uw, w, v) \in \mathcal{S}$.

After each update, if the new state is leaf-excluded, we measure observables. In our simulations, we used $p_1 = p_2 = 1/4$ and $p_3 = 1/2$.

We note that, unlike the case of the worm algorithm for the Ising model (Prokof'ev and Svistunov, 2001), there is no particular reason for using two defects in our algorithm, and in fact the above algorithm can be easily modified to use any fixed number of defects; including one defect. We also note that it would be somewhat

of a misnomer to refer to the above algorithm as a *worm* algorithm; for a state $(A, u, v) \in \mathcal{S}$, it will not be true in general that u and v are connected by occupied bonds, and so in general there is no *worm* as such. This is in contrast to worm algorithms for Eulerian subgraphs (e.g. Ising high temperature graphs), where the handshaking lemma demands that the two defects be connected.

5.2.2 Sampled quantities

We simulated the leaf-excluded model on the $L \times L$ square lattice for system sizes up to $L = 1024$, and on the $L \times L \times L$ simple-cubic lattice for system sizes up to $L = 96$. For each system size, approximately 10^8 samples were produced.

For each sampled leaf-excluded bond configuration, we measured the following observables.

1. The number of occupied bonds \mathcal{N}_b .
2. The size of the largest cluster \mathcal{C}_1 .
3. The cluster-size moments $\mathcal{S}_m = \sum_{\mathcal{C}} |\mathcal{C}|^m$ with $m = 2, 4$, where the sum is over all clusters \mathcal{C} .
4. The indicators $\mathcal{R}^{(x)}, \mathcal{R}^{(y)}, \mathcal{R}^{(z)}$ for the event that a cluster wraps around the lattice in the x, y , or z direction, respectively.

From these observables, we calculated the following quantities:

1. The mean size of the largest cluster $C_1 = \langle \mathcal{C}_1 \rangle$, which scales as $\sim L^{y_h}$ at the critical point v_c .
2. The mean size of the cluster at the origin, $\chi = \langle \mathcal{S}_2 \rangle / L^d$, which at v_c scales as $\sim L^{2y_h - d}$.

3. The dimensionless ratios

$$Q_1 = \frac{\langle \mathcal{C}_1^2 \rangle}{\langle \mathcal{C}_1 \rangle^2}, \quad Q_2 = \frac{\langle 3\mathcal{S}_2^2 - 2\mathcal{S}_4 \rangle}{\langle \mathcal{S}_2^2 \rangle}. \quad (5.2.1)$$

4. The probability that a winding exists in the x direction $R^{(x)} = \langle \mathcal{R}^{(x)} \rangle$. In two dimensions, we also measured $R^{(2)} = \langle \mathcal{R}^{(x)} \mathcal{R}^{(y)} \rangle$, and in three dimensions measured $R^{(3)} = \langle \mathcal{R}^{(x)} \mathcal{R}^{(y)} \mathcal{R}^{(z)} \rangle$. $R^{(d)}$ gives the probability that windings simultaneously exist in all d possible directions.

5. The covariance of $\mathcal{R}^{(x)}$ and \mathcal{N}_b

$$g_{bR}^{(x)} = \langle \mathcal{R}^{(x)} \mathcal{N}_b \rangle - \langle \mathcal{R}^{(x)} \rangle \langle \mathcal{N}_b \rangle, \quad (5.2.2)$$

which is expected to scale as $\sim L^{y_t}$ at the critical point.

5.3 Results

5.3.1 Fitting methodology

We began by estimating the critical point v_c by performing a finite-size scaling analysis of the ratios Q_1 , Q_2 and wrapping probabilities $R^{(x)}$, $R^{(d)}$. The MC data for these quantities were fitted to the ansatz

$$\mathcal{O}(\epsilon, L) = \mathcal{O}_c + \sum_{k=1}^2 q_k \epsilon^k L^{ky_t} + b_1 L^{y_i} + b_2 L^{y_2}, \quad (5.3.1)$$

where $\epsilon = v_c - v$, y_i and y_2 are respectively the leading and sub-leading correction exponents, and $\mathcal{O}_c = \mathcal{O}(\epsilon = 0, L \rightarrow +\infty)$ is a universal constant. The parameters q_k, b_1, b_2 are non-universal amplitudes.

We then performed extensive simulations at our best estimate of v_c , in order to estimate the critical exponents y_t and y_h . These exponents were obtained by fitting $g_{bR}^{(x)}$, C_1 and χ to the ansatz

$$O(L) = L^{y_O} (a_0 + b_1 L^{y_i} + b_2 L^{y_2}), \quad (5.3.2)$$

where y_O equals y_t for $g_{bR}^{(x)}$, y_h for C_1 and $2y_h - d$ for χ , and a_0 is a non-universal constant. In all fits reported below, we fixed $y_2 = -2$, which corresponds to the exact value of the sub-leading correction exponent (Nienhuis, 1984) for percolation.

As a precaution against correction-to-scaling terms that we failed to include in the fit ansatz, we imposed a lower cutoff $L \geq L_{\min}$ on the data points admitted in the fit, and we systematically studied the effect on the χ^2 value of increasing L_{\min} . Generally, the preferred fit for any given ansatz corresponds to the smallest L_{\min} for which the goodness of fit is reasonable and for which subsequent increases in L_{\min} do not cause the χ^2 value to drop by vastly more than one unit per degree of freedom. In practice, by “reasonable” we mean that $\chi^2/\text{DF} \lesssim 1$, where DF is the number of degrees of freedom.

We analyze the data on the square lattice in Sec. 5.3.2 and Sec. 5.3.3. The results on the simple cubic lattice are shown in Sec. 5.3.4.

5.3.2 Square lattice near v_c

We first study the critical behavior of $R^{(x)}$, $R^{(d)}$ and Q_1 , Q_2 near v_c . Fig. 5.2 plots $R^{(x)}$ and Q_1 versus v . Clearly, $R^{(x)}$ suffers from only very weak corrections to scaling.

We begin by considering $R^{(x)}$. Setting $b_2 = 0$ and leaving y_i free, we were unable to obtain a stable estimate of y_i . The fits with two correction terms included

(fixing $y_i = -1$) show that b_1 is consistent with zero and $b_2 = 2(1)$ for $L_{\min} = 64$. In fact, the data for $R^{(x)}$ with $L_{\min} = 128$ can be well fitted even with fixed $b_1 = b_2 = 0$. We also perform fits with only one of $b_1 L^{-1}$ or $b_2 L^{-2}$ included. Comparing the various fit results, we estimate $v_c = 0.3552475(5)$ and $y_t = 0.752(3)$. The latter is clearly consistent with $3/4$ for two-dimensional percolation. We also estimate the universal amplitude $R_c^{(x)} = 0.5212(2)$, consistent with the exact value 0.521058290 (Pinson, 1994; Ziff *et al.*, 1999).

The fits of $R^{(d)}$ show that it suffers even weaker finite-size corrections. The amplitudes b_1 and b_2 are both consistent with zero for $L_{\min} = 16$. Again, we also perform fits in which we include only one of these corrections, and also fits in which we include neither. We then estimate $v_c = 0.3552474(5)$, $y_t = 0.754(3)$ and $R_c^{(d)} = 0.3517(1)$, the latter of which is consistent with the exact value 0.351642855 for standard percolation (Pinson, 1994; Ziff *et al.*, 1999).

Finally, we fit the data for Q_1 and Q_2 . The fits predict a leading correction exponent $y_i = -1.57(5)$ and $-1.7(1)$ respectively. We note that this is consistent with the exact value $-3/2$ (Ziff, 2011) for two-dimensional percolation. We estimate $v_c = 0.3552475(5)$ from Q_1 and $v_c = 0.3552475(8)$ from Q_2 . Both of their fits produce $y_t = 0.751(3)$. We also estimate the universal amplitudes $Q_{1,c} = 1.04147(5)$ and $Q_{2,c} = 1.1486(2)$, both of which are consistent with the estimates for standard percolation (Hu *et al.*, 2012).

Our estimates for v_c , y_t and the universal wrapping probabilities are summarized in Tab. 5.1, where we also report the known results for standard percolation. The results strongly suggest that the phase transition of the leaf-excluded model belongs to the standard percolation universality class.

In Fig. 5.3, we illustrate the accuracy of our estimate of v_c by plotting $R^{(x)}$ versus L with v set to our central estimate of v_c , $v = 0.3552475$, and also with v chosen

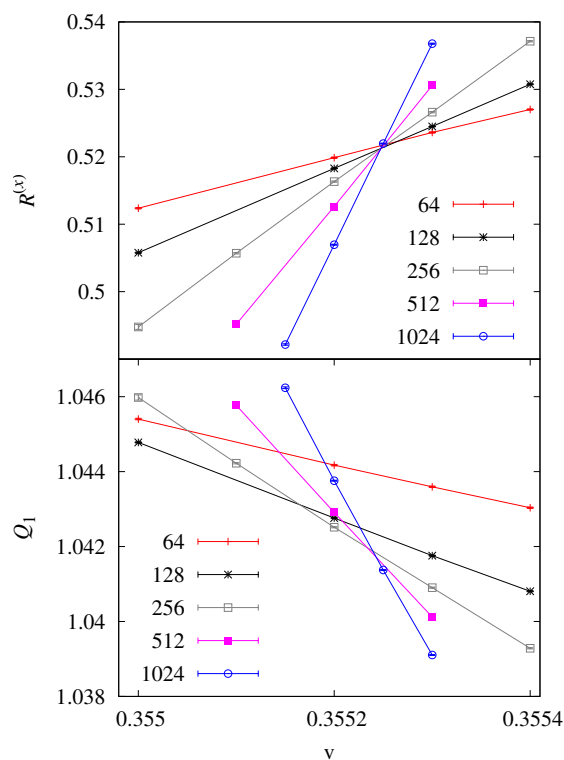


Figure 5.2: Plots of $R^{(x)}$ and Q_1 versus v for the leaf-excluded model on the square lattice.

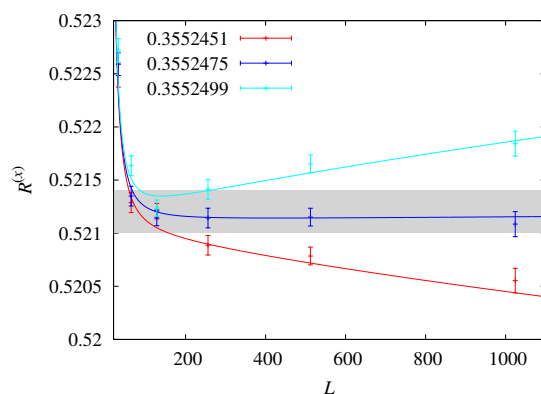


Figure 5.3: Plots of $R^{(x)}(v, L)$ versus L for fixed values of v , for the two-dimensional leaf-excluded model. The curves correspond to our preferred fit of the Monte Carlo data. The shaded grey strips indicate an interval of one error bar above and below the estimate $R_c^{(x)} = 0.5212(2)$.

three error bars above and below this estimate. Precisely at $v = v_c$, as $L \rightarrow \infty$ the data should tend to a horizontal line, whereas the data with $v \neq v_c$ should bend upward or downward. Fig. 5.3 provides confirmation that the true value of v_c does indeed lie in the interval $(0.3552451, 0.3552499)$. Moreover, the asymptotic flatness of the $R^{(x)}$ curve at our reported central estimate of v_c strongly suggests that our estimate lies very close indeed to the true value of v_c .

5.3.3 Square lattice at v_c

To obtain final estimates of y_t and y_h , we performed high-precision simulations at a single value of v corresponding to our estimated threshold $v_c = 0.3552475$, and fitted the data for $g_{bR}^{(x)}$, C_1 and χ to (5.3.2). The leading correction exponent was set to $y_i = -3/2$.

The fits of $g_{bR}^{(x)}$ show that both the amplitudes b_1 and b_2 are consistent with zero. The data for $g_{bR}^{(x)}$ can be well fitted ($\chi^2/DF < 1$ for $L_{\min} = 24$) even without any corrections. From the fits, we estimate $y_t = 0.750(1)$, which is consistent with the estimate in Sec. 5.3.2 but with improved precision.

The fits of C_1 and χ show a non-zero b_1 if only the leading correction term is included in the fits. For comparison, we also performed fits including only the $b_2 L^{-2}$ term, and including both corrections. Both of these fits suggest $y_h = 1.8958(1)$, which is fully consistent with the exact result $y_h = 91/48$ for two-dimensional percolation. As further illustration, Fig. 5.4 shows a plot of $L^{-3/4} g_{bR}^{(x)}$ and $L^{-91/48} C_1$ versus $L^{-3/2}$.

5.3.4 Simple-cubic lattice

We performed an analogous study of the leaf-excluded model on the simple-cubic lattice.

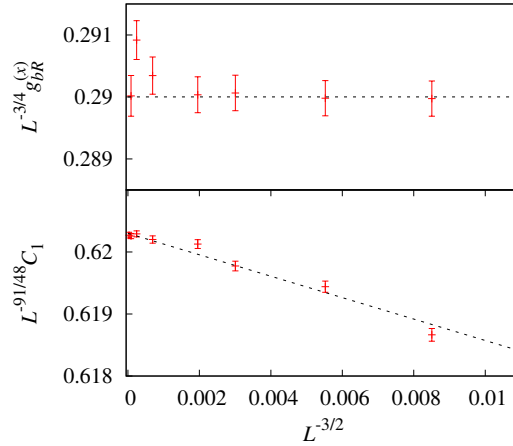


Figure 5.4: Plots of $L^{-3/4} g_{bR}^{(c)}$ and $L^{-91/48} C_1$ versus $L^{-3/2}$. The straight lines are simply to guide the eye.

We again began by fitting the data for $R^{(x)}$, $R^{(d)}$ and Q_1 , Q_2 to the ansatz (5.3.1) in order to estimate v_c . Fig. 5.5 plots $R^{(x)}$ and Q_1 versus v , which again clearly shows that $R^{(x)}$ suffers from only very weak corrections to scaling. In each case of fits, leaving y_i free resulted in unstable fits. Instead, we fixed $y_i = -1.2$, which is numerically estimated in (Wang *et al.*, 2013b) to be the leading correction exponent for three-dimensional percolation. For comparison, we performed fits with different combinations of the terms $b_1 L^{-1.2}$ or $b_2 L^{-2}$ present. The best estimates were obtained from $R^{(x)}$, which yield $v_c = 0.185022(3)$ and $y_t = 1.143(8)$. We also estimated the universal amplitudes $R_c^{(x)} = 0.260(4)$ and $R_c^{(d)} = 0.083(4)$. The universal amplitudes for Q_1 and Q_2 cannot be precisely estimated due to the strong finite-size corrections.

Simulating at our estimated v_c , we then fitted the data for $g_{bR}^{(x)}$, C_1 , χ to the ansatz (5.3.2) to estimate y_t and y_h . Both correction terms were included in the fits. The fits of $g_{bR}^{(x)}$ yields $y_t = 1.142(7)$. From C_1 we estimate $y_h = 2.513(5)$. However, we find that it is difficult to estimate y_h from χ due to the strong finite-size corrections.

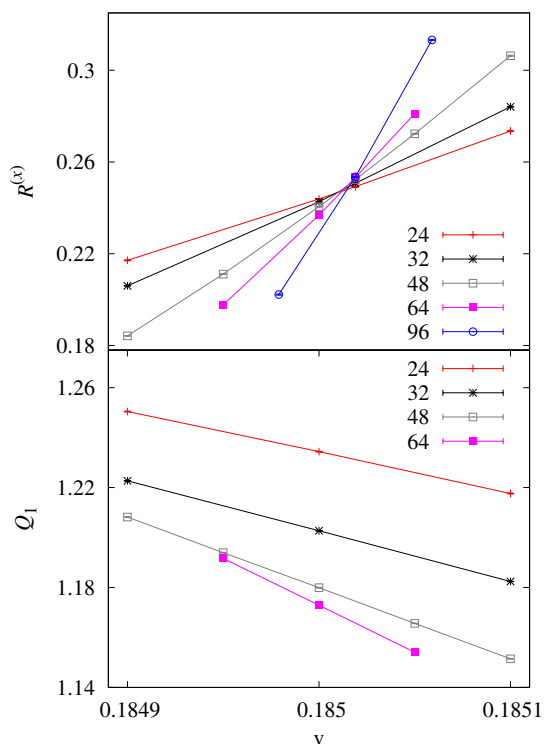


Figure 5.5: Plots of $R_c^{(x)}$ and Q_1 versus v for the leaf-excluded model on the simple-cubic lattice.

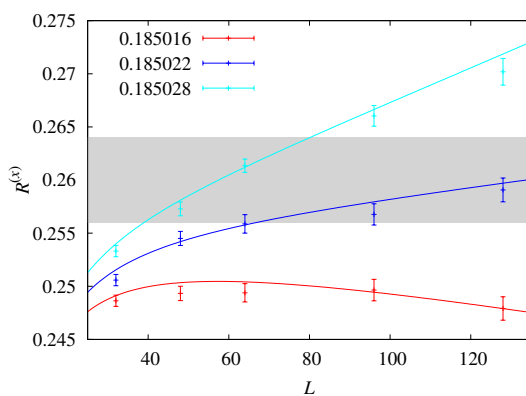


Figure 5.6: Plots of $R_c^{(x)}(p, L)$ versus L for fixed values of p , for the three-dimensional leaf-excluded model. The curves correspond to our preferred fit of the Monte Carlo data. The shaded grey strips indicate an interval of one error bar above and below the estimate $R_c^{(x)} = 0.260(4)$.

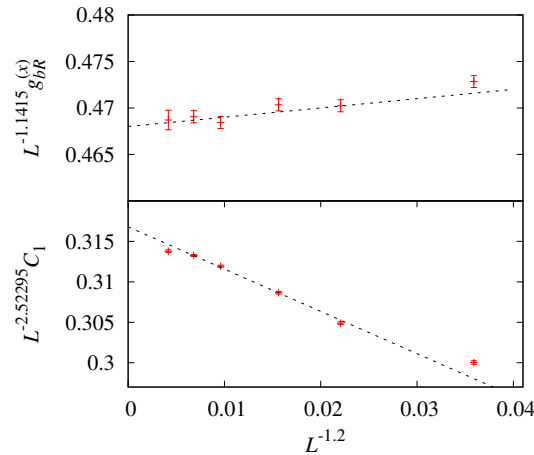


Figure 5.7: Plot of $L^{-1.1415} g_{bR}^{(x)}$ and $L^{-2.52295} C_1$ versus $L^{-1.2}$. The values of the critical exponents used on the vertical axis correspond to the estimates $y_t = 1.1415(15)$ and $y_h = 2.52295(10)$ (Wang et al., 2014, 2013b). The straight lines are simply to guide the eye.

We again illustrate our estimated v_c by plotting $R^{(x)}$ versus L for fixed values of v around our central estimate of v_c . The figure confirms that the true value of v_c lies within two error bars of our central estimate. In this case however, the curvature suggests the central estimate lies slightly above the true value of v_c . See Fig. 5.6. Our estimates for the critical threshold, critical exponents and wrapping probabilities on the simple-cubic lattice are summarized in Tab. 5.1. The agreement with the corresponding values for standard three-dimensional percolation (Wang et al., 2013b) strongly suggests the leaf-excluded model is in the percolation universality class. As further illustration, Fig. 5.7 shows plots of $L^{-y_t} g_{bR}^{(x)}$ and $L^{-y_h} C_1$ versus L^{y_i} , using percolation exponent values taken from (Wang et al., 2013b).

d	Model	v_c	y_t	y_h	$R_c^{(s)}$
2	Leaf-excluded	0.355 247 5(8)	0.751(1)	1.8958(1)	0.5212(2)
	Percolation (Nienhuis, 1984; Pinson, 1994; Ziff <i>et al.</i> , 1999; Hu <i>et al.</i> , 2012)	1	3/4	91/48	0.521 058 290
3	Leaf-excluded	0.185 022(3)	1.143(8)	2.513(5)	0.260(4)
	Percolation (Wang <i>et al.</i> , 2013b, 2014)	0.331 224 4(1)	1.141 5(15)	2.52295(15)	0.257 80(6)

d	Model	$R_c^{(d)}$	$Q_{1,c}$	$Q_{2,c}$
2	Leaf-excluded	0.351 7(1)	1.041 46(10)	1.148 7(2)
	Percolation (Nienhuis, 1984; Pinson, 1994; Ziff <i>et al.</i> , 1999; Hu <i>et al.</i> , 2012)	0.351 642 855	1.041 48(1)	1.148 69(3)
3	Leaf-excluded	0.083(4)	-	-
	Percolation (Wang <i>et al.</i> , 2013b, 2014)	0.080 44(8)	1.155 5(3)	1.578 5(5)

Table 5.1: Summary of our estimates for the thresholds v_c , critical exponents y_t and y_h , and wrapping probabilities for the leaf-excluded model. A comparison with standard bond percolation is also included.

5.4 Discussion

We have introduced in this paper the leaf-excluded model, and investigated its critical behavior. Monte Carlo simulations of the leaf-excluded model were carried out on the square and simple-cubic lattices with periodic boundary conditions. By studying wrapping probabilities, we estimated the critical thresholds $v_c = 0.355\,247\,5(8)$ (square) and $v_c = 0.185\,022(3)$ (simple-cubic). The critical exponents y_t and y_h and wrapping probabilities were found to be consistent with those for standard percolation, which indicates that the phase transition of the leaf-excluded model belongs to the percolation universality class.

As mentioned in the Introduction, rather than enforcing the absence of degree 1 vertices, as we have considered in the current work, one could more generally forbid any specified set of vertex degrees. A very familiar example is to exclude odd vertices, in which case one obtains the high-temperature expansion of the Ising model. Dimer, monomer-dimer, and fully-packed loop models also fit into this framework. A general forbidden-degree model of this kind was studied on the complete graph (i.e. in mean field) from a probabilistic perspective in (?), however questions of universality were not considered. It would be of interest to understand systematically how the choice of forbidden vertex degrees affects the resulting universality class.

Finally, it would be natural to consider a generalization of (5.1.2) which included a cluster fugacity, in addition to the bond fugacity. Such a model would correspond to the Fortuin-Kasteleyn model conditioned on the absence of leaves.

5.5 Acknowledgments

This work is supported by the National Nature Science Foundation of China under Grant No. 11275185, and the Chinese Academy of Sciences. It was also supported under the Australian Research Council's Discovery Projects funding scheme (project number DP110101141), and T.M.G. is the recipient of an Australian Research Council Future Fellowship (project number FT100100494). The simulations were carried out in part on NYU's ITS cluster, which is partly supported by NSF Grant No. PHY-0424082. In addition, this research was undertaken with the assistance of resources provided at the NCI National Facility through the National Computational Merit Allocation Scheme supported by the Australian Government. Y.J.D also acknowledges the Specialized Research Fund for the Doctoral Program of Higher Education under Grant No. 20113402110040 and the Fundamental Research Funds for the Central Universities under Grant No. 2340000034. T.M.G. is grateful for the hospitality shown by the University of Science and Technology of China at which this work was completed, particularly the Hefei National Laboratory for Physical Sciences at Microscale.

Declaration for Thesis Chapter 6

Declaration by candidate

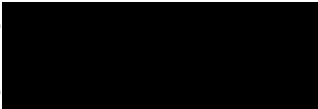
In the case of Chapter 6, the nature and extent of my contribution to the work was the following:

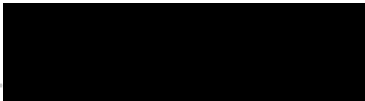
Nature of contribution	Extent of contribution (%)
Prove theorems and lemmas, write the article	80%

The following co-authors contributed to the work. If co-authors are students at Monash University, the extent of their contribution in percentage terms must be stated:

Name	Nature of contribution	Extent of contribution (%) for student co-authors only
Timothy Garoni	Provide guidance and proofreading	

The undersigned hereby certify that the above declaration correctly reflects the nature and extent of the candidate's and co-authors' contributions to this work*.

Candidate's Signature		Date 27/01/2016
-----------------------	---	-----------------

Main Supervisor's Signature		Date 27/01/2016
-----------------------------	---	-----------------

*Note: Where the responsible author is not the candidate's main supervisor, the main supervisor should consult with the responsible author to agree on the respective contributions of the authors.

Chapter 6

*An n -component face-cubic model on
the complete graph*

Chapter 6 is based on the paper in preparation Zhou Z, Garoni TM. 2015. An n -component face-cubic model on the complete graph. in preparation .

Abstract. *In the first part of this paper we rigorously study phase transitions of an n -component face-cubic model on the complete graph with integer $n \geq 1$, by performing a large deviation analysis to the probability distribution of the magnetization, i.e. the empirical mean of spin states. We prove limit theorems for the magnetization, which reveals that phase transitions are continuous for $n \leq 3$ and of first order for $n \geq 4$. We exactly calculate critical points, and for $n \leq 3$ the critical points are equal to n . Both thermal and magnetic exponents are $1/2$ for $n \leq 3$. The second part of this paper is studying the phase diagram of a general n -component face-cubic model on the complete graph. This general model is defined by including a Potts-like interaction to the Hamiltonian of the standard face-cubic model. We rigorously prove the phase diagram for $n = 2$ on the (J_1, J_2) plane, except the region $-J_1 < J_2 < 0$ when $J_1 > 2$. We show that at least four phases exist on the phase diagram: disordered, Ising, Potts, and face-cubic.*

Keywords. *Face-cubic; Phase transitions; Complete graph; Large deviations*

References are considered at the end of the thesis.

Chapter 6

An n -component face-cubic model on the complete graph

6.1 Introduction

Exactly solving non-trivial models with phase transitions is a challenging but important problem in statistical mechanics. An important example is Onsager's solution (Onsager, 1944) of the Ising model on the square lattice. A review of the exactly solvable models in statistical mechanics can be found in Ref. (Baxter, 1982). Despite the difficulty of the calculation, several exact results are now known. For example, critical exponents of two-dimensional percolation are exactly predicted by Coulomb gas argument (Nienhuis, 1987) and conformal field theory (Cardy, 1987). The percolation thresholds on certain two-dimensional lattices are also exactly known (Essam, 1972). However, to provide rigorous proofs for these exact results is extremely difficult. For instance, it was a long-standing conjecture that the critical point for the Fortuin-Kasteleyn random cluster model (Fortuin and Kasteleyn, 1972) on the square lattice is $\sqrt{q}/(1 + \sqrt{q})$, yet this was only rigorously

proved very recently by Beffara and Duminil-Copin in 2012 (Beffara and Duminil-Copin, 2012).

Fortunately, to rigorously study critical behaviors on the complete graph is typically more tractable than on a lattice. A quite early example is the Curie-Weiss model (see Ref. (Ellis, 2005) and the references therein), which is defined as the Ising model on the complete graph. The Curie-Weiss model was rigorously studied in detail around 1980 in Refs. (Ellis and Newman, 1978b,a; Ellis *et al.*, 1980). Precise limit theorems for the magnetization, which is the empirical mean of variables or spins, were proved at all temperatures. From this, a continuous phase transition is indicated at $\beta_c = 1$, with β the inverse of temperature. In 1990, the q -state Curie-Weiss-Potts model (the Potts model on the complete graph) was rigorously studied by Ellis and Wang for $q \geq 3$ (Ellis and Wang, 1990). They proved limit theorems for the empirical vector (also called *type*, defined in Eq. (6.2.3)) at all temperatures, from which a first order transition at $\beta_c = 2(n-1)\log(n-1)/(n-2)$ is revealed.

Another way to generalize the Ising model is the n -component face-cubic model, with n a positive integer. In contrast of the Ising state space $\{-1, 1\}$, the single-spin state space of the face-cubic model consists of $2n$ n -dimensional vectors. Each vector has only one non-zero entry and it is either 1 or -1 . These $2n$ vectors point to the $2n$ face-centers of an n -cube centered at the origin. Therefore the Ising model is the special case of the face-cubic model with $n = 1$. Denote the single-spin state space by Σ . On the complete graph, the face-cubic model is defined by the Hamiltonian

$$H(\omega) = -\frac{1}{2N} \sum_{\alpha, \beta=1}^N \langle \omega_\alpha, \omega_\beta \rangle, \quad \omega \in \Sigma^N, \quad (6.1.1)$$

where N is the number of spins. The interaction between each pair of spins is scaled by $1/2$ to cancel the repeated counting, and by $1/N$ to guarantee an extensive energy. The face-cubic model was introduced in 1975 by Kim and Levy

(Kim *et al.*, 1975; Kim and Levy, 1975) to model the non-trivial critical behaviors of the cubic rare-earth compounds. The mean-field approximation (Kim *et al.*, 1975) predicts that the nature of the phase transitions is continuous for $n \leq 3$ and of first order for $n > 3$; with tricritical exponents at $n = 3$. However, the validity of the mean-field approximation was challenged by the Bethe-Peierls-Weiss and high-temperature approximations, both of which suggest that the transition for $n = 3$ is of first order (Kim and Levy, 1975). To clarify the nature of phase transitions at $n = 3$ was a primary motivation of the present work.

In this paper we present the first rigorous study of the face-cubic model on the complete graph for $n \geq 2$. We apply a large deviation analysis, similar to the methods used in Ref. (Ellis and Wang, 1990), to study limit theorems of the magnetization at all temperatures. Our results prove that the nature of the phase transition is continuous for $n \leq 3$, and of first order for $n \geq 4$. The critical point is $\beta_c = n$ for $n \leq 3$, consistent with the results from the mean-field approximation. At criticality, the central limit theorem for the magnetisation S_N breaks down, and we show $N^{1/4}S_N$ converges in distribution to a random variable whose distribution is non-Gaussian. Then the thermal and magnetic exponents are obtained as $y_t = 1/2$ and $y_h = 1/2$ for all $n \leq 3$. This suggests that, compared with $n = 1$ and 2, no special behavior is observed for $n = 3$.

We also study in this paper a general n -component face-cubic model (Kim *et al.*, 1976) on the complete graph, which is defined by including a Potts-like interaction between spins. Its Hamiltonian is

$$H(\omega) = -\frac{J_1}{2N} \sum_{\alpha, \beta=1}^N \langle \omega_\alpha, \omega_\beta \rangle - \frac{J_2}{2N} \sum_{\alpha, \beta=1}^N \langle \omega_\alpha, \omega_\beta \rangle^2. \quad (6.1.2)$$

The general face-cubic model is remarkable for the possession of both color (Potts) and spin (Ising) orderings, which can be clearly seen from the following special cases. The classic n -state and $2n$ -state Curie-Weiss-Potts models, the Curie-Weiss

model, and the Ashkin-Teller model respectively correspond to $J_1 = 0, J_1 = J_2, n = 1$, and $n = 2$ cases. Many results are known nonrigorously about this general model in two dimensions, such as the schematic phase diagram for general n (Nienhuis *et al.*, 1983), critical points and exponents for the face-cubic, Potts and Ashkin-Teller phase transitions (Blöte and Nightingale, 1984; Guo *et al.*, 2006). We note that the Ashkin-Teller model (Ashkin and Teller, 1943; Fan and Wu, 1970) can be exactly mapped to the $n = 2$ case of the general face-cubic model by redefining $2\omega_\alpha = (\sigma_\alpha + \tau_\alpha, \sigma_\alpha - \tau_\alpha)$ where $\sigma_\alpha, \tau_\alpha \in \{-1, 1\}$. In detail, the Hamiltonian $H(\omega)$ can be written as

$$-\frac{J_1}{4N} \sum_{\alpha, \beta=1}^N (\sigma_\alpha \sigma_\beta + \tau_\alpha \tau_\beta) - \frac{J_2}{4N} \sum_{\alpha, \beta=1}^N (\sigma_\alpha \sigma_\beta \tau_\alpha \tau_\beta + 1). \quad (6.1.3)$$

This is exactly the Hamiltonian of the Ashkin-Teller model if we neglect the constant 1. The phase diagram of the Ashkin-Teller model was studied in 1980 (Ditzian *et al.*, 1980), by mean-field approximations.

In the present paper, we rigorously study the phase diagram of the general face-cubic model on the complete graph, by a large deviation analysis. We prove the phase diagram for $n = 2$ on the (J_1, J_2) plane (except the region $-J_1 < J_2 < 0$ when $J_1 > 2$), and show the existence of the disordered, Ising, Potts and face-cubic phases. Two possible scenarios are considered for this unproved region. One is that there are only the face-cubic and the Ising phases, and the other one is that a new ordered phase is located between them. We call this new phase the super-ordered phase, as colors and spins are ordered simultaneously. Numerical results support the existence of this super-ordered phase. Finding a rigorous proof is left for future work.

The remainder of this paper is organized as follows. Section 6.2 explicitly defines the face-cubic model and the large deviation property of the magnetization. Limit theorems of the magnetization are presented in Section 6.3. The preliminary

results needed to prove limit theorems are summarized in Section 6.4. We then start in Section 6.5 the discussion of the general face-cubic model. The phase diagram is presented in Theorem 6.5.6, with a proof in the subsection after. Propositions and lemmas for proving the phase diagram are given in Section 6.5.4. We finally conclude this paper in Section 6.6.

6.2 The n -component face-cubic model

6.2.1 Model

The face-cubic model on the complete graph is defined by choosing a configuration ω via the Gibbs measure,

$$\rho^\beta(\omega) = \frac{1}{Z_N(\beta)} \exp[-\beta H(\omega)] \rho(\omega), \quad (6.2.1)$$

where the prior measure corresponds to independent uniform spins, $\rho(\omega) = (1/2n)^N$. The parameter $\beta > 0$ is the inverse of temperature, the Hamiltonian $H(\omega) : \Sigma^N \rightarrow \mathbb{R}$ is given by Eq. (6.1.1), and the partition function is

$$Z_N(\beta) = \sum_{\omega \in \Sigma^N} \exp[-\beta H(\omega)] \rho(\omega).$$

On the complete graph, one can verify that $H(\omega)$ can be written as

$$H(\omega) = -\frac{1}{2} N \langle S_N(\omega), S_N(\omega) \rangle, \quad (6.2.2)$$

with $S_N(\omega) := \frac{1}{N} \sum_{\alpha=1}^N \omega_\alpha$, the empirical mean of spin states. In the section below we study the large deviation property for the probability distribution of S_N . We first clarify our notations below: $P(S_N = \cdot)$ is the probability distribution of S_N with

respect to the prior measure $\rho(\omega)$, and $P^\beta(S_N = \cdot)$ is the probability distribution of S_N with respect to Gibbs measure $\rho^\beta(\omega)$.

6.2.2 Large deviations theory

We introduce an example of the large deviations theory in this section, following Chapter 2 in the book by Dembo and Zeitoni (Dembo and Zeitouni, 2009). We first consider the probability distribution of the empirical vector and empirical mean for a sequence of i.i.d. random variables, by recalling the discrete cases of Sanov's and Cramér's theorems. For details of the complete theorems and their proofs, see for example (Dembo and Zeitouni, 2009).

Let $\Sigma = \{a_1, a_2, \dots, a_{|\Sigma|}\}$ be a finite state space. Let $\mathcal{M}_1(\Sigma)$ be the set of all probability measures defined on Σ . Thus, if $\nu \in \mathcal{M}_1(\Sigma)$ then $0 \leq \nu(a_i) \leq 1$ for all $i \in \{1, 2, \dots, |\Sigma|\}$ and $\sum_{i=1}^{|\Sigma|} \nu(a_i) = 1$. Let Y_1, Y_2, \dots be a sequence of i.i.d. random variables with Y_i distributed according to a law $\mu \in \mathcal{M}_1(\Sigma)$. We assume $\mu(a_i) > 0$ for all $i \in \{1, 2, \dots, |\Sigma|\}$. Let Y denote the partial sequence $Y = \{Y_1, Y_2, \dots, Y_N\}$, and y a realization $y = \{y_1, y_2, \dots, y_N\}$. The *type* of a sequence y is defined as

$$L_N^y = (L_{N,1}^y, L_{N,2}^y, \dots, L_{N,|\Sigma|}^y), \quad (6.2.3)$$

with $L_{N,i}^y = \frac{1}{N} \sum_{\alpha=1}^N \mathbf{1}(a_i, y_\alpha)$, the fraction of the occurrence of a_i in the sequence y . Obviously $L_N^y \in \mathcal{M}_1(\Sigma)$ for all sequence $y \in \Sigma^N$.

Denote \mathfrak{L}_N as the set of all outcomes of the random variable L_N^Y . Let $P_\mu(L_N^Y = \cdot)$ be the probability distribution of L_N^Y . For $\nu \in \mathfrak{L}_N$, one has (see Lemma 2.1.9 in Ref. (Dembo and Zeitouni, 2009))

$$(N+1)^{-|\Sigma|} e^{-NH(\nu|\mu)} \leq P_\mu(L_N^Y = \nu) \leq e^{-NH(\nu|\mu)},$$

where

$$H(\nu|\mu) = \sum_{i=1}^{|\Sigma|} \nu_i \ln \frac{\nu_i}{\mu_i}, \quad (6.2.4)$$

is the relative entropy ν with respect to μ . Thus, as $N \rightarrow +\infty$, one has

$$I(\nu) := - \lim_{N \rightarrow +\infty} \frac{1}{N} \log P_\mu(L_N^Y = \nu) = H(\nu|\mu)$$

The function $I(\nu)$ is the rate function of $P_\mu(L_N^Y = \cdot)$. As $N \rightarrow +\infty$, the type of the sequence of random variables is concentrated on those ν for which $I(\nu) = 0$. Note that $I(\nu) = H(\nu|\mu) = 0$ if and only if $\nu = \mu$.

Now suppose $\Sigma \subset \mathbb{R}^d$, and consider the probability distribution of the empirical mean $S_N = \frac{1}{N} \sum_{\alpha=1}^N Y_\alpha$, which can be rewritten as

$$S_N = \frac{1}{N} \sum_{\alpha=1}^N Y_\alpha = \sum_{i=1}^{|\Sigma|} L_{N,i}^Y a_i = \langle L_N^Y, a \rangle, \quad (6.2.5)$$

where a denotes the vector $(a_1, a_2, \dots, a_{|\Sigma|})$. Therefore, the empirical mean of the sequence Y is determined by its type. Let \mathfrak{S}_N be the set of all possible outcomes of S_N , and $P_\mu(S_N = \cdot)$ be the probability distribution of S_N . For $x \in \mathfrak{S}_N$, it is straightforward to obtain

$$I(x) := - \lim_{N \rightarrow +\infty} \frac{1}{N} \log P_\mu(S_N = x) = \inf_{\{\nu: \langle \nu, a \rangle = x\}} H(\nu|\mu). \quad (6.2.6)$$

Here $I(x)$ is the rate function of $P_\mu(S_N = \cdot)$. An explicit expression for the rate function $I(x)$ can be obtained from the Legendre-Fenchel transform of the logarithmic moment generating function $\Lambda(\lambda)$ (see Theorem 2.1.24 in Ref. (Dembo and Zeitouni, 2009)),

$$I(x) = \sup_{\lambda \in \mathbb{R}^d} \{\langle \lambda, x \rangle - \Lambda(\lambda)\}, \quad \text{and} \quad \Lambda(\lambda) = \ln \sum_{i=1}^{|\Sigma|} \mu(a_i) e^{\langle \lambda, a_i \rangle}. \quad (6.2.7)$$

6.2.3 Rate function for $P^\beta(S_N)$

We study in this section the probability distribution of S_N under the Gibbs measure $\rho^\beta(\omega)$, and derive the corresponding rate function. The most probable macroscopic states are those, for which the rate function vanishes. We first consider the free energy which is defined as

$$\beta\psi = - \lim_{N \rightarrow +\infty} \frac{1}{N} \ln Z_N(\beta).$$

From the definition of the partition function $Z_N(\beta)$ we have

$$\begin{aligned} \beta\psi &= - \lim_{N \rightarrow +\infty} \frac{1}{N} \ln Z_N(\beta) \\ &= - \lim_{N \rightarrow +\infty} \frac{1}{N} \ln \sum_{\omega \in \Sigma^N} \exp[-\beta H(\omega)] \rho(\omega) \\ &= - \lim_{N \rightarrow +\infty} \frac{1}{N} \ln \sum_{x \in \mathfrak{G}_N} \exp\{-N[-\beta \langle x, x \rangle / 2 + I(x)]\} \\ &= \min_{x \in \mathfrak{G}_N} [I(x) - \beta \langle x, x \rangle / 2]. \end{aligned}$$

Here we use Eq. (6.2.2) and Eq. (6.2.6).

Consequently, we calculate $P^\beta(S_N = x)$ as

$$\begin{aligned} P^\beta(S_N = x) &:= \frac{1}{Z_N(\beta)} \sum_{\{\omega \in \Sigma^N : S_N(\omega) = x\}} \exp[-\beta H(\omega)] \rho(\omega) \\ &= \frac{1}{Z_N(\beta)} \exp[\beta N \langle x, x \rangle / 2] P(S_N = x), \end{aligned}$$

and find

$$I_\beta(x) := - \lim_{N \rightarrow +\infty} \frac{1}{N} \ln P^\beta(S_N = x) = I(x) - \frac{\beta}{2} \langle x, x \rangle - \beta\psi.$$

Here $I_\beta(x)$ is the rate function of the distribution $P^\beta(S_N = \cdot)$.

A state x is called an *equilibrium macrostate* of the face-cubic model if it satisfies $I_\beta(x) = 0$. Other states with non-zero rate function will vanish as $N \rightarrow +\infty$. The set of all equilibrium macrostates is denoted as $\Omega_m(\beta)$, thus $\Omega_m(\beta) = \{x : I_\beta(x) = 0\}$. To find the set $\Omega_m(\beta)$ is equivalent to finding the set of global minimum points (GMP) of $\{I(x) - \frac{\beta}{2}\langle x, x \rangle\}$. In principle, the function $I(x)$ can be obtained by performing the Legendre-Fenchel transform of the logarithmic generating function $\Lambda(\lambda)$. Let X_1 be a face-cubic spin variable. For all $\lambda \in \mathbb{R}^n$ one has

$$\begin{aligned}\Lambda(\lambda) &:= \ln \mathbb{E}[\exp(\langle \lambda, X_1 \rangle)] = \ln \frac{1}{n} \sum_{i=1}^n \frac{1}{2} (e^{\lambda_i} + e^{-\lambda_i}) \\ &= \ln \frac{1}{n} \sum_{i=1}^n \cosh \lambda_i.\end{aligned}$$

However, to derive $I(x)$ using the transform Eq. (6.2.7) is somewhat complicated. Fortunately, convex duality (Appendix C in (Eisele and Ellis, 1983)) avoids the direct use $I(x)$ and provides the useful relation,

$$\min_{x \in \Omega} [I(x) - \frac{\beta}{2}\langle x, x \rangle] = \min_{\lambda \in \mathbb{R}^n} [\frac{1}{2\beta}\langle \lambda, \lambda \rangle - \Lambda(\lambda)].$$

We note that $\frac{1}{2\beta}\langle \lambda, \lambda \rangle$ is the Legendre-Fenchel transform of $\frac{\beta}{2}\langle x, x \rangle$. Let $\lambda = \beta u$. We now need to find the global minimum points of the function $G_\beta(u)$, defined as

$$G_\beta(u) = \frac{\beta}{2}\langle u, u \rangle - \ln \sum_{i=1}^n \cosh(\beta u_i), \quad \text{with } u \in \mathbb{R}^n. \quad (6.2.8)$$

6.3 Limit theorems

We state in this section limit theorems for the probability distribution of the empirical mean S_N (magnetization). Theorem 6.3.1 discusses existence of laws

of large numbers for S_N . Central limit theorems for different β are considered in Theorems 6.3.3, 6.3.4, 6.3.5.

We first define the following $2n + 1$ vectors: $v^0 = (0, 0, \dots)$, $v^1 = (x(\beta), 0, \dots, 0)$, $v^2 = (0, x(\beta), 0, \dots, 0), \dots, v^n = (0, \dots, 0, x(\beta))$, and $v^{n+i} = -v^i$ for $i = 1, 2, \dots, n$. Here $x(\beta)$ is the global minimum point of the function $A_\beta(x)$,

$$A_\beta(x) = \frac{1}{2}\beta x^2 - \ln[\cosh(\beta x) + n - 1]. \quad (6.3.1)$$

To extend the discrete distribution of S_N to a measure on \mathbb{R}^n , for any set $A \in \mathbb{R}^n$ we introduce

$$\begin{aligned} P(S_N \in A) &= \sum_{v \in \Omega} \mathbf{1}(v \in A) P(S_N = v), \\ P^\beta(S_N \in A) &= \sum_{v \in \Omega} \mathbf{1}(v \in A) P^\beta(S_N = v). \end{aligned} \quad (6.3.2)$$

For convenience, we now state the value of the critical point β_c , with the proof given in Proposition 6.3.2. For $1 \leq n \leq 3$, $\beta_c = n$. For $n \geq 4$, β_c is the solution to the following equations,

$$\frac{1}{2}\beta x^2 - \ln[\cosh(\beta x) + n - 1] = -\ln n \quad (6.3.3)$$

$$x\beta \sinh(\beta x) + (1 - \beta) \cosh(\beta x) + n - 1 = 0, \quad (6.3.4)$$

where $x \in (0, 1)$.

Theorem 6.3.1. (i) For $1 \leq n \leq 3$, S_N converges in distribution to S_* ($S_N \Rightarrow S_*$) where S_* has distribution

$$\begin{cases} \delta_{v^0} & \text{for } 0 < \beta \leq \beta_c \\ \frac{1}{2n} \sum_{i=1}^{2n} \delta_{v^i} & \text{for } \beta > \beta_c, \end{cases} \quad (6.3.5)$$

as $N \rightarrow +\infty$.

(ii) For $n \geq 4$, $S_N \Rightarrow S_*$ where S_* has distribution

$$\begin{cases} \delta_{v^0} & \text{for } 0 < \beta < \beta_c \\ \lambda_0 \delta_{v^0} + \lambda_1 \sum_{i=1}^{2n} \delta_{v^i} & \text{for } \beta = \beta_c \\ \frac{1}{2n} \sum_{i=1}^{2n} \delta_{v^i} & \text{for } \beta > \beta_c, \end{cases} \quad (6.3.6)$$

as $N \rightarrow +\infty$, with

$$\lambda_0 = \frac{\kappa_0}{\kappa_0 + 2n\kappa_1}, \quad \lambda_1 = \frac{\kappa_1}{\kappa_0 + 2n\kappa_1},$$

$$\kappa_0 = \left(\det D^2 G_{\beta_c}(v^0) \right)^{-1/2}, \quad \kappa_1 = \left(\det D^2 G_{\beta_c}(v^1) \right)^{-1/2}.$$

Proof of Theorem 6.3.1. let $W \in \mathbb{R}^n$ a random vector whose entries are independently and normally distributed random variables: $W_i \sim N(0, \beta^{-1})$. Let W be independent of the states of spins ω_i , with $i = 1, 2, \dots, N$. Given a Lebesgue measurable set $V \subseteq \mathbb{R}^n$, we know from Lemma 6.4.4 that

$$P^\beta(N^{-1/2}W + S_N \in V) = \frac{\int_{x \in V} \exp[-NG_\beta(x)] dx}{\int_{x \in \mathbb{R}^n} \exp[-NG_\beta(x)] dx}. \quad (6.3.7)$$

For $\beta > 0$, let $\Omega_m(\beta)$ be the set of global minimum points of $G_\beta(u)$. For each $v_i \in \Omega_m(\beta)$ with $i = 1, 2, \dots, |\Omega_m(\beta)|$, let $B(v_i, b_{v_i})$ be a ball centered at v_i with radius b_{v_i} such that Lemma 6.4.6 can be satisfied. Then we respectively partition V as V_1, V_2 , and partition \mathbb{R}^n as R_1, R_2 , with

$$V_1 = \bigcup_{v_i \in V \cap \Omega_m(\beta)} B(v_i, b_{v_i}), \text{ and } V_2 = V \setminus V_1,$$

$$R_1 = \bigcup_{v_i \in \Omega_m(\beta)} B(v_i, b_{v_i}), \text{ and } R_2 = \mathbb{R}^n \setminus R_1.$$

We let $V_1 = \emptyset$ if $V \cap \Omega_m(\beta) = \emptyset$, and define b_1, b_2 via

$$b_1 = \min\{b_{v_i}, v_i \in V \cap \Omega_m(\beta)\}, \text{ and } b_2 = \min\{b_{v_i}, v_i \in \Omega_m(\beta)\}.$$

Multiplying both nominator and denominator of Eq. (6.3.7) by $e^{N\bar{G}_\beta}$, where $\bar{G}_\beta = \min_{v \in \Omega} G_\beta(u)$, yields

$$\begin{aligned} & P_N^\beta(N^{-1/2}W + S_N \in V) \\ &= \frac{e^{N\bar{G}_\beta} \int_{x \in V_1} \exp[-NG_\beta(x)] dx + e^{N\bar{G}_\beta} \int_{x \in V_2} \exp[-NG_\beta(x)] dx}{e^{N\bar{G}_\beta} \int_{x \in R_1} \exp[-NG_\beta(x)] dx + e^{N\bar{G}_\beta} \int_{x \in R_2} \exp[-NG_\beta(x)] dx}. \end{aligned}$$

Lemma 6.4.5 tells us that both the integrals over V_2 and R_2 behaves as $O(e^{-N\epsilon})$. Thus we only consider here the ratio of the integrals over V_1 and R_1 . Our discussions are separated into the following two cases.

For $\beta \leq \beta_c$ ($n \leq 3$) and $\beta < \beta_c$ ($n \geq 4$), where $\Omega_m(\beta) = \{v^0\}$ from Proposition 6.3.2, we have $P_N^\beta(S_N \in V) \Rightarrow \delta_{v^0}(V)$ as $N \rightarrow +\infty$.

For $\beta > \beta_c$ ($n \geq 1$), where $\Omega_m(\beta) = \{v^1, v^2, \dots, v^{2n}\}$, from Lemma 6.4.6 we have as $N \rightarrow +\infty$,

$$P_N^\beta(S_N \in V) \sim \frac{\sum_{i=1}^{2n} \det[D^2G_\beta(v^i)] \delta_{v^i}(V)}{\sum_{i=1}^{2n} \det[D^2G_\beta(v^i)]} = \frac{1}{2n} \sum_{i=1}^{2n} \delta_{v^i}(V).$$

For $\beta = \beta_c$ ($n \geq 3$), where $\Omega_m(\beta) = \{v^0, v^1, v^2, \dots, v^{2n}\}$, from Lemma 6.4.6 we have as $N \rightarrow +\infty$,

$$P_N^\beta(S_N \in V) \sim \frac{\det[D^2G_\beta(v^0)] \delta_{v^0}(V) + \sum_{i=1}^{2n} \det[D^2G_\beta(v^i)] \delta_{v^i}(V)}{\det[D^2G_\beta(v^0)] + \sum_{i=1}^{2n} \det[D^2G_\beta(v^i)]}.$$

The theorem then follows by defining $\kappa_0, \kappa_1, \lambda_0, \lambda_1$ as in Eq. (6.3.7). \square

The following proposition locates the global minimum points of the function $G_\beta(u)$.

Proposition 6.3.2. *Let $\Omega_m(\beta)$ be the set of global minimum points of $G_\beta(u)$.*

(i) For $1 \leq n \leq 3$,

$$\Omega_m(\beta) = \begin{cases} \{v^0\} & \text{if } 0 < \beta \leq \beta_c \\ \{v^1, v^2, \dots, v^{2n}\} & \text{if } \beta > \beta_c. \end{cases} \quad (6.3.8)$$

(ii) For $n \geq 4$,

$$\Omega_m(\beta) = \begin{cases} \{v^0\} & \text{if } 0 < \beta < \beta_c \\ \{v^0, v^1, v^2, \dots, v^{2n}\} & \text{if } \beta = \beta_c \\ \{v^1, v^2, \dots, v^{2n}\} & \text{if } \beta > \beta_c. \end{cases} \quad (6.3.9)$$

Here $\beta_c = n$ for $1 \leq n \leq 3$. For $n \geq 4$, β_c is obtained by solving the following equations,

$$\begin{aligned} \frac{1}{2}\beta x^2 - \ln[\cosh(\beta x) + n - 1] &= -\ln n \\ x\beta \sinh(\beta x) + (1 - \beta)\cosh(\beta x) + n - 1 &= 0, \end{aligned} \quad (6.3.10)$$

with $x \in (0, 1)$.

Proof. Fix $n \geq 1$. From Lemma 6.4.2, we know one of the global minimum points of $G_\beta(u)$ can be denoted as $\bar{v} = (x, 0, 0, \dots, 0)$, with $|x| < 1$ a function of β . Due to the symmetry of $G_\beta(u)$, the other global minimum points can be obtained by exchanging x with any one of those zero entries. Now we can simplify $G_\beta(u)$ as a function of x , which is

$$A_\beta(x) = G_\beta(u = \bar{v}) = \frac{1}{2}\beta x^2 - \ln[\cosh(\beta x) + n - 1], \quad (6.3.11)$$

where $|x| < 1$. We next study the minimum of $A_\beta(x)$. Since $A_\beta(x)$ is an even function of x , we only need to consider $x \in [0, 1)$. We first let the first derivative of $A_\beta(x)$ be zero, which is

$$A'_\beta(x) = \beta x - \frac{\beta \sinh(\beta x)}{\cosh(\beta x) + n - 1} = 0. \quad (6.3.12)$$

One trivial solution is $x = 0$. The second derivative $A''_\beta(x = 0) = \beta(1 - \beta/n)$, which is positive for $\beta < n$ and negative for $\beta > n$, implying that for the vector v^0 is respectively a local minimum and maximum for $\beta < n$ and $\beta > n$. We then look for other extremas.

We rewrite (6.3.12) as

$$\begin{aligned} A'_\beta(x) &= \frac{\beta}{\cosh(\beta x) + n - 1} [x \cosh(\beta x) - \sinh(\beta x) + (n - 1)x] \\ &= \frac{\beta}{\cosh(\beta x) + n - 1} f(x). \end{aligned}$$

Since the denominator in the right-hand side is always positive, we then only need to consider $f(x)$. Two properties about $A'_\beta(x)$ are known, which are $A'_\beta(x = 0) = 0$ and $A'_\beta(x = 1) > 0$. We then want to know if there are other extremas in $(0, 1)$, which is to find the solutions of $f(x) = 0$. Let $g_\beta(x)$ be the first derivative of $f(x)$,

$$g_\beta(x) = f'(x) = x\beta \sinh(\beta x) + (1 - \beta) \cosh(\beta x) + n - 1. \quad (6.3.13)$$

In Lemma 6.4.3, we show $g_\beta(x) = 0$ has at most two non-zero solutions in $(0, 1)$. We denote the solution as $s_1(\beta)$ if there is only one solution; use $s_1(\beta)$ and $s_2(\beta)$ if there are two solutions and let $s_1(\beta) < s_2(\beta)$. Lemma 6.4.3 gives the extremas of $g_\beta(x)$ in the regime $x \in [0, 1]$, from which we conclude as follows.

For $n \leq 3$, the solutions to $g_\beta(x) = 0$ are respectively none, $x = 0$ and $x = s_1(\beta)$ for $\beta < n$, $\beta = n$ and $\beta > n$. Then in the regime $x \in (0, 1]$, $f(x)$ is positive for $\beta \leq n$.

For $\beta > n$, $f(x)$ is negative in $(0, s_1(\beta))$ and positive in $(s_1(\beta), 1]$. Thus, the global minimum points of $A_\beta(x)$ are respectively $x = 0$ and $x = s_1(\beta)$ for $\beta \leq n$ and $\beta > n$.

For $n \geq 4$, by similar arguments we know $x = s_1(\beta)$ is the global minimum point of $A_\beta(x)$ for $\beta \geq n$. We then consider the $\beta < n$ case. For $\beta \leq 3$, we have $f(x) > 0$ for $x \in [0, 1]$, thus $x = 0$ is the unique global minimum point of $A_\beta(x)$. As β increases, some β (say β_1) is arrived such that there exists a unique solution to $g_{\beta_1}(x) = 0$ in $(0, 1)$. As β keeps increasing, there exist two solutions to $g_\beta(x) = 0$ in $(0, 1)$, denoted as $s_1(\beta)$ and $s_2(\beta)$ with $s_1(\beta) < s_2(\beta)$. Moreover $s_2(\beta)$ is a local minimum point and $s_1(\beta)$ is a local maximum point. As we increase β from β_1 to n , we sequentially have $A_\beta(0) < A_\beta(s_2(\beta))$, $A_\beta(0) = A_\beta(s_2(\beta))$ and $A_\beta(0) > A_\beta(s_2(\beta))$, respectively for $\beta_1 < \beta < \beta_c$, $\beta = \beta_c$, and $\beta > \beta_c$. Here β_c is the solution to Eqs. (6.3.10).

□

We now study the central limit theorems for S_N for all $\beta > 0$, in the next three theorems. We first propose a theorem for $0 < \beta < \beta_c$.

Theorem 6.3.3. *For all $n \geq 1$ and $0 < \beta < \beta_c$, as $N \rightarrow +\infty$,*

$$P^\beta\{\sqrt{N}(S_N - \nu^0)\} \Rightarrow N(0, [D^2G_\beta(\nu^0)]^{-1} - \beta^{-1}I), \quad (6.3.14)$$

where I is the $n \times n$ identity matrix, and the covariance matrix $(D^2G_\beta(\nu^0)^{-1} - \beta^{-1}I)$ is positive definite and has an eigenvalue $(n - \beta)^{-1}$ with multiplicity n .

Proof. For any $t \in \mathbb{R}^n$ and $W \sim N(0, \beta^{-1}I)$, the generating function of $W + \sqrt{N}(S_N - \nu^0)$ is

$$\mathbb{E}\left\{\exp\left[\langle t, W + \sqrt{N}(S_N - \nu^0) \rangle\right]\right\}$$

$$\begin{aligned}
 &= \frac{\int_{\mathbb{R}^n} \exp\left[-NG_\beta\left(\nu^0 + \frac{x}{\sqrt{N}}\right) + \langle t, x \rangle\right] dx}{\int_{\mathbb{R}^n} \exp\left(-NG_\beta\left(\nu^0 + \frac{x}{\sqrt{N}}\right)\right) dx} \\
 &= \frac{e^{-\sqrt{N}\langle t, \nu^0 \rangle} \int_{\mathbb{R}^n} \exp\left[-NG_\beta(x') + \sqrt{N}\langle t, x' \rangle\right] dx'}{\int_{\mathbb{R}^n} \exp\left[-NG_\beta(x')\right] dx'} \\
 &= \frac{e^{-\sqrt{N}\langle t, \nu^0 \rangle} \int_{B(\nu^0, b_0)} \exp\left[-NG_\beta(x') + \sqrt{N}\langle t, x' \rangle\right] dx'}{\int_{B(\nu^0, b_0)} \exp\left[-NG_\beta(x')\right] dx'} \\
 &= \frac{\int_{\mathbb{R}^n} \exp\left[-\frac{1}{2}\langle x, D^2G_\beta(\nu^0)x \rangle + \langle t, x \rangle\right] dx}{\int_{\mathbb{R}^n} \exp\left[-\frac{1}{2}\langle x, D^2G_\beta(\nu^0)x \rangle\right] dx} \\
 &= \exp\left[\frac{1}{2}\langle t, [D^2G_\beta(\nu^0)]^{-1}t \rangle\right]. \tag{6.3.15}
 \end{aligned}$$

with an explanation present as follows. The first equality follows from Lemma 6.4.4. Then we change the variable $x \rightarrow x' = \nu^0 + x/\sqrt{N}$ and have the second equality. Multiplying both the nominator and denominator of right-hand side of the second equality by $e^{N\bar{G}_\beta}$ and using Lemma 6.4.5 result the third equality. We remind that $\bar{G}_\beta = G_\beta(\nu^0)$ for $\beta < \beta_c$, and $B(\nu^0, b_0)$ denotes the ball centered at ν^0 with the radius b_0 defined in Lemma 6.4.6. The fourth equality is obtained by directly using Lemma 6.4.6 and changing back x' to x . The last equality follows by calculating integral for matrix and noting that the eigenvalue of the matrix $[D^2G_\beta(\nu^0)]^{-1}$ (the inverse matrix of $D^2G_\beta(\nu^0)$) is the reciprocal of the eigenvalue of $D^2G_\beta(\nu^0)$.

Since $W \sim N(0, \beta^{-1}I)$, we have $\mathbb{E}[e^{\langle t, W \rangle}] = \exp\left(\frac{t^2}{2\beta}\right)$. The theorem then follows by noticing the fact that W and $\sqrt{N}(S_N - \nu^0)$ are independent which yields

$$\mathbb{E}\left\{\exp\left[\langle t, \sqrt{N}(S_N - \nu^0) \rangle\right]\right\} = \exp\left[\frac{1}{2}\langle t, \left([D^2G_\beta(\nu^0)]^{-1} - \beta^{-1}I\right)t \rangle\right]. \tag{6.3.16}$$

The matrix $D^2G_\beta(v^0)$ has an positive eigenvalue $\beta(1 - \beta/n)$ with multiplicity n since $D^2G_\beta(v^0) = \beta(1 - \beta/n)I$. Thus, the covariance matrix $\left[D^2G_\beta(v^0)\right]^{-1} - \beta^{-1}I$ has an positive eigenvalue $(n - \beta)^{-1}$ with multiplicity n . \square

We next consider central limit theorems for $\beta \geq \beta_c$. For $\beta = \beta_c$ and $n \leq 3$, the central limit theorem for $\sqrt{N}S_N$ fails to hold, but we show that $N^{1/4}S_N$ has a biquadratic probability distribution function. For $\beta > \beta_c$ and $n \leq 3$, we show that a central limit theorem holds in a small region containing only one of the global minimum point of $G_\beta(u)$. Such conditional central limit theorems also hold for $\beta \geq \beta_c$ and $n \geq 4$.

The next theorem is for $\beta = \beta_c = n$ and $n \leq 3$. The proof follows and generalizes the proof for the Curie-Weiss model (Theorem V9.5 in (Ellis, 2005)).

Theorem 6.3.4. *For $\beta = \beta_c = n$ and $1 \leq n \leq 3$, the random variable $N^{1/4}S_N$ converges in distribution to a random vector X which has the probability density function proportional to*

$$\exp\left(-\frac{1}{12} \sum_{i,j,k,l} x_i x_j x_k x_l \frac{\partial^4 G_\beta(x)}{\partial x_i \partial x_j \partial x_k \partial x_l}\right) \quad (6.3.17)$$

Proof. We start by calculating the expectation $\mathbb{E}\left[\exp\left(N^{1/4}\langle r, S_N \rangle\right)\right]$ for any $r \in \mathbb{R}^n$, which is

$$\frac{\int_{\Sigma^N} \exp\left[N^{1/4}\langle r, S_N \rangle + \frac{\beta N}{2}\langle S_N, S_N \rangle\right] \rho_N(d\omega)}{\int_{\Sigma^N} \exp\left[\frac{\beta N}{2}\langle S_N, S_N \rangle\right] \rho_N(d\omega)}.$$

We remind that Σ is the state space of the spins. Here we just need to calculate the nominator, since the denominator can be obtained by setting $r = 0$. Let $\sqrt{\beta N}S_N = y$ then the integral in the nominator can be written as

$$\begin{aligned} & \int_{\Sigma^N} \exp\left[(N\beta^2)^{-1/4}\langle r, y \rangle + \frac{1}{2}\langle y, y \rangle\right] \rho_N(d\omega) \\ &= \exp\left[\frac{-\langle r, r \rangle}{2\beta\sqrt{N}}\right] \int_{\Sigma^N} \exp\left[\frac{1}{2}\langle y + \frac{r}{(\beta^2 N)^{1/4}}, y + \frac{r}{(\beta^2 N)^{1/4}} \rangle\right] \rho_N(d\omega) \end{aligned}$$

$$= (2\pi)^{-n/2} n^{-N} (N\beta^2)^{1/4} \exp\left[\frac{-\langle r, r \rangle}{2\beta\sqrt{N}}\right] \int_{\mathbb{R}^n} \exp\left[-NG_\beta(x/N^{1/4}) + \langle r, x \rangle\right] dx.$$

The last step follows by first using the identity

$$\exp\left[\frac{1}{2}\langle t, t \rangle\right] = (2\pi)^{-n/2} \int_{\mathbb{R}^n} \exp\left[\langle t, x \rangle - \frac{1}{2}\langle x, x \rangle\right] dx,$$

where $t = y + r/(\beta^2 N)^{1/4}$ in our case. Then we take the integral over $\rho_N(d\omega)$, and obtain

$$\begin{aligned} \int_{\Sigma^N} \exp[\langle y, x \rangle] \rho_N(d\omega) &= \int_{\Sigma^N} \exp\left[\sum_{i=1}^n \langle \sqrt{\beta/N} \omega_i, x \rangle\right] \rho_N(d\omega) \\ &= \prod_{i=1}^N \int_{\Sigma} \exp[\langle \sqrt{\beta/N} \omega_i, x \rangle] \rho(d\omega) \\ &= n^{-N} \left[\sum_{i=1}^n \cosh(\sqrt{\beta/N} x_i) \right]^N \end{aligned}$$

The third equality then follows by using the definition of the function $G_\beta(x)$ and redefine x as $x/\sqrt{\beta/N^{1/2}}$. Combine with Eq. (6.3.18) and let $N \rightarrow +\infty$ we have

$$\mathbb{E}\left[\exp\left(N^{1/4}\langle r, S_N \rangle\right)\right] = \frac{\int_{\mathbb{R}^n} \exp\left[-NG_\beta(x/N^{1/4}) + \langle r, x \rangle\right] dx}{\int_{\mathbb{R}^n} \exp\left[-NG_\beta(x/N^{1/4})\right] dx}.$$

Therefore $N^{1/4}S_N$ has a probability density function proportional to $\exp[-NG_\beta(x/N^{1/4})]$. The theorem follows by noticing that the first, second, and third derivatives of $G_\beta(u)$ are all zero. \square

The last theorem is for the limit theorem for $\beta > \beta_c$ with $1 \leq n \leq 3$ and for $\beta \geq \beta_c$ with $n \geq 4$.

Theorem 6.3.5. For $\beta > \beta_c$ with $1 \leq n \leq 3$ and for $\beta \geq \beta_c$ with $n \geq 4$, let $\Omega_m(\beta)$ be the set of global minimum points of $G_\beta(u)$. Let $d(\beta)$ be the minimum distance between any pair of global minimum points. For any $\delta \in (0, d(\beta))$ and $v^i \in \Omega_m$, the following

conditional probability holds,

$$P_N^\beta\{\sqrt{N}(S_N - v^i)|S_N \in B(v^i, \delta)\} \Rightarrow N\left(0, [D^2G_\beta(v^i)]^{-1} - \beta^{-1}I\right). \quad (6.3.18)$$

The proof to this theorem is the same as the proof of Theorem 2.5 in (Ellis and Wang, 1990), and thus we omit it here.

6.4 Preliminary results needed to prove theorems

Lemma 6.4.1. For $\beta > 0$, $G_\beta(u)$ is a real analytic function of $u \in \mathbb{R}^n$. There exists a real number $M_\beta > 0$, such that for $\|u\| \geq M_\beta$ we have $G_\beta(u) \geq \frac{\beta}{4}\langle u, u \rangle$.

Proof. Because $G_\beta(u)$ is an even function, here we only need to consider all $u_i \geq 0$.

We have

$$\begin{aligned} G_\beta(u) &= \frac{\beta}{2}\langle u, u \rangle - \ln \sum_{i=1}^n \cosh(\beta u_i) \\ &\geq \frac{\beta}{2}\langle u, u \rangle - \ln \sum_{i=1}^n e^{\beta u_i} \\ &= \frac{\beta}{2}\langle u, u \rangle - \ln \prod_{j=1}^n e^{\beta u_j} \sum_{i=1}^n \frac{e^{\beta u_i}}{\prod_{j=1}^n e^{\beta u_j}} \\ &\geq \frac{\beta}{2}\langle u, u \rangle - \ln \prod_{j=1}^n e^{\beta u_j} - \ln n \\ &\geq \frac{\beta}{4}\langle u, u \rangle + \frac{\beta}{4} \sum_{i=1}^n (u_i - 2)^2 - n\beta - \ln n. \end{aligned}$$

Choosing some M_β such that $\frac{\beta}{4} \sum_{i=1}^n (u_i - 2)^2 - n\beta - \ln n \geq 0$ for $\|u\| \geq M_\beta$, the lemma then follows. \square

We then aim to find the set of global minimum points of $G_\beta(u)$. The next lemma imposes a constraint on the possible global minimum points.

Lemma 6.4.2. *If \bar{v} is a global minimum point of $G_\beta(u)$, then \bar{v} must be one of the following $2n + 1$ vectors: $v^0 = (0, 0, \dots, 0)$, $v^1 = (x, 0, 0, \dots, 0)$, $v^2 = (0, x, 0, \dots, 0)$, \dots , $v^n = (0, \dots, 0, x)$, and $v^{n+i} = -v^i$ for $i = 1, 2, \dots, n$, and $|x| < 1$.*

Proof. If \bar{v} is a global minimum point of $G_\beta(u)$, one must have

$$\left(\frac{\partial G_\beta(u)}{\partial u_i} \right)_{u=\bar{v}} = \bar{v}_i - \frac{\sinh(\beta \bar{v}_i)}{\sum_{i=1}^n \cosh(\beta \bar{v}_i)} = 0. \quad (6.4.1)$$

We have $\bar{v}_i \in (-1, 1)$, since from the above equation $\bar{v}_i \leq \frac{\sinh(\beta \bar{v}_i)}{\cosh(\beta \bar{v}_i)}$ which is bounded by -1 and 1 .

We next show that if \bar{v} is a global minimum point of $G_\beta(u)$, the number of non-zero entries in \bar{v} is at most one. In Eq.(6.4.1), a trivial solution is $\bar{v}_i = 0$. Thus $\bar{v}^0 = (0, 0, \dots, 0)$ is a possible global minimum of $G_\beta(u)$. If there are more than one non-zero entries in \bar{v} , for example \bar{v}_i and \bar{v}_j , we must have $\sinh(\bar{v}_i)/\bar{v}_i = \sinh(\bar{v}_j)/\bar{v}_j$. Since $\sinh(x)/x$ is an even function, it directly follows that $|\bar{v}_i| = |\bar{v}_j|$. This means that all non-zero entries in \bar{v} have the same absolute value, and we denote this value as x . Next we will show that if there are more than one non-zero entry in \bar{v} , then \bar{v} is not a global minimum.

Assume $\bar{v}_k, \bar{v}_l \neq 0$ for some $1 \leq k \leq l \leq n$ and define a vector w as a function of t in the following way: $w_k = 2x - t$ and $w_l = t$ and $w_i = \bar{v}_i$ for $i \neq k, l$. Let $W(t) = G_\beta(u = w(t))$ and take the second derivative of $W(t)$ at the point $t = x$, we have

$$\left(\frac{\partial^2 W(t)}{\partial t^2} \right)_{t=x} = 2\beta \left(1 - \frac{\beta x}{\tanh(\beta x)} \right). \quad (6.4.2)$$

Since the right hand side is always negative for $x \neq 0$, the vector $w(t = x)$ is a local maximum. Therefore, if \bar{v} is a GMP of $G_\beta(u)$, the number of non-zero entries in \bar{v} is at most one. The Lemma 6.4.2 then follows by the symmetry of $G_\beta(u)$. \square

Lemma 6.4.3. *Define the function*

$$g_\beta(x) = x\beta \sinh(\beta x) + (1 - \beta) \cosh(\beta x) + n - 1, \quad (6.4.3)$$

where $x \in [0, 1]$, $\beta > 0$, and n is a positive integer. Define the set $\Omega_X := \{x : g(x) = 0\}$. Then we have the following results.

(i) For $1 \leq n \leq 3$,

$$\Omega_X = \begin{cases} \emptyset & \text{if } \beta < n \\ \{0\} & \text{if } \beta = n \\ \{s_1(\beta)\} & \text{if } \beta > n. \end{cases} \quad (6.4.4)$$

(ii) For $n \geq 4$,

$$\Omega_X = \begin{cases} \emptyset & \text{if } \beta < \beta' \\ \{0\} & \text{if } \beta = \beta' \\ \{s_1(\beta), s_2(\beta)\} & \text{if } \beta' < \beta < n \\ \{0, s_1(\beta)\} & \text{if } \beta = n \\ \{s_1(\beta)\} & \text{if } \beta > n. \end{cases} \quad (6.4.5)$$

The value of β' is determined by solving the following equations.

$$g_\beta(x) = 0, \quad \tanh(\beta x) = \frac{\beta}{\beta - 2} x. \quad (6.4.6)$$

The number of non-zero solutions to $g_\beta(x) = 0$ is at most two, and they are denoted as $s_1(\beta), s_2(\beta)$ and $0 < s_1(\beta) \leq s_2(\beta) < 1$.

Proof. We start the proof by considering the boundary value of $g_\beta(x)$ at $x = 0$ and $x = 1$. We have $g_\beta(x = 0) = (n - \beta)$, which is respectively positive, zero and

negative for $\beta < n$, $\beta = n$, and $\beta > n$. For $x = 1$, we have $g_\beta(x = 1) = \beta \sinh(\beta) + (1 - \beta) \cosh(\beta) + n - 1$, which is positive for any $\beta > 0$ and any positive integer n , with reasons given as below. We first note that $g_\beta(x = 1)$ is an increasing function of n , thus it is sufficient if we show that $g_\beta(x = 1) > 0$ for $n = 1$, which is $g_\beta(x = 1, n = 1) = e^{-\beta}(e^{2\beta} + 1 - 2\beta)/2$. The part $(e^{2\beta} + 1 - 2\beta)$ is positive since it is an increasing function of β with positive initial value at $\beta = 0$.

Now we know that $g_\beta(x)$ is a function which initializes at $x = 0$ with a positive, zero and negative value, respectively for $\beta < n$, $\beta = n$, and $\beta > n$, and reaches a positive value at $x = 1$. To determine the number of solutions to $g_\beta(x) = 0$ with $x \in (0, 1)$, we first study the number of extremas of $g_\beta(x)$ in this regime. We next show that there are at most two extremas of $g_\beta(x)$ for $x \in (0, 1)$. To see this point, we consider the first derivative of $g_\beta(x)$ which is

$$g'_\beta(x) = \beta [(2 - \beta) \sinh(\beta x) + \beta x \cosh(\beta x)] .$$

Letting $g'(x) = 0$ yields

$$(\beta - 2) \tanh(\beta x) = \beta x . \tag{6.4.7}$$

We then separate our discussions as follows.

The $\beta \leq 3$ case. In this case, the only solution to (6.4.7) is $x = 0$ and thus $g_\beta(x)$ is an increasing function of $x \in [0, 1]$. Thus for $\beta < n$, $\beta = n$ and $\beta > n$, the solution set Ω_X are respectively $\{\emptyset\}$, $\{0\}$ and $\{s_1(\beta)\}$.

The $\beta \geq 4$ case. In this case, there exists a unique non-zero solution to (6.4.7), implying that there is a unique extrema in the regime $x \in (0, 1)$. Thus, for $\beta = n$ and $\beta > n$, where $g_\beta(x = 0)$ is zero and negative respectively, the solution set is $s_1(\beta)$. For $\beta < n$, although $g_\beta(x)$ has a unique extrema, the existence of non-zero solutions to $g_\beta(x) = 0$ still depends on the value of β . As β increases from 3 to n , the equation $g_\beta(x) = 0$ has respectively no solution, a unique solution $s_1(\beta)$ and

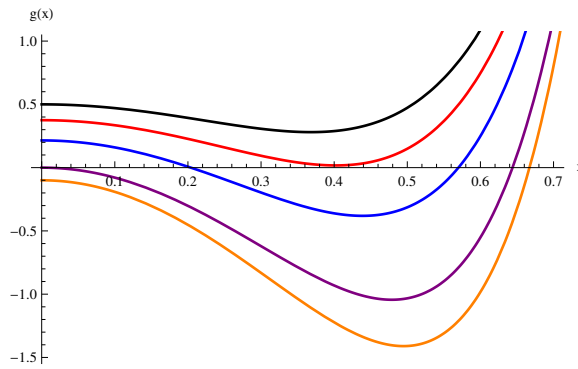


Figure 6.1: Plot of $g_\beta(x)$ versus x for $n = 4$. The curves from top to bottom respectively correspond to $\beta = 3.5, 3.625, 3.785, 4, 4.1$. The values of 3.625 and 3.785 are respectively the estimates of β' and β_c . The reason that $\beta_c \approx 3.785$ can be seen in Fig. 6.2

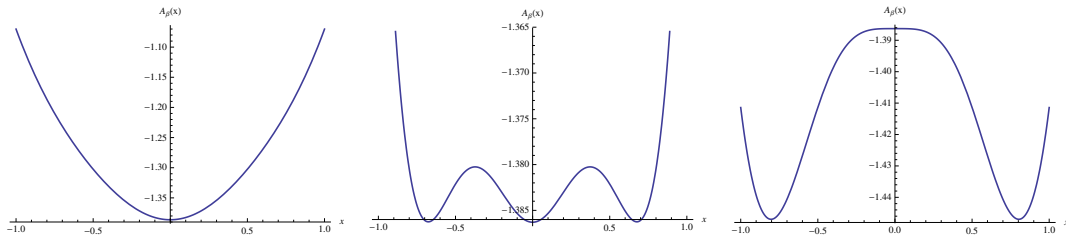


Figure 6.2: Plot of $A_\beta(x)$ versus x for $n = 4$. From left to right, plots respectively correspond to $\beta = 3, \beta = 3.785$, and $\beta = 4$. A first order phase transition can be seen around $\beta = 3.785$.

two solutions $s_1(\beta), s_2(\beta)$, respectively for $3 < \beta < \beta'$, $\beta = \beta'$ and $\beta' < \beta < n$. The value of β' is the solution to the equations (6.4.6).

The theorem follows by combining the cases $\beta \leq 3$ and $\beta \geq 4$. □

The following Lemma plays a central role in proving our limit theorems. The proof given follows the proof of Lemma 3.2 in (Ellis and Wang, 1990).

Lemma 6.4.4. For $\beta > 0$, let $W \in \mathbb{R}^n$ a random vector whose entries are independently and normally distributed random variables: $W_i \sim N(0, \beta^{-1})$. Let W be independent of ω_i , for all $i = 1, 2, \dots, N$. Then for any $m \in \mathbb{R}^n$ and $\gamma \in \mathbb{R}$ and any $N = 1, 2, \dots$, the

probability density function of $\frac{W}{N^{1/2-\gamma}} + \frac{N(S_N - m)}{N^{1-\gamma}}$ is

$$f(x) = \frac{\exp\left[-NG_\beta\left(m + \frac{x}{N^\gamma}\right)\right]}{\int_{x \in \mathbb{R}^n} \exp\left[-NG_\beta\left(m + \frac{x}{N^\gamma}\right)\right] dx}. \quad (6.4.8)$$

Proof. We first consider the probability $P^\beta\left(\frac{W}{N^{1/2-\gamma}} + \frac{N(S_N - m)}{N^{1-\gamma}} \leq \xi\right)$, which is equivalent to $P^\beta(N^{1/2}W + NS_N \leq A_N(\xi))$ with $A_N(\xi) = N^{1-\gamma}\xi + Nm$. Since

$$P^\beta(NS_N \in dx) = \frac{1}{Z_N(\beta)} \exp\left(\frac{\beta}{2N}\langle x, x \rangle\right) P(NS_N \in dx),$$

we have

$$\begin{aligned} & P^\beta(N^{1/2}W + NS_N \leq A_N(\xi)) \\ &= \int_{x \in \mathbb{R}^n} P^\beta(NS_N \in dx) P(N^{1/2}W \leq A_N(\xi) - x) \\ &= \frac{1}{Z_N(\beta)} \int_{x \in \mathbb{R}^n} \exp\left(\frac{\beta}{2N}\langle x, x \rangle\right) P(NS_N \in dx) \\ &\quad \times \left(\frac{\beta}{2\pi N}\right)^{n/2} \int_{t \leq A_N(\xi) - x} \exp\left(-\frac{\beta}{2N}\langle t, t \rangle\right) dt. \end{aligned}$$

Substitute $t - x = u$, one has

$$\begin{aligned} & P^\beta(N^{1/2}W + NS_N \leq A_N(\xi)) \\ &= \frac{1}{Z_N(\beta)} \left(\frac{\beta}{2\pi N}\right)^{n/2} \int_{u \leq A_N(\xi)} \exp\left(-\frac{\beta}{2N}\langle u, u \rangle\right) du \\ &\quad \times \int_{x \in \mathbb{R}^n} \exp\left(\frac{\beta}{N}\langle u, x \rangle\right) P(NS_N \in dx) \end{aligned}$$

The inner integral in the right-hand side is

$$\begin{aligned} \int_{x \in \mathbb{R}^n} \exp\left[\frac{\beta}{N}\langle u, x \rangle\right] P(NS_N \in dx) &= \sum_{\omega \in \Sigma^N} \exp\left[\frac{\beta}{N}\langle u, NS_N \rangle\right] \rho_N(\omega) \\ &= \mathbb{E}[\exp[\beta\langle u, S_N \rangle]] \end{aligned}$$

$$= \exp[N\Lambda(\beta u/N)],$$

where Λ is the logarithmic moment generating function. Using the Eq. (6.2.8) for $\Lambda(\beta u/N)$, we have

$$\begin{aligned} & P_N^\beta \left(\frac{W}{N^{1/2-\gamma}} + \frac{N(S_N - m)}{N^{1-\gamma}} \leq \xi \right) \\ &= \frac{1}{Z_N(\beta)} \left(\frac{\beta}{2\pi N} \right)^{n/2} \int_{u \leq A_N(\xi)} \exp[-NG_\beta(u/N) - N \ln n] du \\ &= \frac{1}{Z_N(\beta)} \left(\frac{\beta}{2\pi N} \right)^{n/2} \frac{N^{(1-\gamma)n}}{n^N} \int_{x \leq \xi} \exp \left[-NG_\beta \left(m + \frac{x}{N^\gamma} \right) \right] dx. \end{aligned} \quad (6.4.9)$$

The last step follows from changing variable $u = xN^{1-\gamma} + mN$. The lemma follows from obtaining the normalization factor $Z_N(\beta)$ by taking ξ to $(+\infty, +\infty, \dots, +\infty)$. \square

Lemma 6.4.5. For $\beta > 0$, let $\bar{G}_\beta = \min_{u \in \mathbb{R}^n} G_\beta(u)$, and let $V \subset \mathbb{R}^n$ be a Borel set containing no global minimum points of $G_\beta(u)$. For any vector $t \in \mathbb{R}^n$ there exists an ϵ such that

$$e^{N\bar{G}_\beta} \int_V e^{-NG_\beta(u) + \sqrt{N}\langle t, u \rangle} du \leq Ce^{-N\epsilon}, \text{ as } N \rightarrow +\infty,$$

with C a constant independent of N and V .

Proof. There exists an positive α such that $G_\beta(u \in V) \geq \bar{G}_\beta + \alpha$. From Lemma 6.4.1, we have

$$NG_\beta(u) - \sqrt{N}\langle t, u \rangle \geq \frac{1}{5}u^2, \text{ as } \|u\| \geq M,$$

for large enough M . Thus, we have

$$\begin{aligned} & e^{N\bar{G}_\beta} \int_V e^{-NG_\beta(u) + \sqrt{N}\langle t, u \rangle} du \\ &= e^{N\bar{G}_\beta} \int_{V \cap \{\|u\| \geq M\}} e^{-NG_\beta(u) + \sqrt{N}\langle t, u \rangle} du + e^{N\bar{G}_\beta} \int_{V \cap \{\|u\| < M\}} e^{-NG_\beta(u) + \sqrt{N}\langle t, u \rangle} du \\ &\leq e^{N\bar{G}_\beta} \int_{V \cap \{\|u\| \geq M\}} e^{-u^2/5} du + e^{-N\alpha} e^{\sqrt{N}M\|t\|} \int_{V \cap \{\|u\| < M\}} du. \end{aligned}$$

The lemma follows since $\bar{G}_\beta \leq G_\beta[u = (0, 0, \dots, 0)] = -\ln n < 0$. \square

Lemma 6.4.6. *Let \bar{v} be a global minimum point of $G_\beta(u)$, and $B(\bar{v}, b)$ denote a ball centered at \bar{v} with radius b . There exists a positive b such that for any bounded continuous function $f(u) : \mathbb{R}^n \rightarrow \mathbb{R}$,*

$$\begin{aligned} & \lim_{N \rightarrow \infty} e^{-\sqrt{N}\langle t, v \rangle} N^{n/2} e^{N\bar{G}_\beta} \int_{B(\bar{v}, b)} f(u) e^{-NG_\beta(u) + \sqrt{N}\langle t, u \rangle} \mathrm{d}u \\ &= f(\bar{v}) \int_{\mathbb{R}^n} \exp\left\{-\frac{1}{2}\langle x, D^2 G_\beta(\bar{v})x \rangle + \langle t, x \rangle\right\} \mathrm{d}x \end{aligned}$$

Proof.

$$\begin{aligned} & \lim_{N \rightarrow \infty} e^{-\sqrt{N}\langle t, \bar{v} \rangle} N^{n/2} e^{N\bar{G}_\beta} \int_{B(\bar{v}, b)} f(u) e^{-NG_\beta(u) + \sqrt{N}\langle t, u \rangle} \mathrm{d}u \\ &= \lim_{N \rightarrow \infty} e^{N\bar{G}_\beta} \int_{B(0, b\sqrt{N})} f(\bar{v} + x/\sqrt{N}) \exp\left\{-N \left[G_\beta(\bar{v} + x/\sqrt{N})\right] + \langle t, x \rangle\right\} \mathrm{d}x \\ &= f(\bar{v}) \lim_{N \rightarrow \infty} \int_{B(0, b\sqrt{N})} \exp\left\{-\frac{1}{2}\langle x, D^2 G_\beta(\bar{v})x \rangle + \langle t, x \rangle\right\} \mathrm{d}x \\ &= f(\bar{v}) \int_{\mathbb{R}^n} \exp\left\{-\frac{1}{2}\langle x, D^2 G_\beta(\bar{v})x \rangle + \langle t, x \rangle\right\} \mathrm{d}x. \end{aligned} \tag{6.4.10}$$

The first step follows by replacing $u = \bar{v} + x/\sqrt{N}$. The last step follows by doing Taylor expansions of $G_\beta(u)$ and using that $G'(\bar{v}) = 0$. \square

6.5 The general face-cubic model

6.5.1 Model

The Hamiltonian of the general face-cubic model on the complete graph is introduced in Eq. (6.1.2). There are a number of special cases where the general face-cubic model can be reduced to more familiar models.

- $J_1 = 0$, the n -state Curie-Weiss-Potts model.

- $J_2 = 0$, the standard face-cubic model.
- $J_1 = J_2$, the $2n$ -state Curie-Weiss-Potts model.
- $n = 1$, the Curie-Weiss model.
- $n = 2$, the Ashkin-Teller model by redefining $\omega_\alpha = \frac{1}{2}(\sigma_\alpha + \tau_\alpha, \sigma_\alpha - \tau_\alpha)$ with $\sigma_\alpha, \tau_\alpha \in \{-1, 1\}$, see Eq. (6.1.3).

We can rewrite the Hamiltonian Eq. (6.1.2) as follows,

$$H(\omega) = -\frac{J_1}{2N} \sum_{i=1}^n (N_i^+ - N_i^-)^2 - \frac{J_2}{2N} \sum_{i=1}^n (N_i^+ + N_i^-)^2, \quad \omega \in \Sigma^N.$$

Here N_i^+ and N_i^- are respectively the number of spins of the following two states on the configuration ω : the i -th entry is 1 and the i -th entry is -1 . To determine the Hamiltonian, one has to know exactly N_i^+ and N_i^- . This implies that S_N , the magnetization, is not enough to determine the Hamiltonian. We need a $2n$ dimensional vector which explicitly gives N_i^+ and N_i^- . A natural choice is the empirical vector L , with $L_i = N_i^+/N$ and $L_{i+n} = N_i^-/N$. Now we can rewrite the Hamiltonian as $H(\omega) = \tilde{H}(L(\omega))$, where $\tilde{H} : \Delta \rightarrow \mathbb{R}$ is an energy representation function for L . Here Δ denotes the $(2n - 1)$ -dimensional simplex. Precisely,

$$\tilde{H}(v) = -\frac{NJ_1}{2} \sum_{i=1}^n (v_i - v_{i+n})^2 - \frac{NJ_2}{2} \sum_{i=1}^n (v_i + v_{i+n})^2, \quad v \in \Delta.$$

A standard large deviation analysis (see Theorem 2.4 in Ref. (Ellis *et al.*, 2000)) yields the rate function for the distribution of the empirical vector, that is

$$I_0(J_1, J_2, v) = I(J_1, J_2, v) - \min_{v \in \Delta} I(J_1, J_2, v), \quad v \in \Delta, \quad (6.5.1)$$

with $I(J_1, J_2, v)$ defined as

$$\begin{aligned}
 I(J_1, J_2, v) = & -\frac{J_1}{2} \sum_{i=1}^n (v_i - v_{i+n})^2 - \frac{J_2}{2} \sum_{i=1}^n (v_i + v_{i+n})^2 \\
 & + \sum_{i=1}^{2n} v_i \log v_i, \quad v \in \Delta.
 \end{aligned} \tag{6.5.2}$$

Here we have taken $\beta = 1$. Compared with Eq. (6.2.4), we neglect the constant $\log(2n)$ since any constants in $I(J_1, J_2, v)$ will be subtracted in Eq. (6.5.1). In addition, we note from the definition that the rate function $I_0(J_1, J_2, v) = 0$ when $I(J_1, J_2, v)$ attains its global minimums. Therefore, the main task in the next sections is to study how the global minimum points of $I(J_1, J_2, v)$ change with respect to J_1 and J_2 , which reveals the phase transitions. Without confusion, we call $I(J_1, J_2, v)$ the rate function in the discussions below.

6.5.2 Useful definitions

We now introduce some useful notation and definitions.

Definition 6.5.1. Let $c > 0$ and define $\Delta(c) \subset \mathbb{R}^{2n}$ such that a vector $v \in \Delta(c)$ iff it satisfies $v_i \geq 0$ for all $1 \leq i \leq 2n$ and $\sum_{i=1}^{2n} v_i = c$.

Definition 6.5.2. Let $\Omega(c) \subset \Delta(c)$. A vector $v \in \Omega(c)$ iff

$$(i) \quad v_1 = \max\{v_i, 1 \leq i \leq 2n\};$$

$$(ii) \quad v_i \geq v_{i+n} \text{ for all } 1 \leq i \leq n.$$

For $c = 1$, we denote $\Delta(1) = \Delta$ and $\Omega(1) = \Omega$.

For $v \in \Delta$, since $\sum_{i=1}^{2n} v_i \log v_i$ is bounded, the function $I(J_1, J_2, v)$ must have at least one global minimum points in Δ . Moreover, the symmetry of $I(J_1, J_2, v)$ guarantees that there must be at least one global minimum points in Ω . We also note that, at

the critical point of a first order transition, the number of global minimum points in Ω is more than one. Unless stated otherwise, the probability vectors we discuss below belong to Ω .

Definition 6.5.3. (i) Let $x > 0$, $J_1 \in \mathbb{R}$ and a real function $g(J_1, x) := \log x - 2J_1 x$. The function $s(J_1, x)$ is defined as

$$s(J_1, x) := \min_{y>0} \{y : g(J_1, y) = g(J_1, x)\}. \quad (6.5.3)$$

(ii) Let $x > 0$ and $J_1, J_2 \in \mathbb{R}$, define a function

$$F(J_1, J_2, x) = \log x + \log s(J_1, x) - 2J_2 [x + s(J_1, x)]. \quad (6.5.4)$$

If $J_1 < 0$, then $g(J_1, x)$ is monotonically increasing and thus $s(J_1, x) = x$. For $J_1 > 0$, it can be easily shown that $g(J_1, x)$ increases on $(0, 1/(2J_1)]$ and decreases on $[1/(2J_1), +\infty)$. This directly implies that $s(J_1, x) = x$ if $x \leq 1/(2J_1)$, and $s(J_1, x) < x$ if $x > 1/(2J_1)$. The function $s(J_1, x)$ is introduced to describe the constraints on v_i and v_{i+n} if v is a global minimum point, that is $v_{i+n} = s(J_1, v_i)$ (see Lemma. 6.5.12). Similarly, the function $F(J_1, J_2, x)$ is defined to describe the constraints on v_i and v_j if v is a global minimum point, with details shown in Lemma. 6.5.12. Differentiating the equality $\log x - 2J_1 x = \log s(J_1, x) - 2J_1 s(J_1, x)$ with respect to x yields

$$s'(J_1, x) = \frac{1/x - 2J_1}{1/s(J_1, x) - 2J_1}. \quad (6.5.5)$$

Definition 6.5.4. (i) Define $\Gamma \subset \Omega$ such that $v \in \Gamma$ iff there exists $J_1 \in \mathbb{R}$ for which $v_{i+n} = s(J_1, v_i)$ for all $1 \leq i \leq n$.

(ii) Define $\Omega_m(J_1, J_2) \subset \Omega$ as the set of global minimum points of $I(J_1, J_2, v)$.

Lemma. 6.5.12 (ii) shows that for any J_1, J_2 , if $v \in \Omega$ is a global minimum point of the rate function, then $v \in \Gamma$. Thus, we have $\Omega_m(J_1, J_2) \subset \Gamma$.

Definition 6.5.5. *We define a number of distinguished subsets of Γ as follows.*

- (i) *The constant vector $(1/(2n), 1/(2n), \dots, 1/(2n))$ is called the disordered vector, and denoted v_0 .*
- (ii) *A vector $v \in \Gamma$ is called an Ising vector if $v_i = a$ and $v_{i+n} = b$ for all $1 \leq i \leq n$ with $a > b$. The set of all Ising vectors is called the Ising set, denoted Ω_I .*
- (iii) *A vector $v \in \Gamma$ is called a Potts vector if $v_1 = a$ and $v_i = b$ for all $2 \leq i \leq n$, with $a > b$, and $v_{i+n} = v_i$ for all $1 \leq i \leq n$. The set of all Potts vectors is called the Potts set, denoted Ω_P .*
- (iv) *A vector $v \in \Gamma$ is called a super-ordered vector if there exists $J_1 > 0$ such that $v_1 = a$ and $v_i = b$ for all $2 \leq i \leq n$, with $1/(2J_1) < b < a$; and $v_{i+n} = s(J_1, v_i)$ for all $1 \leq i \leq n$. The set of all super-ordered vectors is called the super-ordered set, denoted Ω_{SO} .*
- (v) *A vector $v \in \Gamma$ is called a face-cubic vector if there exists $J_1 > 0$ such that $v_1 = a$ and $v_i = b$ for all $2 \leq i \leq n$, with $b \leq 1/(2J_1) < a$; and $v_{i+n} = s(J_1, v_i)$ for all $1 \leq i \leq n$. The set of all face-cubic vectors is called the face-cubic set, denoted Ω_{FC} .*

Recall that $\Omega_m(J_1, J_2)$ is the set of global minimum points of $I(J_1, J_2, v)$. We respectively say the general face-cubic model is in the disordered, Ising, Potts, super-ordered, or face-cubic phase if $\Omega_m(J_1, J_2)$ is a subset of the set $\{v_0\}$, Ω_I , Ω_P , Ω_{SO} , or Ω_{FC} . To better understand these phases, we can describe the states of the face-cubic model in terms of colors and spins. The $2n$ vectors in the state space can be partitioned into n colors. A state is in color i if the i -th entry is non-zero. In each color, a state is respectively called spin up or down if the non-zero entry is 1 or -1 . Taking $n = 2$ for example, the state $(1, 0)$ is in color 1 and spin up, and $(-1, 0)$ is in color 1 and spin down. We can now interpret the various phases in terms of

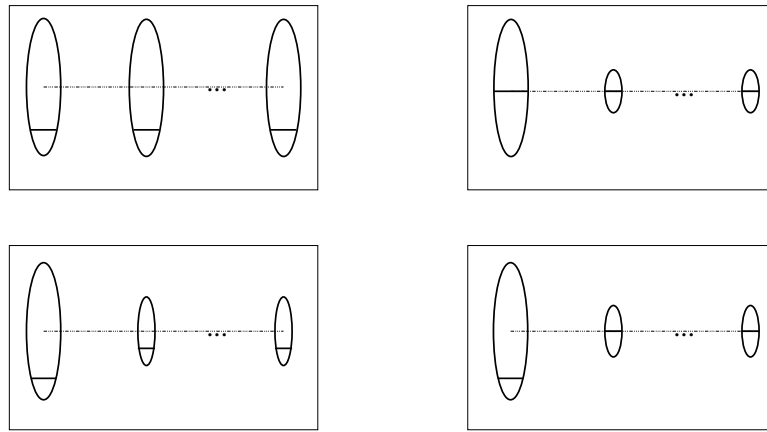


Figure 6.3: Illustration of an Ising vector (top left), Potts vector (top right), super-ordered vector (bottom left), and face-cubic vector (bottom right). In each figure, the size of each ellipse represents the fractional occupation of the corresponding color, while the regions above and below the bar respectively represent spin up and down.

the ordering of colors and spins. The disordered phase corresponds to both color and spin disorder. The Ising phase is spin ordered but color disordered. The Potts phase is ordered in color but not in spin. The face-cubic phase is more subtle. The color is ordered, but spin is ordered in the dominant color but disordered in others. The super-ordered phase is both spin and color ordered. These ordered phases are illustrated in Fig. 6.3 by ellipses. In each figure, we use n ellipses to denote the fractional occupations of n colors. In each ellipse, a bar is used to separate the occupations of spin up and down.

6.5.3 Phase diagram

We present in Theorem 6.5.6 the phase diagram of the general n -component face-cubic model with $n = 2$ on the (J_1, J_2) plane. The structure of the phase diagram for $n = 2$ is shown in Fig. 6.4 to help interpreting the theorem.

Theorem 6.5.6. *On the complete graph, the phase diagram of the n -component general face-cubic model with $n = 2$ on the (J_1, J_2) plane is separated into two infinite half plane by a curve C . The values of J_1 on C satisfy $1 < J_1 \leq n$. Furthermore $J_1 = n$ for all $J_2 \leq 0$.*

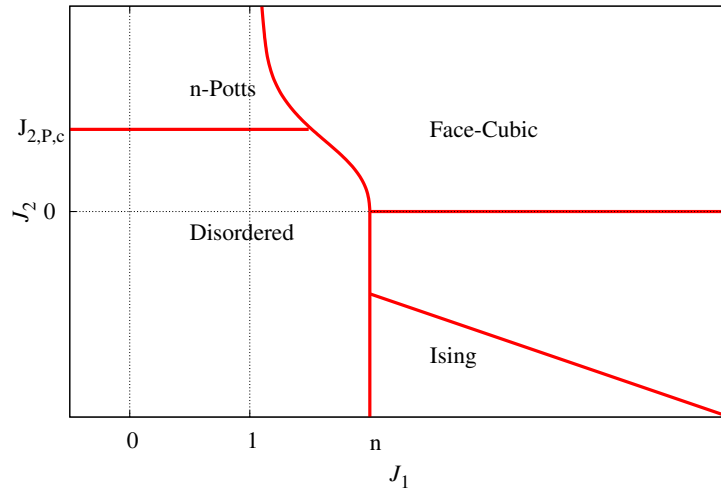


Figure 6.4: Phase diagram for the general n -component face-cubic model on the complete graph with $n = 2$. The phase diagram is rigorous except the region $-J_1 < J_2 < 0$ when $J_1 > 2$.

On the left infinite plane, a line $J_2 = n$ separates the disordered phase and the n -state Potts phase. On the right infinite plane, the system is in the face-cubic phase for $J_2 \geq 0$, and in the Ising phase for $J_2 \leq -J_1$.

Proof. Recall that phases of the general face-cubic model on the complete graph are determined by the global minimum points of the rate function $I(J_1, J_2, v)$. Proposition 6.5.7 states that the minimum of $I(J_1, J_2, v)$ is a continuous function of J_1 and J_2 .

We first prove that for $n = 2$, there are at most five phases on the phase diagram. Let $\bar{v} \in \Omega_m(J_1, J_2)$ (defined in Def. 6.5.4), Lemma 6.5.12 with $c = 1$ implies that $\bar{v}_{i+n} = s(J_1, \bar{v}_i)$ for $i = 1, 2$. When $J_1 \leq 0$, the function $g(J_1, x)$ (see Def. 6.5.3) is monotonically increasing and thus we have $\bar{v}_{i+n} = \bar{v}_i$. This corresponds to either the Potts or disordered phase. We next discuss the $J_1 > 0$ case, where $\bar{v}_{i+n} = \bar{v}_i$ if $\bar{v}_i \leq 1/(2J_1)$ and $\bar{v}_{i+n} < \bar{v}_i$ if $\bar{v}_i > 1/(2J_1)$. For $n = 2$, if $\bar{v}_1 \leq 1/(2J_1)$, then $\bar{v}_3 = \bar{v}_1$ and $\bar{v}_2 = \bar{v}_4$, which implies that the system is either in the Potts phase or disordered phase. If $\bar{v}_1 > 1/(2J_1)$, the cases $\bar{v}_2 \leq 1/(2J_1) < \bar{v}_1$, $1/(2J_1) < \bar{v}_2 < \bar{v}_1$, and $\bar{v}_2 = \bar{v}_1$

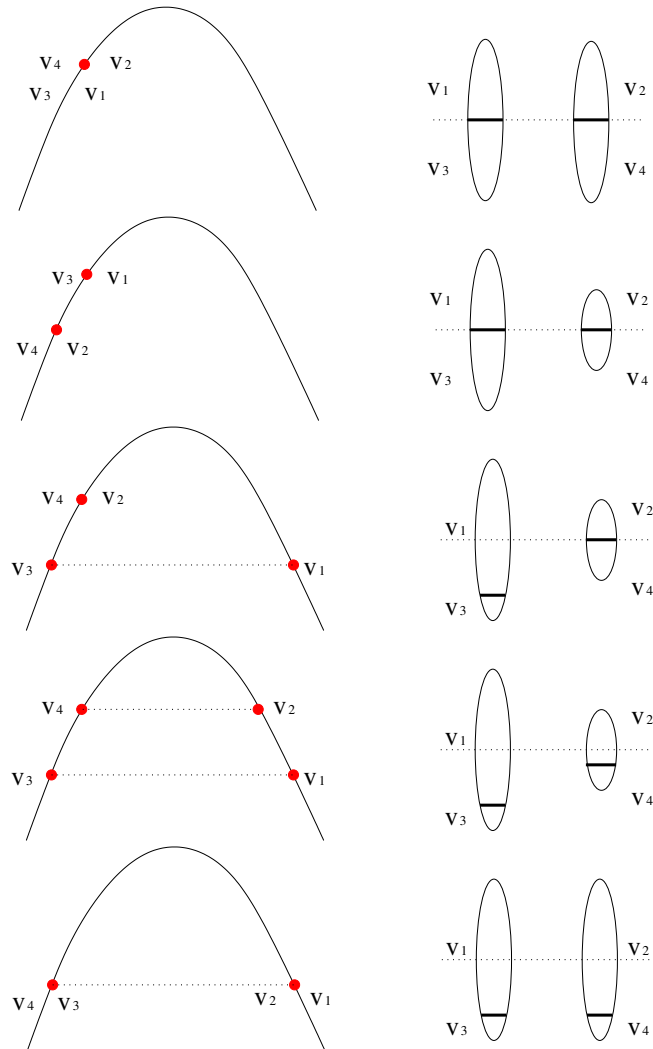


Figure 6.5: Illustration of five phases by means of the function $g(J_1, x)$ and ellipse diagrams. From top to bottom, they respectively denote the disordered, Potts, face-cubic, super-ordered, and Ising phases. The curves on the left plot the function $g(J_1, x) = \log x - 2J_1 x$. On the right, we use ellipses to represent the fractional occupation of colors and in each ellipse, a bar is used to distinguish spin up and down. One can see both spin and color disorder in the disordered phase, color order but spin disorder in the Potts phase, color disorder but spin order in the Ising phase. In the face-cubic phase, color is ordered and spin is ordered in the dominant color but disordered in the other. In the super-ordered phase, both color and spin are ordered.

respectively corresponds to the face-cubic phase, the super-ordered phase, and the Ising phase. We illustrate these five phases in Fig. 6.5.

We now separate our discussions into three regions on the (J_1, J_2) plane: $J_1 \leq 1$, $J_2 \leq -J_1 \leq 0$, and $J_2 \geq 0$. We note that the proofs for the first two regions also hold for $n \geq 3$.

Region $J_1 \leq 1$. For $J_1 \leq 1$, part (i) in Proposition 6.5.8 gives that $\Omega_m(J_1, J_2) \subset \Omega_p \cup \{v_0\}$. This means if \bar{v} is a global minimum point, then $\bar{v}_{i+n} = \bar{v}_i$ for all $1 \leq i \leq n$. Therefore, finding the minimum of $I(J_1, J_2, v)$ is reduced to find the minimum of the following function

$$-\frac{J_2}{2} \sum_{i=1}^n (2\bar{v}_i)^2 + \sum_{i=1}^n (2\bar{v}_i) \log(2\bar{v}_i) - \log 2,$$

which is independent of J_1 . This is exactly the rate function of the n -state Curie-Weiss-Potts model (Ellis and Wang, 1990), if we define $\bar{v}'_i = 2\bar{v}_i$ and neglect the constant $\log 2$. The transition is continuous for $n = 2$ and of first order for $n \geq 3$, and the critical value $J_{2,P,c} = n$ for $n = 2$ and $J_{2,P,c} = 2(n-1)\log(n-1)/(n-2)$ for $n \geq 3$.

Region $J_2 \leq -J_1 \leq 0$. Part (iii) in Lemma 6.5.12 with $c = 1$ tells that $F(J_1, J_2, \bar{v}_i) = F(J_1, J_2, \bar{v}_j)$ for all $1 \leq i, j \leq n$, if \bar{v} is a global minimum point. Part (iii) in Proposition 6.5.11 shows the function $F(J_1, J_2, x)$ is monotonic in this region, thus we have $\bar{v}_i = \bar{v}_j$ for all $1 \leq i, j \leq n$. From part (ii) in Lemma 6.5.12, we know $\bar{v}_{i+n} = s(J_1, \bar{v}_i)$, thus $\bar{v}_{i+n} = \bar{v}_{j+n}$ for all $1 \leq i, j \leq n$. Let $\bar{v}_i = x$ and $\bar{v}_{i+n} = 1/n - x$ for all $1 \leq i \leq n$ with $x \in [1/(2n), 1/n]$, then the minimum of $I(J_1, J_2, v)$ is equal to the minimum of the following function,

$$\begin{aligned} & -\frac{J_1}{2n} (2nx - 1)^2 + nx \log(nx) + (1 - nx) \log(1 - nx) \\ = & -\frac{J_1'}{2} (x_1 - x_2)^2 + x_1 \log x_1 + x_2 \log x_2 - \frac{J_2}{2n} - \log n. \end{aligned}$$

Here we let $x_1 = nx$, $x_2 = 1 - nx$, and $J'_1 = J_1/n$. Ignoring the unimportant constant $\left(-\frac{J_2}{2n} - \log n\right)$, we notice that this is exactly the rate function for the Curie-Weiss model (Eisele and Ellis, 1983), where a continuous phase transition happens at $J'_1 = 1$ (or equivalently at $J_1 = n$) for all $n \geq 2$.

Region $J_2 \geq 0$. We prove this region only for $n = 2$. Difficulties for $n \geq 3$ in this region are discussed in the Discussion. We already know that for $J_1 \leq 1$, the line $J_2 = J_{2,P,c}$ separates the Potts phase and the disordered phase. In addition, part (ii) in Proposition 6.5.8 states that the system cannot be disordered or in the Potts phase when $J_1 > n$. In other words, the region $J_1 > n$ contains some other ordered phases. From the monotonic properties of Potts and disordered phases (see Proposition 6.5.10), we know there must be a boundary in the region $1 < J_1 \leq n$ separating the Potts and disordered phases on the left with some other ordered phases on the right. We denote this boundary as the curve C . Their monotonic properties also imply that the line $J_2 = J_{2,P,c}$ extends to C . Moreover for $n = 2$ and 3, since $J_1 = n$ is the critical point of the standard face-cubic model ($J_2 = 0$), a vertical line $J_1 = n$ is a boundary between the disordered phase and the ordered phase for all $J_2 \leq 0$.

We then discuss the right of C for $J_2 \geq 0$. We separate our discussions into two parts, $J_1 \leq 2$ and $J_1 > 2$. If $J_1 \leq 2$, the right of C is face-cubic ordered since part (iii) of Proposition 6.5.8 implies that the Ising and super-ordered phases cannot exist in this region. We then discuss the region where $J_1 > 2$ and $J_2 \geq 0$. When $J_1 > 2$ and $J_2 = 0$, the system is in the face-cubic phase, as indicated in Theorem 6.3.1. Proposition 6.5.9 says that if $\Omega_m(J_1, J_2) \subset \Omega_{FC}$, then $\Omega_m(J_1, J_2 + \epsilon) \subset \Omega_{FC}$ for any $\epsilon > 0$. So, to the right of C and $J_2 \geq 0$, the system is in the face-cubic phase. \square

6.5.4 Preliminary knowledge needed to prove the phase diagram

Define $M(J_1, J_2) = \inf_{\nu \in \Omega} I(J_1, J_2, \nu)$, the next lemma proves the continuity of $M(J_1, J_2)$ on the (J_1, J_2) plane.

Proposition 6.5.7. *Define $M : \mathbb{R}^2 \rightarrow \mathbb{R}$ via $M(J_1, J_2) = \inf_{\nu \in \Omega} I(J_1, J_2, \nu)$. Then M is continuous.*

Proof. Note that $I(J_1, J_2, \nu)$ is well-defined for all $J_1, J_2 \in \mathbb{R}$ and $\nu \in \Omega$. We need to prove that for any $x_0, y_0 \in \mathbb{R}$

$$\lim_{\|(x,y)-(x_0,y_0)\| \rightarrow 0} M(x,y) = M(x_0,y_0). \quad (6.5.6)$$

If μ is a vector such that $M(x_0, y_0) = I(x_0, y_0, \mu)$, then

$$M(x,y) \leq I(x,y,\mu) = M(x_0,y_0) - \frac{x-x_0}{2} \sum_{i=1}^n (\mu_i - \mu_{i+n})^2 - \frac{y-y_0}{2} \sum_{i=1}^n (\mu_i + \mu_{i+n})^2.$$

Similarly, if ν is a vector such that $M(x,y) = I(x,y,\nu)$, then

$$\begin{aligned} M(x,y) = I(x,y,\nu) &= I(x_0,y_0,\nu) - \frac{x-x_0}{2} \sum_{i=1}^n (\nu_i - \nu_{i+n})^2 - \frac{y-y_0}{2} \sum_{i=1}^n (\nu_i + \nu_{i+n})^2 \\ &\geq I(x_0,y_0,\mu) - \frac{x-x_0}{2} \sum_{i=1}^n (\nu_i - \nu_{i+n})^2 - \frac{y-y_0}{2} \sum_{i=1}^n (\nu_i + \nu_{i+n})^2 \\ &= M(x_0,y_0) - \frac{x-x_0}{2} \sum_{i=1}^n (\nu_i - \nu_{i+n})^2 - \frac{y-y_0}{2} \sum_{i=1}^n (\nu_i + \nu_{i+n})^2. \end{aligned}$$

We have therefore shown that $M(x,y) - M(x_0,y_0)$ is bounded both above and below by quantities which tend to 0 as $\|(x,y) - (x_0,y_0)\| \rightarrow 0$. It follows that Eq. (6.5.6) is valid for any $(x_0,y_0) \in \mathbb{R}^2$, so M is continuous. □

The next proposition gives bounds for the locations of the disordered, Potts, Ising, and super-ordered phases.

Proposition 6.5.8. *Let $\bar{v} \in \Omega_m(J_1, J_2)$.*

(i) *For $J_1 \leq 1$, $\bar{v} \in \Omega_P \cup \{\nu_0\}$.*

(ii) *For $J_1 > n$, $\bar{v} \notin \Omega_P \cup \{\nu_0\}$.*

(iii) *For $J_1 \leq n$, $\bar{v} \notin \Omega_I \cup \Omega_{SO}$.*

Proof. Recall that $\Omega_m(J_1, J_2)$ is defined in Def. 6.5.4. For part (i), we consider $J_1 \leq 0$ and $0 < J_1 \leq 1$ separately. If $J_1 \leq 0$, then $g(J_1, x)$ (defined in Def. 6.5.3) is monotonically increasing. Lemma 6.5.12 (ii) with $c = 1$ implies that $\bar{v}_{i+n} = s(J_1, \bar{v}_i) = \bar{v}_i$ for every $1 \leq i \leq n$. We then consider the $0 < J_1 \leq 1$ case. Part (ii) in Lemma 6.5.13 says that $x + s(J_1, x)$ is an increasing function of x in the region $[1/(2J_1), +\infty)$. Therefore, if $\bar{v}_i > 1/(2J_1)$, then $\bar{v}_i + s(J_1, \bar{v}_i) > 1/(2J_1) + s(J_1, 1/(2J_1)) = 1/J_1 > 1$. The facts that $\bar{v}_{i+n} = s(J_1, \bar{v}_i)$ (from part (ii) in Lemma 6.5.12 with $c = 1$) and $s(J_1, 1/(2J_1)) = 1/(2J_1)$ are used. So, for $0 < J_1 \leq 1$, we again have $\bar{v}_i \leq 1/(2J_1)$ for all $1 \leq i \leq n$, which further indicates that $\bar{v}_{i+n} = s(J_1, \bar{v}_i) = \bar{v}_i$. Part (i) then follows, recalling the definition of Ω_P and ν_0 in Def. 6.5.5.

For part (ii), recall that \bar{v}_1 is the largest entry of \bar{v} (see Def. 6.5.2). Therefore, if $J_1 > n$, then $\bar{v}_1 \geq 1/(2n) > 1/(2J_1)$, and so $s(J_1, \bar{v}_1) < \bar{v}_1$. Lemma 6.5.12 (ii) with $c = 1$ then shows $\bar{v}_{1+n} = s(J_1, \bar{v}_1) < \bar{v}_1$, which implies $\bar{v} \notin \Omega_P \cup \{\nu_0\}$.

For part (iii), suppose $J_1 < n$. If $\bar{v} \in \Omega_I \cup \Omega_{SO}$, then $\bar{v}_{i+n} < \bar{v}_i$ for all $1 \leq i \leq n$, which implies $\bar{v}_i > 1/(2J_1)$ for all $1 \leq i \leq n$. Therefore, Lemma 6.5.13 (ii) shows

$$\bar{v}_i + s(J_1, \bar{v}_i) > \frac{1}{2J_1} + s\left(J_1, \frac{1}{2J_1}\right) = \frac{1}{J_1}.$$

So Lemma 6.5.12 (ii) with $c = 1$ implies $\bar{v}_i + \bar{v}_{i+n} > 1/J_1$, which means $\sum_{i=1}^n (\bar{v}_i + \bar{v}_{i+n}) > n/J_1 > 1$. So $\bar{v} \notin \Omega_I \cup \Omega_{SO}$. \square

Proposition 6.5.9. *Let $n = 2$. If $\Omega_m(J_1, J_2) \subset \Omega_{FC}$, then $\Omega_m(J_1, J_2 + \epsilon) \subset \Omega_{FC}$ for any $\epsilon > 0$.*

Proof. Recall that $\Omega_m(J_1, J_2)$ is defined in Def. 6.5.4. For $\epsilon > 0$ and $v \in \Omega$,

$$I(J_1, J_2 + \epsilon, v) = I(J_1, J_2, v) - \frac{\epsilon}{2} \sum_{i=1}^2 (v_i + v_{i+2})^2.$$

Let $v \in \Omega_m(J_1, J_2)$. If $\Omega_m(J_1, J_2) \subset \Omega_{FC}$, then $\bar{v}_1 > 1/(2J_1) > \bar{v}_3$ and $\bar{v}_2 = \bar{v}_4 \leq 1/(2J_1)$.

Let $\mu \in \Omega$ satisfy that $\mu_3 = s(J_1, \mu_1)$ and $\mu_4 = s(J_1, \mu_2)$. Suppose $\mu_1 < \bar{v}_1$. Proposition 6.5.13 (ii) says that $f(x) = x + s(J_1, x)$ is an increasing function for all $x > 0$, so

$$\begin{aligned} \mu_1 + \mu_3 &= \mu_1 + s(J_1, \mu_1) < \bar{v}_1 + s(J_1, \bar{v}_1) = \bar{v}_1 + \bar{v}_3, \\ \mu_1 + \mu_3 &= \mu_1 + s(J_1, \mu_1) > \mu_2 + s(J_1, \mu_2) = \mu_2 + \mu_4. \end{aligned}$$

We also have $\mu_2 + \mu_4 > \bar{v}_2 + \bar{v}_4$ since $\sum_{i=1}^4 \mu_i = \sum_{i=1}^4 \bar{v}_i$. Therefore,

$$\bar{v}_2 + \bar{v}_4 < \mu_2 + \mu_4 < \mu_1 + \mu_3 < \bar{v}_1 + \bar{v}_3. \quad (6.5.7)$$

A straightforward optimization analysis gives

$$(\bar{v}_2 + \bar{v}_4)^2 + (\bar{v}_1 + \bar{v}_3)^2 > (\mu_2 + \mu_4)^2 + (\mu_1 + \mu_3)^2.$$

From Eq. (6.5.7),

$$I(J_1, J_2 + \epsilon, \bar{v}) = I(J_1, J_2, \bar{v}) - \frac{\epsilon}{2} \sum_{i=1}^2 (\bar{v}_i + \bar{v}_{i+2})^2$$

$$\begin{aligned}
 &< I(J_1, J_2, \mu) - \frac{\epsilon}{2} \sum_{i=1}^2 (\bar{v}_i + \bar{v}_{i+2})^2 \\
 &< I(J_1, J_2, \mu) - \frac{\epsilon}{2} \sum_{i=1}^2 (\mu_i + \mu_{i+2})^2 \\
 &= I(J_1, J_2 + \epsilon, \mu).
 \end{aligned}$$

So μ must not be a global minimum point of $I(J_1, J_2 + \epsilon, \nu)$ if $\mu_1 < \bar{v}_1$.

Let $\mu \in \Omega_m(J_1, J_2 + \epsilon)$. We now know $\mu_1 \geq \bar{v}_1 > 1/(2J_1)$, and so $\mu_3 = s(J_1, \mu_1) < 1/(2J_1)$.

Since $f(x)$ is increasing for all $x > 0$, we have

$$\mu_1 + \mu_3 = \mu_1 + s(J_1, \mu_1) \geq \bar{v}_1 + s(J_1, \bar{v}_1) = \bar{v}_1 + \bar{v}_3, \quad (6.5.8)$$

and so $\mu_2 + \mu_4 \leq \bar{v}_2 + \bar{v}_4$. Since $\bar{v}_2 = \bar{v}_4 \leq 1/(2J_1)$, we have $\mu_2 + \mu_4 = \mu_2 + s(J_1, \mu_2) \leq 1/J_1$. Again, since $f(x)$ is increasing and $f(1/(2J_1)) = 1/J_1$, we have $\mu_2 \leq 1/(2J_1)$ and so $\mu_4 = s(J_1, \mu_2) = \mu_2$. Therefore $\mu_1 > 1/(2J_1) > \mu_3$ and $\mu_2 = \mu_4$, implying $\mu \in \Omega_{FC}$. So $\Omega_m(J_1, J_2 + \epsilon) \in \Omega_{FC}$ for any $\epsilon > 0$. \square

The next proposition shows the monotonicity properties of the Ising, Potts and disordered phases.

Proposition 6.5.10. *Let $\epsilon > 0$.*

- (i) *If $\Omega_m(J_1, J_2) \subset \Omega_P$, then $\Omega_m(J_1 - \epsilon, J_2) \subset \Omega_P$.*
- (ii) *If $\Omega_m(J_1, J_2) \subset \Omega_I$, then $\Omega_m(J_1, J_2 - \epsilon) \subset \Omega_I$.*
- (iii) *If $\Omega_m(J_1, J_2) = \{\nu_0\}$, then $\Omega_m(J_1 - \epsilon, J_2) = \{\nu_0\}$.*
- (iv) *If $\Omega_m(J_1, J_2) = \{\nu_0\}$, then $\Omega_m(J_1, J_2 - \epsilon) = \{\nu_0\}$.*

Proof. We first prove part (i). Assume $\Omega_m(J_1, J_2) \subset \Omega_P$. Let $\bar{v} \in \Omega_m(J_1, J_2)$, then $\bar{v}_i = \bar{v}_{i+n}$ for all $1 \leq i \leq n$, and $\bar{v}_1 > \bar{v}_2 = \dots = \bar{v}_n$. For $\epsilon > 0$,

$$I(J_1 - \epsilon, J_2, v) = I(J_1, J_2, v) + (\epsilon/2) \sum_{i=1}^n (v_i - v_{i+n})^2, \quad v \in \Omega. \quad (6.5.9)$$

We observe that \bar{v} also minimize $I(J_1 - \epsilon, J_2, v)$, since \bar{v} minimizes $(\epsilon/2) \sum_{i=1}^n (v_i - v_{i+n})^2$. It further implies that $I(J_1 - \epsilon, J_2, \bar{v}) = I(J_1, J_2, \bar{v})$.

Let $\mu \in \Omega(J_1 - \epsilon, J_2)$. From Eq. (6.5.9), we have $I(J_1 - \epsilon, J_2, \mu) \geq I(J_1, J_2, \mu)$. Since \bar{v} is a minimizer of both $I(J_1, J_2, v)$ and $I(J_1 - \epsilon, J_2, v)$, we have

$$I(J_1 - \epsilon, J_2, \mu) \geq I(J_1, J_2, \mu) \geq I(J_1, J_2, \bar{v}) = I(J_1 - \epsilon, J_2, \bar{v}) = I(J_1 - \epsilon, J_2, \mu).$$

The first inequality becomes equality iff $\mu_i = \mu_{i+n}$ for all $1 \leq i \leq n$. The second inequality becomes equality iff $\mu \in \Omega_P$. So $\Omega_m(J_1 - \epsilon, J_2) \in \Omega_P$.

We now prove part (ii). Assume $\Omega_m(J_1, J_2) \subset \Omega_I$. Let \bar{v} be a minimizer of $I(J_1, J_2, v)$, then $\bar{v}_1 = \dots = \bar{v}_n > \bar{v}_{n+1} = \dots = \bar{v}_{2n}$, which further implies $\bar{v}_i + \bar{v}_{i+n} = 1/n$ for all $1 \leq i \leq n$. For $\epsilon > 0$,

$$I(J_1, J_2 - \epsilon, v) = I(J_1, J_2, v) + (\epsilon/2) \sum_{i=1}^n (v_i + v_{i+n})^2, \quad v \in \Omega. \quad (6.5.10)$$

We observe that \bar{v} also minimize $I(J_1, J_2 - \epsilon, v)$, since \bar{v} minimizes $(\epsilon/2) \sum_{i=1}^n (v_i + v_{i+n})^2$. It further implies that $I(J_1, J_2 - \epsilon, \bar{v}) = I(J_1, J_2, \bar{v})$.

Let μ be a minimizer of $I(J_1, J_2 - \epsilon, v)$. From Eq. (6.5.10), we have $I(J_1, J_2 - \epsilon, \mu) \geq I(J_1, J_2, \mu)$. Since \bar{v} is a minimizer of both $I(J_1, J_2, v)$ and $I(J_1, J_2 - \epsilon, v)$, we have

$$I(J_1, J_2 - \epsilon, \mu) \geq I(J_1, J_2, \mu) \geq I(J_1, J_2, \bar{v}) = I(J_1, J_2 - \epsilon, \bar{v}) = I(J_1, J_2 - \epsilon, \mu).$$

The first inequality becomes equality iff $\mu_i + \mu_{i+n} = 1/n$ for all $1 \leq i \leq n$. The second inequality becomes equality iff $\mu \in \Omega_I$. So $\Omega_m(J_1, J_2 - \epsilon) \in \Omega_I$.

The proof of part (iii) is similar to part (i), and the proof of part (iv) is similar to part (ii).

Proposition 6.5.11. *Let $J_1 > 0$ and $J_2 \in \mathbb{R}$.*

(i) *If $J_2 > 0$, then $F(J_1, J_2, x)$ increases in $(0, 1/(2J_{\min}))$ and decreases in $(1/(2J_{\min}), +\infty)$, with $J_{\min} = \max(J_1, J_2)$.*

(ii) *If $J_2 \leq -J_1 < 0$, then $F(J_1, J_2, x)$ is monotonically increasing in $(0, +\infty)$.*

Proof. Recall that $F(J_1, J_2, x)$ is defined in Def. 6.5.3. We use $F(x)$ for $F(J_1, J_2, x)$ for simplicity. Recall that, if $x \leq 1/(2J_1)$ then $s(J_1, x) = x$. In this case we have

$$F(x) = 2(\log x - 2J_2x) = 2g(J_2, x), \quad (6.5.11)$$

which is monotonically increasing for $J_2 \leq 0$ or for $J_2 > 0$ and $x \leq 1/(2J_2)$.

We first prove part (i). From Eq. (6.5.11), we see that $F(x) = 2g(J_2, x)$ in the region $(0, 1/(2J_1))$. If $J_2 > J_1$, then $F(x)$ increases in $(0, 1/(2J_2)]$ and decreases in $[1/(2J_2), 1/(2J_1))$. If $J_2 < J_1$, then $F(x)$ increases in $(0, 1/(2J_1)]$. The function $F(x)$ is monotonically decreasing in $[1/(2J_1), +\infty)$ because both $\log(xs(J_1, x))$ and $-2J_2(x + s(J_1, x))$ are decreasing functions, see Lemma 6.5.13.

We then prove part (ii). Again $F(x) = 2g(J_2, x)$ in the region $(0, 1/(2J_1)]$. If $J_2 \leq 0$, then $F(x)$ is monotonically increasing in $(0, 1/(2J_1)]$. We next study $F(x)$ in the region $[1/(2J_1), +\infty)$ with $J_2 = -J_1 < 0$. The first derivative is

$$\begin{aligned} F'(x) &= \frac{1}{x} + \frac{s'(J_1, x)}{s(J_1, x)} - 2J_2(1 + s'(J_1, x)) \\ &= \frac{2}{x(1 - 2J_1s(J_1, x))} [1 - (J_1 + J_2)(x + s(J_1, x)) + 4J_1J_2xs(J_1, x)] \end{aligned}$$

$$= \frac{2}{x(1 - 2J_1 s(J_1, x))} \left[1 - 4J_1^2 x s(J_1, x) \right]. \quad (6.5.12)$$

From Lemma 6.5.13 (iii), we see that $x s(J_1, x) > \frac{1}{2J_1} s(J_1, 1/(2J_1)) = 1/(4J_1^2)$, which yields $F'(x) < 0$. If $J_2 < -J_1 < 0$, we can write $J_2 = -J_1 - \epsilon$ with $\epsilon > 0$, then

$$F'(x) = \frac{2}{x(1 - 2J_1 s(J_1, x))} \left[1 - 4J_1^2 x s(J_1, x) + \epsilon(x + s(J_1, x) - 4J_1 x s(J_1, x)) \right].$$

From Lemma 6.5.13 (ii) and (iii), we see that $x + s(J_1, x)$ is increasing whilst $x s(J_1, x)$ is decreasing in $(1/(2J_1), +\infty)$. This implies that

$$x + s(J_1, x) - 4J_1 x s(J_1, x) > \frac{1}{2J_1} + s(J_1, 1/(2J_1)) - 4J_1 \frac{1}{2J_1} s(J_1, 1/(2J_1)) = 0.$$

So $F'(x) > 0$ in $(1/(2J_1), +\infty)$, when $J_2 \leq -J_1 < 0$. Therefore, if $J_2 \leq -J_1 < 0$ then $F(x)$ is monotonically increasing. \square

We next summarize the lemmas. Define the rate function $I(J_1, J_2, \nu)$ (see Eq. (6.5.2)) on $\Delta(c)$ (defined in Def. 6.5.1). We first propose a lemma showing that the global minimum points of $I(J_1, J_2, \nu)$ must live in the interior of $\Delta(c)$, and deriving necessary conditions for possible global minimum points.

Lemma 6.5.12. *Define the rate function $I(J_1, J_2, \nu)$ on $\Delta(c)$. Let $\bar{\nu} \in \Omega(c)$ be a global minimum point of $I(J_1, J_2, \nu)$, then the following statements hold.*

- (i) $\bar{\nu}$ is in the interior of $\Delta(c)$;
- (ii) $\bar{\nu}_{i+n} = s(J_1, \bar{\nu}_i)$ for all $1 \leq i \leq n$;
- (iii) $F(J_1, J_2, \bar{\nu}_i) = F(J_1, J_2, \bar{\nu}_j)$ for all $1 \leq i, j \leq n$.

Proof. Recall that the functions $s(J_1, x)$ and $F(J_1, J_2, x)$ are defined in Def. 6.5.3, and $\Omega(c) \subset \Delta(c)$ is defined in Def. 6.5.2. Write $I(J_1, J_2, \nu)$ as $I(\nu)$ for simplicity. We first

note that $I(\nu)$ is bounded in $\Delta(c)$. For $1 \leq i \leq n$, the partial derivatives are

$$\begin{aligned} I_i(\nu) &:= \left. \frac{\partial I(\nu)}{\partial \nu_i} \right|_{\nu=\nu} = -J_1(\nu_i - \nu_{i+n}) - J_2(\nu_i + \nu_{i+n}) + \log \nu_i + 1, \\ I_{i+n}(\nu) &:= \left. \frac{\partial I(\nu)}{\partial \nu_{i+n}} \right|_{\nu=\nu} = -J_1(\nu_{i+n} - \nu_i) - J_2(\nu_i + \nu_{i+n}) + \log \nu_{i+n} + 1. \end{aligned} \quad (6.5.13)$$

Let ν lie on the boundary of $\Delta(c)$, then there exists $1 \leq i, j \leq 2n$ such that $\nu_i = 0$ and $\nu_j > 0$. If we set $\nu'_i = \epsilon$, $\nu'_j = \nu_j - \epsilon$ with a sufficiently small $\epsilon > 0$, and $\nu'_k = \nu_k$ for $k \neq i, j$. The change of $I(\nu)$ is

$$\delta I = I(\bar{\nu}') - I(\bar{\nu}) = (I_i(\nu) - I_j(\nu))\epsilon + o(\epsilon). \quad (6.5.14)$$

Since $I_i(\nu) \rightarrow -\infty$ as $\nu_i \rightarrow 0^+$ but $I_j(\nu)$ is finite, one has $\delta I < 0$ which implies that ν cannot be a minimum. Part (i) then follows.

We then study part (ii). Let $\bar{\nu}$ be a global minimum point, then $\bar{\nu}$ is in the interior of $\Delta(c)$ from the above argument. Since $\bar{\nu} \in \Delta(c)$, from Eq. (6.5.14) we have $I_i(\bar{\nu}) = I_j(\bar{\nu})$ for all $1 \leq i, j \leq 2n$. Let $1 \leq i \leq n$ and $j = i + n$, we have from Eq. (6.5.13) that

$$\log \bar{\nu}_i - 2J_1 \bar{\nu}_i = \log \bar{\nu}_{i+n} - 2J_1 \bar{\nu}_{i+n}.$$

Define $g(J_1, x) = \log x - 2J_1 x$ for $J_1 \in \mathbb{R}$ and $x > 0$, then $g(J_1, \bar{\nu}_i) = g(J_1, \bar{\nu}_{i+n})$ for all $1 \leq i \leq n$. If $J_1 \leq 0$, then $g(J_1, x)$ is monotonically increasing and thus $\bar{\nu}_{i+n} = \bar{\nu}_i$. If $J_1 > 0$, then $g(J_1, x)$ increases in $(0, 1/(2J_1)]$ and decreases in $[1/(2J_1), +\infty)$. Since $\bar{\nu} \in \Omega$, we have $\bar{\nu}_{i+n} \leq \bar{\nu}_i$, and so if $\bar{\nu}_i \leq 1/(2J_1)$ then $\bar{\nu}_{i+n} \leq 1/(2J_1)$. Therefore, since $g(J_1, x)$ is monotonic for $x \leq 1/(2J_1)$, the constraint $g(J_1, \bar{\nu}_{i+n}) = g(J_1, \bar{\nu}_i)$ implies that $\bar{\nu}_{i+n} = \bar{\nu}_i = s(J_1, \bar{\nu}_i)$.

We next show by contradiction that if $\bar{v}_i > 1/(2J_1)$ then $\bar{v}_{i+n} < \bar{v}_i$. Let $\bar{v}'_i = \bar{v}_i + \epsilon$, $\bar{v}'_{i+n} = \bar{v}_{i+n} - \epsilon$, and $\bar{v}'_j = \bar{v}_j$ for any $j \neq i, i+n$. Then

$$\begin{aligned} \delta I = I(\bar{v}') - I(\bar{v}) &= \frac{\epsilon^2}{2} [I_{i,i}(\bar{v}) - 2I_{i,i+n}(\bar{v}) + I_{i+n,i+n}(\bar{v})] + o(\epsilon^2) \\ &= \frac{\epsilon^2}{2} \left(-4J_1 + \frac{1}{\bar{v}_i} + \frac{1}{\bar{v}_{i+n}} \right) + o(\epsilon^2). \end{aligned} \quad (6.5.15)$$

with

$$I_{i,i}(\bar{v}) = \left. \frac{\partial^2 I(v)}{\partial v_i^2} \right|_{v=\bar{v}}, \quad I_{i,j}(\bar{v}) = \left. \frac{\partial^2 I(v)}{\partial v_j \partial v_i} \right|_{v=\bar{v}}, \quad I_{j,j}(\bar{v}) = \left. \frac{\partial^2 I(v)}{\partial v_j^2} \right|_{v=\bar{v}}.$$

The terms associated with first derivatives vanish since \bar{v} is an extrema. Thus, if \bar{v} is a global minimum point, then

$$\frac{1}{\bar{v}_i} + \frac{1}{\bar{v}_{i+n}} \geq 4J_1. \quad (6.5.16)$$

If $\bar{v}_i = \bar{v}_{i+n} > 1/(2J_1)$ then $\delta I < 0$, which implies that \bar{v} is not a minimum. Part (ii) of this lemma then follows by noticing the definition of $s(J_1, x)$ in Def. 6.5.3.

Finally, we prove part (iii). Using the fact that $I_i(\bar{v}) = I_j(\bar{v})$ for $1 \leq i, j \leq n$, we have

$$-J_1(\bar{v}_i - \bar{v}_{i+n}) - J_2(\bar{v}_i + \bar{v}_{i+n}) + \log \bar{v}_i = -J_1(\bar{v}_j - \bar{v}_{j+n}) - J_2(\bar{v}_j + \bar{v}_{j+n}) + \log \bar{v}_j. \quad (6.5.17)$$

Multiplying Eq. (6.5.17) by 2 and setting $\bar{v}_{k+n} = s(J_1, \bar{v}_k)$ for $k = i, j$ (using part (ii)), we obtain

$$F(J, \bar{v}_i) + g(J_1, \bar{v}_i) - g(J_1, s(J_1, \bar{v}_i)) = F(J, \bar{v}_j) + g(J_1, \bar{v}_j) - g(J_1, s(J_1, \bar{v}_j))$$

By definition of $s(J_1, x)$ (Def. 6.5.3), we have $g(J_1, x) = g(J_1, s(J_1, x))$ for all x . The part (iii) then follows. \square

Lemma 6.5.13. For $J_1 > 0$ and $x > 1/(2J_1)$.

(i) $1/x + 1/s(J_1, x) > 4J_1$.

(ii) $x + s(J_1, x)$ is an increasing function of x .

(iii) $xs(J_1, x)$ is a decreasing function of x .

Proof. Recall that $s(J_1, x)$ is defined in Def. 6.5.3. We first prove part (i). In the proof of part (ii) in Lemma 6.5.12, we showed that if \bar{v} is a minimizer of $I(J_1, J_2, v)$ on $\Delta(c)$, then $1/\bar{v}_i + 1/\bar{v}_{i+n} \geq 4J_1$, see Eq. (6.5.16). We now show that in fact

$$1/x + 1/s(J_1, x) \geq 4J_1 \tag{6.5.18}$$

for all x . The $J_1 \leq 0$ case is trivial, since $s(J_1, x) = x$ and $x > 0$. The other trivial case is when $J_1 > 0$ and $x \leq 1/(2J_1)$, since again $s(J_1, x) = x$ and so $2/x \geq 1/(4J_1)$. We now study the $J_1 > 0$ and $x > 1/(2J_1)$ case. Fix $J_1 > 0$, $x > 1/(2J_1)$ and let $x + s(J_1, x) = c$. The inequality (6.5.18) follows once we show that $\bar{v} = (x, s(J_1, x))$ is a minimizer of $I(J_1, 0, v)$ on $\Delta(c)$ with $n = 1$. From the definition of $s(J_1, x)$, we know $(x, s(J_1, x))$ is an extrema (or saddle point) of $I(J_1, 0, v)$. Lemma 6.5.14 implies that if $\bar{v} \in \Delta(c)$ satisfies $\bar{v}_2 = s(J_1, \bar{v}_1) < \bar{v}_1$, then \bar{v} is a local minimum point. So the inequality (6.5.18) follows.

We then show equality holds only at $x = s(J_1, x) = 1/(2J_1)$. If $1/x + 1/s(J_1, x) = 4J_1$, then $s(J_1, x) = \frac{x}{4J_1x - 1}$. But from the definition of $s(J_1, x)$, we have

$$\log x - 2J_1x = \log s(J_1, x) - 2J_1s(J_1, x),$$

and so

$$\log(4J_1x - 1) - 2J_1x + \frac{2J_1x}{4J_1x - 1} = 0. \tag{6.5.19}$$

Elementary calculus shows the LHS of Eq. (6.5.19) is strictly decreasing for all $x > 1/(2J_1)$. So equality holds only at $x = 1/(2J_1)$. Part (i) is proved.

We then consider part (ii). The first derivative of $f(x)$ is

$$f'(x) = 1 + s'(x) = \frac{s}{1 - 2J_1 s(x)} \left(\frac{1}{x} + \frac{1}{s(x)} - 4J_1 \right)$$

Since $x > 1/(2J_1)$, one has $s(x) < 1/(2J_1)$. Thus $f'(x) > 0$ iff $1/x + 1/s(x) > 4J_1$, and so part (ii) follows from part (i).

Finally, we prove part (iii). Define $h(x) := xs(J_1, x)$ for $J_1 > 0$ and $x > 1/(2J_1)$, we have

$$h'(x) = s(J_1, x) + xs'(J_1, x) = \frac{2J_1 s(J_1, x)}{2J_1 s(J_1, x) - 1} (x + s(J_1, x) - 1/J_1).$$

For $x > 1/(2J_1)$, we have $s(J_1, x) < 1/(2J_1)$ and so $1 - 2J_1 s(J_1, x) > 0$. Part (ii) says that $x + s(J_1, x)$ is increasing for $J_1 > 0$ and all $x > 1/(2J_1)$, and thus $x + s(J_1, x) > 1/(2J_1) + s(J_1, 1/(2J_1)) = 1/J_1$. So $h'(x) < 0$ for all $x > 1/(2J_1)$. \square

Lemma 6.5.14. *Let $n = 1$, $c > 0$ and $J_2 = 0$. If $a \in (c/2, c)$ is a solution to the equation*

$$\log x - 2J_1 x = \log(c - x) - 2J_1(c - x),$$

then $(a, 1 - a)$ is a minimizer of $I(J_1, 0, v)$ on $\Delta(c)$.

Proof. Applying Lemma 6.5.12 (i) with $n = 1$ and $J_2 = 0$ shows that the minimum of $I(J_1, 0, v)$ lies in the interior of $\Delta(c)$. We can rewrite $I(J_1, 0, v)$ as

$$I(J_1, 0, v) = \tilde{I}(J_1, x) = -\frac{J_1}{2}(2x - c)^2 + x \log x + (c - x) \log(c - x),$$

where $x = v_1$ and $c - x = v_2$ with $0 \leq x \leq c$. The first derivative of $\tilde{I}(J_1, x)$ with respect to x is

$$\tilde{I}'(J_1, x) = -2J_1(2x - c) + \log x - \log(c - x).$$

Thus, we have $I'(x \rightarrow 0^+) \rightarrow -\infty$, $I'(c/2) = 0$, and $I'(x \rightarrow c^-) \rightarrow +\infty$. Moreover, for $J_1 \leq c$, one can verify that $I'(x)$ is monotonically increasing and thus $x = c/2$ is the

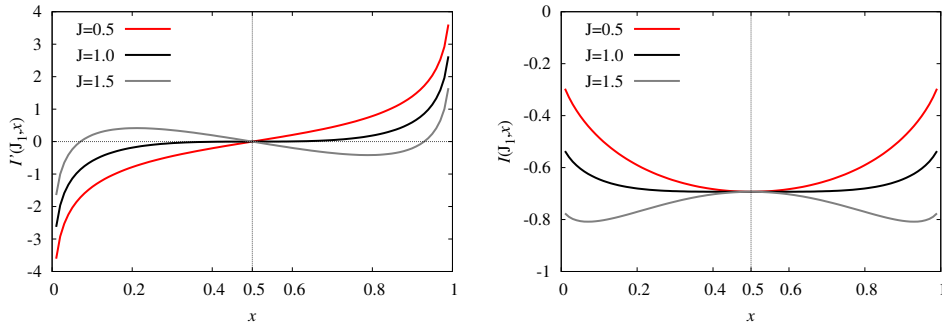


Figure 6.6: Plot of $I'(J_1, x)$ (left) and $I(J_1, x)$ (right) for $J = c/2, c$ and $3c/2$, with $c = 1$.

only minimum. For $J_1 > c$, $I(x)$ has three extremas. The point $x = c/2$ is a local maximum while other two extremas are minimums. Plots of $\tilde{I}'(J_1, x)$ and $\tilde{I}(J_1, x)$ with different values of J_1 are shown in Fig. 6.6 for interpretation. The lemma then follows. □

6.6 Discussion

We study in the first part of this paper the standard n -component face-cubic model on the complete graph. We prove limit theorems for the magnetization S_N , which implies that the phase transitions are continuous for $n = 2, 3$ and of first order for $n \geq 4$. This rigorously resolve the longstanding uncertainty about the nature of phase transition at $n = 3$. The critical points are also exactly calculated for $n \geq 2$, and for $n = 2, 3$ we simply have $\beta_c = n$, consistent with the results from the mean-field approximation. For $n \geq 4$, the values of β_c can be obtained by solving nonlinear equations. We also study central limit theorems for the magnetization at all temperatures. At criticality, the central limit theorem for S_N breaks down, and we show $N^{1/4}S_N$ converges to a distribution which is independent of N . This yields that $\mathbb{E}[(N^{1/4}S_N)^k] \sim C$ where k is any positive integer and C denotes a constant independent of N . Based on this, we obtain the asymptotic behaviors of the susceptibility χ and the specific heat C_H which are defined as $\chi \propto N\mathbb{E}[S_N^2]$ and $C_H \sim N^{-1}(\mathbb{E}[H^2] - \mathbb{E}[H]^2)$. Using the fact that $H = -NS_N^2/2$ on the complete

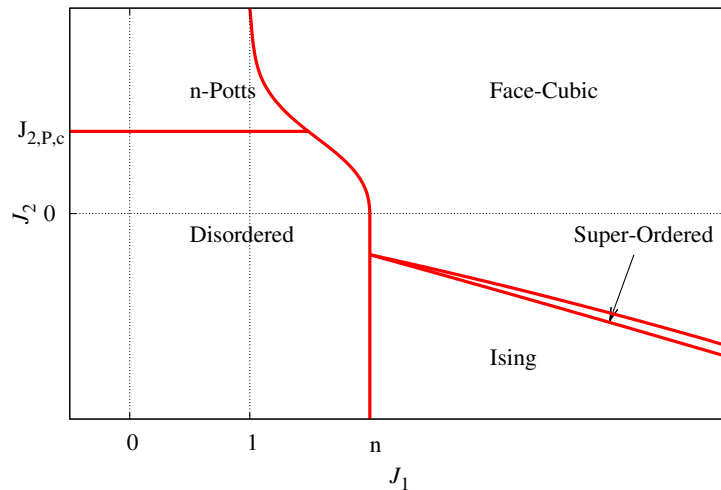


Figure 6.7: Phase diagram for the general n -component face-cubic model on the complete graph with $n = 2$. A super-ordered phase is observed in the region $-J_1 < J_2 < 0$ ($J_1 > 2$) by numerically calculating the global minimums of the rate function.

graph, we have $\chi \sim N^{1/2} \sim N^{\gamma_h}$ and $C_V \sim N^0 \sim N^{2\gamma_t-1}$. This implies the thermal exponent $\gamma_t = 1/2$ and the magnetic exponent $\gamma_h = 1/2$, for $n = 2$ and 3.

We also studied the n -component general face-cubic model on the complete graph. For $n = 2$, we prove the existence of disordered, n -state Potts, Ising and face-cubic phases on the (J_1, J_2) plane. However, there is still an unproved region where $-J_1 < J_2 < 0$ when $J_1 > 2$. Two possible scenarios can happen in this region. Proposition 6.5.8 (ii) states that this region cannot be Potts ordered or disordered. So, the first scenario is that no other ordered phase exists in this region. From the monotonic properties of the face-cubic phase (Proposition 6.5.9) and the Ising phase (Proposition 6.5.10(ii)), we know there exists a boundary such that above and below this boundary are respectively the face-cubic phase and the Ising phase. The other scenario is that another ordered phase exists in this region. As we discussed in Sec. 6.5.3, this ordered phase can only be the super-ordered phase. Again, the monotonic properties of the face-cubic and the Ising phases guarantee that the super-ordered phase is located between them. The results obtained by numerically locating the global minimum points of the rate function support the

second scenario, which is for all $J_1 > 2$, a super-ordered phase locates between the face-cubic and the Ising phases, see Fig. 6.7. Finding a rigorous proof is left as future work.

For the face-cubic model, the state of a random variable can be rephrased in terms of colors and spins. Two states ω_i and ω_j have the same color if $|\omega_i \cdot \omega_j| = 1$. In addition, two states ω_i and ω_j have the same spin if $\omega_i \cdot \omega_j = 1$, opposite spin if $\omega_i \cdot \omega_j = -1$. Various phases can be interpreted as the ordering of colors and spins. The disordered phase corresponds to both color and spin disorder. The Ising phase is spin ordered but color disordered. The Potts phase ordered in color but not in spin. The face-cubic phase is more subtle. The color is ordered, whilst spin is ordered in the dominant color but disordered in other colors. The super-ordered phase is both spin and color ordered. For the general n -component face-cubic model on the complete graph, we observed the above five phases on the phase diagrams for $n \geq 2$. We note that the super-ordered phase has not been previously discovered, even in the $n = 2$ case which corresponds to the Ashkin-Teller model. In addition, we note that the $2n$ -state Potts model is recovered when $J_2 = J_1$. On the phase diagram, one can see the $2n$ -state Potts phase can be taken as a special case of the face-cubic phase.

In order to better understand the phases of the $n = 2$ general face-cubic model on the complete graph, we can compare them with the phases of the Ashkin-Teller model. We recall that two models can be mutually mapped by defining $2\omega_i = (\sigma_i + \tau_i, \sigma_i - \tau_i)$ with $\sigma_i, \tau_i \in \{-1, 1\}$. Define $\langle \sigma \rangle = \lim_{h \rightarrow 0^+} \langle \sigma_i \rangle_h$ as the order parameter for $\{\sigma_i\}$, with h an external field. We call σ is ordered if $\langle \sigma \rangle \neq 0$ and disordered if $\langle \sigma \rangle = 0$. Analogous definitions apply for τ and $\sigma\tau$; the latter is the product of them. The comparison is summarized in Tab. 6.1. The paramagnetic phase corresponds to that σ and τ are independently disordered, that is, $\langle \sigma \rangle = 0$ and $\langle \tau \rangle = 0$. Baxter phase corresponds to σ and τ are independently ordered, that is $\langle \sigma \rangle = \pm \langle \tau \rangle \neq 0$. It is also true that $\langle \sigma\tau \rangle \neq 0$ and has the same sign as the product

$\langle \sigma \rangle \langle \tau \rangle$. The $(\sigma\tau)$ phase is such that $(\sigma\tau)$ is ordered but $\langle \sigma \rangle = \langle \tau \rangle = 0$. The partially ordered phase is such that either σ or τ (but not both) is ordered, that is, $\langle \sigma \rangle \neq 0$ ($\langle \tau \rangle \neq 0$) but $\langle \tau \rangle = \langle \sigma\tau \rangle = 0$ ($\langle \sigma \rangle = \langle \sigma\tau \rangle = 0$). It is straightforward to verify that the above four phases correspond respectively to the disordered, face-cubic, Potts and Ising phases in the $n = 2$ general face-cubic model. The super-ordered phase has not been observed in the Ashkin-Teller model, which in fact corresponds to both σ and τ ordered but $\langle \sigma \rangle \neq \langle \tau \rangle$.

A common feature is observed in the five phases of the GFC model. Let \bar{v} be a global minimum point of the rate function, and for $1 \leq i \leq n$ define $\bar{v}_i + \bar{v}_{i+n}$ as the fractional occupation of color i . The common feature is that, in all phases, at least $(n - 1)$ colors all have the same occupation. In other words, there can be at most one dominant color. When they are all equal, we have color disorder and it corresponds to either the disordered phase or the Ising phase. When there exists a dominant color, we have color order and this corresponds to the Potts, face-cubic or super-ordered phases. This seems a quite natural conjecture, and a common sense in the study of phase transitions. However, to rule out the possibility of other phases for the general face-cubic model with $n \geq 3$ is difficult. We note that, conditioned on the natural conjecture, the phase diagrams for $n \geq 3$ can also be proved rigorously.

Finally, let us mention another cubic model, the n -component corner-cubic model, the state space of which is $\Sigma = \{1, -1\}^n$. On the complete graph, the Hamiltonian of the corner-cubic model can be written as

$$H = -\frac{1}{2N} \sum_{\alpha, \beta=1}^N \langle \omega_\alpha, \omega_\beta \rangle = -\frac{1}{2N} \sum_{\alpha, \beta=1}^N \sum_{k=1}^n \omega_{\alpha k} \omega_{\beta k} = -\frac{1}{2N} \sum_{k=1}^n \sum_{\alpha, \beta=1}^N \omega_{\alpha k} \omega_{\beta k}. \quad (6.6.1)$$

Since $\omega_{\cdot k}$ is either 1 or -1 , it is exactly the superimposition of n independent Curie-Weiss models. Thus, there is a continuous phase transition at $\beta_c = 1$ for all integer $n \geq 1$.

Ashkin-Teller	$n = 2$ general face-cubic
Paramagnetic phase	Disordered phase
Baxter phase	Face-cubic phase
$(\sigma\tau)$ phase	Potts phase
Partially ordered phase	Ising phase
Not observed	Super-ordered phase

Table 6.1: Comparison of phases in the Ashkin-Teller model and the $n = 2$ general face-cubic model on the complete graph.

Chapter 7
Conclusion

Chapter 7

Conclusion

7.1 Estimating thresholds and critical exponents for the percolation and directed percolation models

The contributions of this thesis consist of three parts. First, by extensive Monte Carlo simulations, we provide precise estimates of percolation thresholds and universal parameters for some percolation and directed percolation models. These universal parameters are considered essential in understanding the nature of phase transitions, as revealed from the renormalization group theory. Precisely locating thresholds are also crucial since corrections associated with the deviations from criticality can be largely suppressed. In this thesis, our estimates are either new or improvements of previous results. To be specific, for bond and site percolation on the simple-cubic lattice in Chapter 2, our reported estimates of percolation thresholds and critical exponents are more precise than previous results. We also improve estimates of various universal amplitudes, wrapping probabilities, ratios associated with the cluster-size distribution, and the excess cluster number. We

also studied the bond and site directed percolation models on $(d + 1)$ dimensions on simple-cubic and body-centered-cubic lattices in Chapter 3, with $2 \leq d \leq 7$. Generally, our estimates of thresholds and critical exponents are much more precise than previously known results, especially in high dimensions where no previous estimates are available.

7.2 Geometric structure of percolation clusters

In addition to estimating percolation thresholds and universal parameters, our study also provide insights to understand the geometric structure of percolation clusters in Chapter 4. For critical bond percolation on the square lattice, we show that the density of bridges and nonbridges both tend to $1/4$ for large system sizes. In (Elçi *et al.*, 2015), the authors derive an exact and more general formula for the density of bridges, that is $1/(2(1 + \sqrt{q}))$, for the critical random cluster model with $0 < q \leq 4$ on the square lattice.

On the square lattice, we have found that leaf-free configurations have the same fractal dimension and hull dimension as standard percolation configurations, while bridge-free configurations have cluster and hull fractal dimensions consistent with the backbone and external perimeter dimensions, respectively. This observation is also confirmed for site percolation on the triangular lattice and bond percolation on the simple-cubic lattice. We also extend our study to the general random cluster model with $0 < q \leq 4$ in two dimensions. Results from Monte Carlo simulations show that the leaf-free configurations have the same fractal dimension and hull dimension as the corresponding standard random cluster configurations. It would also be of interest to determine whether the fractal dimensions of cluster size and hull length for bridge-free random cluster configurations again coincide with d_B and d_E when $q \neq 1$.

Motivated by the nontrivial properties of leaf-free clusters, we then consider a leaf-excluded percolation model which is defined as independent bond percolation conditioned on the absence of leaves in Chapter 5. We study this model on the square and simple-cubic lattices via Monte Carlo simulation, using a worm-like algorithm. Our results imply that the phase transition of the leaf-excluded percolation model belongs to the standard percolation universality class. It would also be of interest to study a bridge-excluded percolation model, which can be defined as independent bond percolation conditioned on the absence of bridges. Intuitively, one would expect that large clusters are broken into a collection of small clusters, and thus the critical behavior would change dramatically. To numerically confirm this scenario would be interesting.

7.3 Phase transitions of an n -component face-cubic model on the complete graph

We finally rigorously study phase transitions of an n -component face-cubic model on the complete graph in Chapter 6, by a large deviations analysis. Limit theorems are proved for the magnetization, which reveals that the phase transitions are continuous for $n \leq 3$ and of first order for $n \geq 4$. This clarifies the longstanding uncertainty about the nature of the phase transition for $n = 3$. Both thermal and magnetic exponents are $1/2$ for $n \leq 3$.

We also rigorously study the phase diagram of a general n -component face-cubic model on the complete graph. We prove the phase diagram for $n = 2$ on the (J_1, J_2) plane, except the region $-J_1 < J_2 < 0$ when $J_1 > 2$. We proved that at least four phases exist on the phase diagram: disordered, Ising, Potts, and face-cubic. In the unproved region, we numerically observe a new ordered phase. We call it the

super-ordered phase, since spins and colors are ordered simultaneously. Proving the existence of the super-ordered phase is one of our future work.

In our future work, we will first prove the existence of the super-ordered phase for $n = 2$, and then try to prove the phase diagram of the general $n \geq 3$ cases. In fact, two proved regions $J_1 \leq 1$ and $J_2 \leq -J_1$ for $n = 2$ can be directly applied to the $n \geq 3$ cases. However, other regions for $n \geq 3$ are difficult to prove. A major obstacle is the validation of a conjecture, that is, that there are at most one dominant color in any phase of the general face-cubic model. This seems a quite natural conjecture, and a common sense in the study of phase transitions. However, finding a rigorous proof is difficult.

Bibliography

Bibliography

- Adler J, Berger J, Duarte JAMS, Meir Y. 1988. Directed percolation in 3+1 dimensions. *Physical Review B* **37**: 7529–7533.
- Aizenman M, Duplantier B, Aharony A. 1999. Path-crossing exponents and the external perimeter in 2D percolation. *Physical Review Letters* **83**: 1359–1362.
- Aizenman M, Newman CM. 1984. Tree graph inequalities and critical-behavior in percolation models. *Journal of Statistical Physics* **36**: 107–143.
- Albano EV. 1994. Critical-behavior of a forest-fire model with immune trees. *Journal of Physics A: Mathematical and Theoretical* **27**: L881–L886.
- Ashkin J, Teller E. 1943. Statistics of two-dimensional lattices with four components. *Physical Review* **64**: 178–184.
- Ballesteros HG, Fernández LA, Martín-Mayor V, Muñoz Sudupe A, Parisi G, Ruiz-Lorenzo JJ. 1999. Scaling corrections: site percolation and ising model in three dimensions. *Journal of Physics A: Mathematical and Theoretical* **32**: 1.
- Baxter R. 1982. *Exactly solved models in statistical mechanics*. Academic Press.
- Baxter RJ, Kelland SB, Wu FY. 1976. Equivalence of the Potts model or Whitney polynomial with an ice-type model. *Journal of Physics A: Mathematical and Theoretical* **9**: 397–406.

- Beffara V, Duminil-Copin H. 2012. The self-dual point of the two-dimensional random-cluster model is critical for $q \geq 1$. *Probability Theory and Related Fields* **153**(3-4): 511–542.
- Blease J. 1977. Series expansions for directed-bond percolation problem. *Journal of Physics C: Solid State Physics* **10**: 917–924.
- Blöte H, Nightingale M. 1984. The temperature exponent of the n-component cubic model. *Physica A: Statistical Mechanics and its Applications* **129**(1): 1 – 16.
- Bollobás B, Riordan O. 2006. *Percolation*. Cambridge University Press.
- Bouchaud JP, Georges A. 1990. Anomalous diffusion in disordered media: statistical mechanisms, models and physical applications. *Physics Reports* **195**: 127–293.
- Broadbent SR, Hammersley JM. 1957. Percolation processes. i. crystals and mazes. *Proceedings of the Cambridge Philosophical Society* **53**: 629–641.
- Bronzan J, Dash J. 1974. Higher-order epsilon-terms in renormalization group approach to reggeon field-theory. *Physica Letter B* **51**(5): 496–498.
- Cardy J. 1992. Critical percolation in finite geometries. *Journal of Physics A: Mathematical and Theoretical* **25**: L201–L206.
- Cardy J. 2005. SLE for theoretical physicists. *Annals of Physics* **318**: 81–118.
- Cardy JL. 1987. Conformal invariance. In: *Phase Transition and Critical Phenomena*, vol. 11, Domb C, Green M, Lebowitz JL (eds), Academic Press: London.
- Chayes L, Machta J. 1998. Graphical representations and cluster algorithms {II}. *Physica A: Statistical Mechanics and its Applications* **254**(34): 477 – 516.
- Coniglio A. 1982. Cluster structure near the percolation threshold. *Journal of Physics A: Mathematical and General* **15**: 3829.

- Coniglio A. 1989. Fractal structure of Ising and Potts clusters: exact results. *Physical Review Letters* **62**: 3054–3057.
- Dembo A, Zeitouni O. 2009. *Large deviations techniques and applications*. Stochastic Modelling and Applied Probability, Springer.
- Deng Y, Blöte HWJ. 2005. Monte carlo study of the site-percolation model in two and three dimensions. *Physical Review E* **72**: 016 126.
- Deng Y, Blöte HWJ, Nienhuis B. 2004. Backbone exponents of the two-dimensional q -state Potts model: A Monte Carlo investigation. *Physical Review E* **69**: 026 114.
- Deng Y, Garoni TM, Sokal AD. 2007. Dynamic Critical Behavior of the Worm Algorithm for the Ising Model. *Physical Review Letters* **99**: 110 601.
- Deng Y, Zhang W, Garoni TM, Sokal AD, Sportiello A. 2010. Some geometric critical exponents for percolation and the random-cluster model. *Physical Review E* **81**: 020 102R.
- Dickman R. 1999. Reweighting in nonequilibrium simulations. *Physical Review E* **60**: R2441–R2444.
- Ditzian RV, Banavar JR, Grest GS, Kadanoff LP. 1980. Phase diagram for the ashkin-teller model in three dimensions. *Physical Review B* **22**: 2542–2553.
- Duplantier B. 1999. Harmonic measure exponents for two-dimensional percolation. *Physical Review Letters* **82**: 3940–3943.
- Duplantier B. 2000. Conformally invariant fractals and potential theory. *Physical Review Letters* **84**: 1363–1367.
- Eisele T, Ellis R. 1983. Symmetry breaking and random waves for magnetic systems on a circle. *Zeitschrift für Wahrscheinlichkeitstheorie und Verwandte Gebiete* **63**: 297–348.

- Elçi EM, Weigel M, Fytas NG. 2015. Fragmentation of fractal random structures. *Physical Review Letters* **114**: 115 701.
- Ellis R. 2005. *Entropy, large deviations, and statistical mechanics*. Springer.
- Ellis R, Haven K, Turkington B. 2000. Large deviation principles and complete equivalence and nonequivalence results for pure and mixed ensembles. *Journal of Statistical Physics* **101**: 999–1064.
- Ellis R, Newman C. 1978a. Limit theorems for sums of dependent random variables occurring in statistical mechanics. *Zeitschrift für Wahrscheinlichkeitstheorie und Verwandte Gebiete* **44**: 117–139.
- Ellis R, Newman C. 1978b. The statistics of curie-weiss models. *Journal of Statistical Physics* **19**: 149–161.
- Ellis R, Newman C, Rosen J. 1980. Limit theorems for sums of dependent random variables occurring in statistical mechanics. *Zeitschrift für Wahrscheinlichkeitstheorie und Verwandte Gebiete* **51**: 153–169.
- Ellis RS, Wang K. 1990. Limit theorems for the empirical vector of the curie-weiss-potts model. *Stochastic Processes and their Applications* **35**: 59 – 79.
- Ellis-Monaghan JA, Moffatt I. 2013. *Graphs on Surfaces: Dualities, Polynomials, and Knots*. Springer: New York.
- Essam JW. 1972. Percolation and cluster size. In: *Phase Transition and Critical Phenomena*, vol. 2, Domb C, Green M (eds), Academic Press: New York.
- Fan C, Wu FY. 1970. General lattice model of phase transitions. *Physical Review B* **2**: 723–733.
- Feng X, Deng Y, Blöte HWJ. 2008. *Physical Review E* **78**: 031 136.
- Fortuin C, Kasteleyn P. 1972. On the random-cluster model. *Physica* **57(4)**: 536 – 564.

- Foster JG, Grassberger P, Paczuski M. 2009. Reinforced walks in two and three dimensions. *New Journal of Physics* **11**: 023 009.
- Grassberger P. 1982. On phase-transitions in schlogl 2nd model. *Zeitschrift für Physik B Condensed Matter* **47**: 365–374.
- Grassberger P. 1992. Spreading and backbone dimensions of 2D percolation. *Journal of Physics A: Mathematical and General* **25**: 5475–5484.
- Grassberger P. 2003. Critical percolation in high dimensions. *Physical Review E* **67**: 036 101.
- Grassberger P. 2009a. *Physical Review E* **79**: 052 104.
- Grassberger P. 2009b. Local persistence in directed percolation. *Journal of Statistical Mechanics: Theory and Experiment* (08): P08 021.
- Grassberger P, Zhang Y. 1996. “self-organized” formulation of standard percolation phenomena. *physica A* **224**: 169–179.
- Grimmett GR. 1999. *Percolation*. Springer: Berlin, 2 edn.
- Grossman T, Aharony A. 1987. Accessible external perimeters of percolation clusters. *Journal of Physics A: Mathematical and General* **20**: L1193–L1201.
- Guo W, Qian X, Blöte HWJ, Wu FY. 2006. Critical line of an n -component cubic model. *Physical Review E* **73**: 026 104.
- Hara T, Slade G. 1990. Mean-field critical-behavior for percolation in high dimensions. *Communications in Mathematical Physics* **128**: 333–391.
- Havlin S, ben Avraham D. 1987. Diffusion in disordered media. *Advances in Physics* **36**: 695–798.
- Herrmann HJ, Hong DC, Stanley HE. 1984. Backbone and elastic backbone of percolation clusters obtained by the new method of ‘burning’. *Journal of Physics A: Mathematical and Theoretical* **17**: L261.

- Herrmann HJ, Stanley HE. 1984. Building blocks of percolation clusters: Volatile fractals. *Physical Review Letters* **53**: 1121–1124.
- Hinrichsen H. 2000. Non-equilibrium critical phenomena and phase transitions into absorbing states. *Advances in Physics* **49**(7): 815–958.
- Hu H, Blöte HWJ, Deng Y. 2012. Percolation in the canonical ensemble. *Journal of Physics A: Mathematical and Theoretical* **45**(49): 494 006.
- Jacobsen JL, Zinn-Justin P. 2002. A transfer matrix for the backbone exponent of two-dimensional percolation. *Journal of Physics A: Mathematical and General* **35**: 2131–2144.
- Janssen HK. 1981. On the non-equilibrium phase-transition in reaction-diffusion systems with an absorbing stationary state. *Zeitschrift für Physik B Condensed Matter* **42**: 151–154.
- Janssen HK, Stenull O. 2004. Logarithmic corrections in directed percolation. *Physical Review E* **69**: 016 125.
- Janssen HK, Täuber U. 2005. The field theory approach to percolation processes. *Annals of Physics* **315**(1): 147–192.
- Jensen I. 1992. Critical behavior of the three-dimensional contact process **45**: R563–R566.
- Jensen I. 1996. Low-density series expansions for directed percolation on square and triangular lattices. *Journal of Physics A: Mathematical and Theoretical* **29**: 7013–7040.
- Jensen I. 1999. Low-density series expansions for directed percolation: I. a new efficient algorithm with applications to the square lattice. *Journal of Physics A: Mathematical and Theoretical* **32**(28): 5233–5249.

- Jensen I. 2004. Low-density series expansions for directed percolation: Iii. some two-dimensional lattices. *Journal of Physics A: Mathematical and Theoretical* **37**(27): 6899–6915.
- Jensen I, Guttmann A. 1995. Series expansions of the percolation probability for directed square and honeycomb lattices. *Journal of Physics A: Mathematical and Theoretical* **28**(17): 4813–4833.
- Kager W, Nienhuis B. 2004. A guide to stochastic Löwner evolution and its applications. *Journal of Statistical Physics* **115**: 1149–1229.
- Kesten H. 1980. The critical probability of bond percolation on the square lattice equals $1/2$. *Communications in Mathematical Physics* **74**: 41–59.
- Kim D, Levy PM. 1975. Critical behavior of the cubic model. *Physical Review B* **12**: 5105–5111.
- Kim D, Levy PM, Sudano JJ. 1976. Applicability of the cubic model to the critical behavior of real systems. *Physical Review B* **13**: 2054–2065.
- Kim D, Levy PM, Uffer LF. 1975. Cubic rare-earth compounds: Variants of the three-state potts model. *Physical Review B* **12**: 989–1004.
- Kozlov B, Laguës M. 2010. Universality of 3d percolation exponents and first-order corrections to scaling for conductivity exponents. *Physica A* **389**: 5339–5346.
- Kurrer C, Schulten K. 1993. Dependence of percolation thresholds on lattice connectivity. *Physical Review E* **48**: 614–617.
- Langlands R, Pouliot P, Saint-Aubin Y. 1994. Conformal-invariance in 2-dimensional percolation. *Bulletin of American Mathematical Society* **30**: 1–61.
- Langlands RP, Pichet C, Pouliot P, Saint-Aubin Y. 1992. On the universality of crossing probabilities in 2-dimensional percolation. *Journal of Statistical Physics* **67**: 553–574.

- Lawler GF, Schramm O, Werner W. 2002. One-arm exponent for critical 2D percolation. *Electronic Journal of Probability* **7**: 2.
- Lorenz CD, Ziff RM. 1998a. Precise determination of the bond percolation thresholds and finite-size scaling corrections for the sc, fcc, and bcc lattices. *Physical Review E* **57**: 230–236.
- Lorenz CD, Ziff RM. 1998b. Universality of the excess number of clusters and the crossing probability function in three-dimensional percolation. *Journal of Physics A: Mathematical and Theoretical* **31**: 8147.
- Lubeck S, Willmann R. 2002. Universal scaling behaviour of directed percolation and the pair contact process in an external field. *Journal of Physics A: Mathematical and Theoretical* **35**(48): 10 205–10 217.
- Lubeck S, Willmann R. 2004. Universal scaling behavior of directed percolation around the upper critical dimension. *Journal of Statistical Physics* **115**: 1231–1250.
- Martins PHL, Plascak JA. 2003. Percolation on two- and three-dimensional lattices. *Physical Review E* **67**: 046 119.
- Mollison D. 1977. Spatial contact models for ecological and epidemic spread. *Journal of the Royal Statistical Society. Series B (Methodological)* **39**(3): 283–326.
- Newman MEJ, Ziff RM. 2000. Efficient monte carlo algorithm and high-precision results for percolation. *Physical Review Letters* **85**: 4104–4107.
- Nienhuis B. 1984. Critical behavior of two-dimensional spin models and charge asymmetry in the Coulomb gas. *Journal of Statistical Physics* **34**: 731–761.
- Nienhuis B. 1987. Coulomb gas formulation of two-dimensional phase transitions. In: *Phase Transition and Critical Phenomena*, vol. 11, Domb C, M G, Lebowitz JL (eds), Academic Press: London.

- Nienhuis B, Riedel EK, Schick M. 1983. Critical behavior of the n -component cubic model and the ashkin-teller fixed line. *Physical Review B* **27**: 5625–5643.
- Onsager L. 1944. Crystal statistics. i. a two-dimensional model with an order-disorder transition. *Physical Review* **65**: 117–149.
- Perlsman E, Havlin S. 2002. Method to estimate critical exponents using numerical studies. *Europhysics Letters* **58**(2): 176–181.
- Pinson HT. 1994. Critical percolation on the torus. *Journal of Statistical Physics* **75**: 1167–1177.
- Prokof'ev N, Svistunov B. 2001. Worm algorithms for classical statistical models. *Physical Review Letters* **87**: 160 601.
- Saleur H, Duplantier B. 1987. Exact determination of the percolation hull exponent in two dimensions. *Physical Review Letters* **58**: 2325–2328.
- Schmidt JM. 2013. A simple test on 2-vertex- and 2-edge-connectivity. *Information Processing Letters* **113**: 241–244.
- Sedgewick R. 1998. *Algorithms in c*. Addison-Wesley: Reading, Massachusetts, 3 edn.
- Smirnov S, Werner W. 2001. Critical exponents for two-dimensional percolation. *Mathematical Research Letters* **8**: 729–744.
- Stanley HE. 1977. Cluster shapes at the percolation threshold: an effective cluster dimensionality and its connection with critical-point exponents. *Journal of Physics A: Mathematical and Theoretical* **10**: L211–L220.
- Stauffer D, Aharony A. 1994. *Introduction to percolation theory*. Taylor & Francis: London, 2 edn.
- Stauffer D, Aharony A. 2003. *Introduction to Percolation Theory*. Taylor & Francis: London, 2 edn.

- Sweeny M. 1983. Monte carlo study of weighted percolation clusters relevant to the potts models. *Physical Review B* **27**: 4445–4455.
- Tarjan RE. 1974. A note on finding the bridges of a graph. *Information Processing Letters* **2**: 160–161.
- Toulouse G. 1974. Perspectives from theory of phase-transitions. *Nuovo Cimento Soc. Ital. Fis.* **B 23**: 234–240.
- Vasseur R, Jacobsen JL, Saleur H. 2012. Logarithmic observables in critical percolation. *Journal of Statistical Mechanics: Theory and Experiment* **2012**: L07 001.
- Voigt CA, Ziff RM. 1997. Epidemic analysis of the second-order transition in the ziff-gulari-barshad surface-reaction model. *Physical Review E* **56**: R6241–R6244.
- Wang J, Zhou Z, Liu Q, Garoni TM, Deng Y. 2013a. High-precision monte carlo study of directed percolation in $(d+1)$ dimensions. *Physical Review E* **88**: 042 102.
- Wang J, Zhou Z, Zhang W, Garoni TM, Deng Y. 2013b. Bond and site percolation in three dimensions. *Physical Review E* **87**: 052 107.
- Wang J, Zhou Z, Zhang W, Garoni TM, Deng Y. 2014. Erratum: Bond and site percolation in three dimensions [phys. rev. e 87, 052107 (2013)]. *Physical Review E* **89**: 069 907.
- Wolff U. 2009a. Simulating the all-order hopping expansion II: Wilson fermions. *Nuclear Physics B* **814**: 549–572.
- Wolff U. 2009b. Simulating the all-order strong coupling expansion I: Ising model demo. *Nuclear Physics B* **810**: 491–502.
- Wolff U. 2010a. Simulating the all-order strong coupling expansion III: $O(N)$ sigma/loop models. *Nuclear Physics B* **824**: 254–272.
- Wolff U. 2010b. Simulating the all-order strong coupling expansion IV: $CP(N-1)$ as a loop model. *Nuclear Physics B* **832**: 520–537.

- Xu X, Wang J, Lv JP, Deng Y. 2014a. Simultaneous analysis of three-dimensional percolation models. *Frontiers of Physics* **9**: 113–119.
- Xu X, Wang J, Zhou Z, Garoni TM, Deng Y. 2014b. Geometric structure of percolation clusters. *Physical Review E* **89**: 012 120.
- Zhou Z, Garoni TM. 2015. An n -component face-cubic model on the complete graph. *in preparation* .
- Zhou Z, Xu X, Garoni TM, Deng Y. 2015. Leaf-excluded percolation in two and three dimensions. *Physical Review E* **91**: 022 140.
- Zhou Z, Yang J, Ziff RM, Deng Y. 2012a. Crossover from isotropic to directed percolation. *Physical Review E* **86**: 021 102.
- Zhou Z, Yang J, Ziff RM, Deng Y. 2012b. shortest-path fractal dimension in two and three dimensions. *Physical Review E* **86**: 061 101.
- Ziff RM. 2011. Correction-to-scaling exponent for two-dimensional percolation. *Physical Review E* **83**: 020 107.
- Ziff RM, Finch SR, Adamchik VS. 1997. Universality of finite-size corrections to the number of critical percolation clusters. *Physical Review Letters* **79**: 3447–3450.
- Ziff RM, Lorenz CD, Kleban P. 1999. Shape-dependent universality in percolation. *Physica A: Statistical Mechanics and its Applications* **266**: 17 – 26.